

Spring 2008

# Fabrication of bioactive osteogenic controlled-release systems, cellular platforms, and cellular capsules using layer -by -layer nanoassembly

Skylar Stewart-Clark  
*Louisiana Tech University*

Follow this and additional works at: <https://digitalcommons.latech.edu/dissertations>



Part of the [Biomedical Engineering and Bioengineering Commons](#)

---

## Recommended Citation

Stewart-Clark, Skylar, "" (2008). *Dissertation*. 514.  
<https://digitalcommons.latech.edu/dissertations/514>

This Dissertation is brought to you for free and open access by the Graduate School at Louisiana Tech Digital Commons. It has been accepted for inclusion in Doctoral Dissertations by an authorized administrator of Louisiana Tech Digital Commons. For more information, please contact [digitalcommons@latech.edu](mailto:digitalcommons@latech.edu).

**FABRICATION OF BIOACTIVE OSTEOGENIC CONTROLLED-  
RELEASE SYSTEMS, CELLULAR PLATFORMS, AND  
CELLULAR CAPSULES USING LAYER-BY-LAYER  
NANOASSEMBLY**

by

Skylar Stewart-Clark, B.S.

A Dissertation Presented in Partial Fulfillment  
of the Requirements of the Degree  
Doctor of Philosophy

COLLEGE OF ENGINEERING AND SCIENCE  
LOUISIANA TECH UNIVERSITY

May 2008

UMI Number: 3308060

### INFORMATION TO USERS

The quality of this reproduction is dependent upon the quality of the copy submitted. Broken or indistinct print, colored or poor quality illustrations and photographs, print bleed-through, substandard margins, and improper alignment can adversely affect reproduction.

In the unlikely event that the author did not send a complete manuscript and there are missing pages, these will be noted. Also, if unauthorized copyright material had to be removed, a note will indicate the deletion.

**UMI**<sup>®</sup>

---

UMI Microform 3308060

Copyright 2008 by ProQuest LLC.

All rights reserved. This microform edition is protected against unauthorized copying under Title 17, United States Code.

ProQuest LLC  
789 E. Eisenhower Parkway  
PO Box 1346  
Ann Arbor, MI 48106-1346

LOUISIANA TECH UNIVERSITY

THE GRADUATE SCHOOL

April 18, 2008

Date

We hereby recommend that the dissertation prepared under our supervision by Skylar Stewart-Clark entitled Fabrication of Bioactive Osteogenic Cellular Capsules, Cellular Platforms, and Controlled-Release Systems Using Layer-by-Layer Nanoassembly

be accepted in partial fulfillment of the requirements for the Degree of Doctor of Philosophy in Biomedical Engineering

David Mills  
Supervisor of Dissertation Research  
Sten Gjo  
Head of Department  
Biomedical Engineering  
Department

Recommendation concurred in:

Sten Gjo  
Paul Cook  
Yuri Lvov  
Pat O'Neil

Advisory Committee

Approved:  
Pat Srinivasan  
Director of Graduate Studies

Approved:  
William McConathy  
Dean of the Graduate School

Sten Gjo  
Dean of the College

## ABSTRACT

There is an ever-increasing awareness that the field of tissue engineering offers many potential solutions to clinical problems. While advances along these lines have been made, the design and implementation of an “off the shelf” tissue is yet to be realized. Thus, the objectives of this work were largely aimed at the design and fabrication of biocompatible, bioactive structures which could be integrated into existing biomaterial products.

The electrostatic layer-by-layer (LbL) self-assembly technique was used to incorporate biologically relevant molecules within controlled release systems, cell culture platforms, and 3-D cellular capsules. Two delivery systems were investigated to determine the release of a model drug, dexamethasone (DEX). In the first system, nanothin polyelectrolyte (PE) layers were applied to the micronized drug crystals as a diffusion barrier. In the second system, DEX was physically entrapped within calcium alginate microspheres which were further modified with PE layers. The fabrication of cell culture platforms functionalized with nanothin layers of PEs, TiO<sub>2</sub> nanoparticles, and the growth factor TGFβ<sub>1</sub> was achieved through ultrasonic nebulization. Finally, individual cellular capsules were fabricated by elaborating the LbL process on mesenchymal stem cell and human dermal fibroblast templates.

Materials characterization and cell culture testing were performed as preliminary indicators of potential cytotoxicity. Release of the drug DEX was enhanced when

directly templated with polyelectrolyte layers while DEX entrapment within polyelectrolyte-modified alginate microspheres reduced drug release by a factor of three. An encouraging result of *in vitro* cell culture assessment was the distinct change in fibrochondrocyte morphology when compared with positive and negative controls. An ultrasonic nebulizer produced 14-layered cell culture substrates containing DEX, TiO<sub>2</sub> nanoparticles, and the growth factor TGFβ<sub>1</sub>. In comparison with traditionally dipped substrates, layer fabrication was expedited six-fold. Moreover, the positioning of TGFβ<sub>1</sub> within the layer architecture modulated cell behavior. For example, incorporation of the growth factor as a terminal layer produced visible cellular extensions associated with enhanced adhesion of human dermal fibroblasts (HDFs) to the substrates. The final application of LbL was for production of nanothin cellular capsules. Layer fabrication onto both HDFs and mouse mesenchymal stem cells (MSCs) was demonstrated with acceptable cell tolerances although cell viability is likely affected by layer composition and encapsulation time.

The major findings of this work not only demonstrated the feasibility of the technologies, but also their ability to influence cellular behavior by exposure to specific layer chemistries and architectures. The results are extremely promising for both further fundamental research, as well as translation into products. A major obstacle is determining optimal parameters necessary to yield a given cell response. Moreover, cost effectiveness must be addressed before clinical implementation of these systems is realized. Undoubtedly, the work here provides an underpinning for the development of additional capsules, microspheres, and substrates which could ultimately be integrated to create novel, biocompatible, heterogeneous assemblies.

## APPROVAL FOR SCHOLARLY DISSEMINATION

The author grants to the Prescott Memorial Library of Louisiana Tech University the right to reproduce, by appropriate methods, upon request, any or all portions of this Dissertation. It is understood that "proper request" consists of the agreement, on the part of the requesting party, that said reproduction is for his personal use and that subsequent reproduction will not occur without written approval of the author of this Dissertation. Further, any portions of the Dissertation used in books, papers, and other works must be appropriately referenced to this Dissertation.

Finally, the author of this Dissertation reserves the right to publish freely, in the literature, at any time, any or all portions of this Dissertation.

Author

Shyke Stat-Oll

Date

5/2/2008

## **DEDICATION**

To my son Adrian for giving me a renewed sense of inspiration, and my husband Geoff  
for his never-ending love, support, and understanding.

## TABLE OF CONTENTS

<b>ABSTRACT</b> .....	<b>iii</b>
<b>LIST OF TABLES</b> .....	<b>xi</b>
<b>LIST OF FIGURES</b> .....	<b>xii</b>
<b>ACKNOWLEDGMENTS</b> .....	<b>xviii</b>
<b>CHAPTERS</b>	
<b>1 INTRODUCTION AND BACKGROUND</b> .....	<b>1</b>
1.1 The Cellular Niche .....	3
1.2 Orthopedic and Dental Tissue Engineering .....	5
1.2.1 Design Requirements .....	6
1.2.1.1 Osteoinductive component .....	6
1.2.1.2 Osteogenic component .....	7
1.2.1.3 Osteoconductive component .....	9
1.2.1.4 Other factors .....	10
1.2.2 Dental and Orthopedic Biomaterials .....	11
1.2.3 Influential Factors for Cell-Substrate Interactions .....	12
1.2.3.1 Surface roughness .....	13
1.2.3.2 Surface chemistry and surface energy .....	14
1.2.3.3 Surface stiffness .....	15
1.3 Specific Aims and Novel Aspects .....	16
1.4 Dissertation Overview .....	19
<b>2 SELF-ASSEMBLY IN TISSUE ENGINEERING</b> .....	<b>20</b>
2.1 Self-Assembly of Thin Films .....	20
2.2 Nanofabrication by LbL Assembly .....	22
2.2.1 Fabrication of LbL Films by Substrate Dipping .....	22
2.2.2 Fabrication of LbL Films by Spraying .....	24
2.3 Multilayered LbL Films for Biological Applications .....	24
2.3.1 Cell Culture on Polyelectrolyte LbL Films .....	25
2.3.2 Cell Culture on Nanophase LbL Films .....	27
2.3.3 Incorporation of Bioactive Species in LbL Films .....	28
<b>3 METHODS AND INSTRUMENTATION USED FOR EXPERIMENTAL QUANTITATION AND ANALYSIS</b> .....	<b>30</b>
3.1 Materials Characterization Methods .....	30

3.1.1	Quartz Crystal Microbalance Technique .....	31
3.1.2	Zeta-Potential Analysis .....	31
3.1.3	Ultraviolet-Visible Spectroscopy .....	32
3.1.4	Laser Scanning Confocal Microscopy .....	32
3.1.5	Atomic Force Microscopy .....	33
3.1.6	Ultrasonic Nebulization .....	33
3.2	Cellular Characterization Methods .....	34
3.2.1	Live/Dead Assay .....	34
3.2.2	Cellular Metabolic Activity Assays .....	34
3.2.3	PicoGreen Assay .....	35
3.2.4	Immunocytochemistry .....	35
<b>4</b>	<b>CONTROLLED RELEASE OF DEXAMETHASONE USING LAYER-BY-LAYER ASSEMBLY .....</b>	<b>37</b>
4.1	Introduction .....	37
4.2	Materials and Methods .....	40
4.2.1	Preparation of Polyelectrolyte and Drug Solutions .....	40
4.2.2	Fabrication of Calcium Alginate Microspheres .....	41
4.2.3	Surface Modification of Release Systems Using LbL Assembly .....	42
4.3	Results and Discussion .....	43
4.3.1	Influence of Layer Architecture on Aggregate Assembly .....	43
4.3.2	Comparison of PSS/PS-Modified Release Systems .....	45
4.3.2.1	Zeta-potential measurements .....	45
4.3.2.2	QCM measurements .....	47
4.3.2.3	Dexamethasone release testing .....	49
4.3.2.4	Confocal microscopy .....	53
4.3.2.5	<i>In vitro</i> analysis of fibrochondrocyte response .....	54
4.3.2.5.1	Cell viability and morphology .....	55
4.3.2.5.2	Cellular metabolic activity .....	58
4.3.2.5.3	Aggrecan and collagen II immunocytochemistry .....	60
4.3.3	Comparison of CS/GelB-Modified Release Systems .....	68
4.3.3.1	QCM measurements .....	69
4.3.3.2	Dexamethasone release testing .....	70
4.4	Conclusions .....	72
<b>5</b>	<b>FABRICATION AND CHARACTERIZATION OF CELL- SUPPORTIVE SUBSTRATES USING NEBULIZED LAYER-BY- LAYER ASSEMBLY .....</b>	<b>74</b>
5.1	Introduction .....	74
5.2	Materials and Methods .....	77
5.2.1	Preparation of Polyelectrolyte, Nanoparticle, Protein, and Drug Solutions .....	77
5.2.2	Fabrication of Multilayered Substrates .....	78
5.3	Results and Discussion .....	80

5.3.1	LbL Nebulized Thin Films Functionalized with TiO <sub>2</sub> and Dexamethasone .....	80
5.3.1.1	Zeta-potential measurements .....	81
5.3.1.2	QCM measurements.....	83
5.3.1.3	AFM measurements .....	87
5.3.2	LbL Nebulized Thin Films Functionalized with TGFβ <sub>1</sub> .....	92
5.3.2.1	Zeta-potential measurements .....	92
5.3.2.2	QCM measurements.....	94
5.3.2.3	Cell culture.....	98
5.3.2.3.1	Cell viability.....	99
5.3.2.3.2	Mitochondrial activity.....	100
5.3.2.3.3	DNA quantification.....	102
5.3.2.3.4	Cell morphology and localization of BrdU and collagen I .....	104
5.4	Conclusions.....	108
<b>6</b>	<b>CELLULAR ENCAPSULATION WITHIN NANOTHIN CAPSULES USING LAYER-BY-LAYER ASSEMBLY.....</b>	<b>111</b>
6.1	Introduction.....	111
6.2	Materials and Methods.....	114
6.2.1	Preparation of Polyelectrolyte, Nanoparticle, Protein, and Drug Solutions.....	114
6.2.2	Fabrication of Cellular Capsules.....	115
6.3	Results and Discussion .....	116
6.3.1	MSC Encapsulation in Biocompatible Shells .....	116
6.3.1.1	Zeta-potential measurements .....	116
6.3.1.2	QCM measurements.....	119
6.3.1.3	Fluorescence microscopy .....	120
6.3.1.4	Mitochondrial activity.....	124
6.3.2	HDF Encapsulation in TGFβ <sub>1</sub> Functionalized Shells.....	127
6.3.2.1	Zeta-potential measurements .....	127
6.3.2.2	QCM measurements.....	128
6.3.2.3	Viability of encapsulated HDFs .....	129
6.4	Conclusions.....	131
<b>7</b>	<b>CONCLUSIONS AND FUTURE WORK.....</b>	<b>134</b>
7.1	Conclusions.....	134
7.2	Future Work .....	135
7.2.1	Controlled-Release Technology.....	135
7.2.2	Nebulized Substrates with Bioactive Functionality.....	136
7.2.3	Cellular Encapsulation.....	137
<b>APPENDICIES</b>		
<b>APPENDIX A</b>	<b>PROTOCOL FOR FABRICATION OF CALCIUM ALGINATE MICROSPHERES .....</b>	<b>139</b>

<b>APPENDIX B</b>	<b>FITC-CONJUGATION PROTOCOL.....</b>	<b>141</b>
<b>APPENDIX C</b>	<b>WST-1 ASSAY .....</b>	<b>143</b>
<b>APPENDIX D</b>	<b>IMMUNOCYTOCHEMICAL LOCALIZATION OF CELLULAR ANTIGENS.....</b>	<b>145</b>
<b>APPENDIX E</b>	<b>MTT ASSAY .....</b>	<b>149</b>
<b>APPENDIX F</b>	<b>CELL LYSIS PROTOCOL .....</b>	<b>151</b>
<b>REFERENCES.....</b>		<b>153</b>
<b>VITA.....</b>		<b>168</b>

## LIST OF TABLES

<b>Table 4.1</b>	Polyelectrolytes, Biomolecules and Their Isoelectric Points.....	43
<b>Table 4.2</b>	Layering Schemes and Surface Charge Measurements for Potential Surface Modifications of Dexamethasone .....	44
<b>Table 4.3</b>	Average Monolayer Thickness for PSS and PS Layers Deposited on Dexamethasone Aggregates at pH 4 and pH 7 .....	48
<b>Table 4.4</b>	Zero-Order Release Kinetics for Dexamethasone Delivery Systems .....	51
<b>Table 5.1</b>	Isoelectric Points of Polyelectrolytes, Nanoparticles, and Biomolecules.....	77
<b>Table 5.2</b>	Qualitative Outcome of Varying Individual Nebulization Parameters for LbL Films Composed of Synthetic and Natural PEs.....	79
<b>Table 5.3</b>	Layering Architectures for Nebulized Films Functionalized with TiO <sub>2</sub> and Dexamethasone .....	81
<b>Table 5.4</b>	Average Layer Thicknesses Produced by Dipping and Nebulization .....	86
<b>Table 5.5</b>	Surface Parameters for Nebulized TiO <sub>2</sub> Films Obtained from AFM Measurements .....	91
<b>Table 5.6</b>	Nebulized Layer Architectures Functionalized with TGFβ <sub>1</sub> .....	92
<b>Table 5.7</b>	Minimum Exposure Times for Collagen I Fluorescence Signal Acquisition.....	108
<b>Table 6.1</b>	Isoelectric Points of Polyelectrolytes, Nanoparticles, and Biomolecules.....	115
<b>Table 6.2</b>	PLL/TGFβ <sub>1</sub> Layer Architectures.....	127
<b>Table 6.3</b>	Surface Charge Inversions for Encapsulated HDFs Comparing Different Layering Schemes .....	130

## LIST OF FIGURES

<b>Figure 4.1</b>	Schematic of dexamethasone-loaded calcium alginate microspheres. ....	41
<b>Figure 4.2</b>	Schematic of LbL surface modification of micronized dexamethasone for production of dexamethasone aggregates.....	42
<b>Figure 4.3</b>	Net surface charge characteristics following deposition of PSS and PS monolayers onto dexamethasone aggregates assembled at pH 4 and resuspended at pH 7 .....	46
<b>Figure 4.4</b>	Net surface charge characteristics following deposition of PS and PSS monolayers onto dexamethasone-loaded calcium alginate microspheres at pH 7 .....	47
<b>Figure 4.5</b>	Progressive film thickness after deposition of PSS and PS monolayers as obtained from QCM measurements.....	48
<b>Figure 4.6</b>	Release profile for PSS/PS modified DEX aggregates, DEX in alginate microspheres, and unencapsulated DEX, 3 mg preparations used, release testing in PBS .....	50
<b>Figure 4.7</b>	Steady-state release kinetics for dexamethasone aggregates and dexamethasone-loaded microspheres.....	51
<b>Figure 4.8</b>	Confocal micrograph and line profile of PSS/PS modified dexamethasone aggregates.....	53
<b>Figure 4.9</b>	Percent cell viability for treated and control cultures, n=3, symbols denote statistically significant difference, p<.05, one-tailed t-test .....	56
<b>Figure 4.10</b>	Cell morphology of treated and control cultures at t=0, 12, and 36 hours, A-C, controls, D-F, cells cultured in media supplemented with unencapsulated dexamethasone, G-I, cells cultured in media supplemented with dexamethasone aggregates. Original magnification 100X, scale bar=15 $\mu\text{m}$ .....	57

<b>Figure 4.11</b>	WST-1 Assay for determination of cellular metabolic activity for fibrochondrocytes cultured in complete media, media supplemented with unencapsulated dexamethasone, and media supplemented with dexamethasone aggregates. Measurement data obtained at 440nm, reference 690 nm using a Tecan Spectrophotometer. Seeding density 10,000 cells/well, n=3 .....	59
<b>Figure 4.12</b>	Negative controls for (a) aggrecan and (b) collagen II. Primary antibodies were replaced with blocking serum. Original magnification 400X .....	61
<b>Figure 4.13</b>	Immunocytochemical results for aggrecan localization at t=0 hours (a) control FCs cultured without dexamethasone supplement, (b) FCs cultured with unencapsulated dexamethasone, (c) FCs cultured with dexamethasone aggregates. Original magnification 100X .....	62
<b>Figure 4.14</b>	Immunocytochemical results for aggrecan localization at t=12 hours (a) control FCs cultured without dexamethasone supplement, (b) FCs cultured with unencapsulated dexamethasone, (c) FCs cultured with dexamethasone aggregates. Original magnification 100X .....	62
<b>Figure 4.15</b>	Immunocytochemical results for aggrecan localization at t=24 hours (a) control FCs cultured without dexamethasone supplement, (b) FCs cultured with unencapsulated dexamethasone, (c) FCs cultured with dexamethasone aggregates. Original magnification 100X .....	63
<b>Figure 4.16</b>	Immunocytochemical results for aggrecan localization at t=36 hours (a) control FCs cultured without dexamethasone supplement, (b) FCs cultured with unencapsulated dexamethasone, (c) FCs cultured with dexamethasone aggregates. Original magnification 100X .....	64
<b>Figure 4.17</b>	Immunocytochemical results for aggrecan localization at t=48 hours (a) control FCs cultured without dexamethasone supplement, (b) FCs cultured with unencapsulated dexamethasone, (c) FCs cultured with dexamethasone aggregates. Original magnification 100X .....	64
<b>Figure 4.18</b>	Immunocytochemical results for collagen II localization at t=0 hours (a) control FCs cultured without dexamethasone supplement, (b) FCs cultured with unencapsulated dexamethasone, (c) FCs cultured with dexamethasone aggregates. Original magnification 100X .....	65

<b>Figure 4.19</b>	Immunocytochemical results for collagen II localization at t=12 hours (a) control FCs cultured without dexamethasone supplement, (b) FCs cultured with unencapsulated dexamethasone, (c) FCs cultured with dexamethasone aggregates. Original magnification 100X .....	65
<b>Figure 4.20</b>	Immunocytochemical results for collagen II localization at t=36 hours (a) control FCs cultured without dexamethasone supplement, (b) FCs cultured with unencapsulated dexamethasone, (c) FCs cultured with dexamethasone aggregates. Original magnification 200X .....	66
<b>Figure 4.21</b>	Immunocytochemical results for collagen II localization at t=48 hours (a) control FCs cultured without dexamethasone supplement, (b) FCs cultured with unencapsulated dexamethasone, (c) FCs cultured with dexamethasone aggregates. Original magnification 200X .....	66
<b>Figure 4.22</b>	Net surface charge characteristics following deposition of CS and GelB monolayers onto dexamethasone aggregates and dexamethasone-loaded calcium alginate micropsheres, n=7 .....	69
<b>Figure 4.23</b>	Progressive film thickness following deposition of CS and GelB monolayers, n=3 .....	70
<b>Figure 4.24</b>	Release profile for GelB/CS modified dexamethasone aggregates and dexamethasone loaded calcium alginate microspheres. 50 mg initially incorporated into each drug formulation, n=3 .....	70
<b>Figure 4.25</b>	Steady state release kinetics for dexamethasone loaded calcium alginate microspheres modified with GelB and CS layers. These resultsshow the amount of dexamethasone released in the linear phase, the burst phase is removed.....	71
<b>Figure 5.1</b>	Diagram of experimental setup for LbL film deposition by nebulization.....	78
<b>Figure 5.2</b>	Net surface charge characteristics following deposition of thin films comprised of TiO <sub>2</sub> and PSS functionalized with dexamethasone (■) as a superficial layer and (◆) as a deep layer, n=10 .....	82
<b>Figure 5.3</b>	Progressive film thickness for (PDDA/PSS) <sub>3</sub> /(TiO <sub>2</sub> /DEX)/(TiO <sub>2</sub> /PSS) <sub>3</sub> -TiO <sub>2</sub> generated by dipping (■) and nebulization (◆), n=3 .....	83

<b>Figure 5.4</b>	Progressive film thickness for (PDDA/PSS) <sub>3</sub> /(TiO <sub>2</sub> /PSS) <sub>3</sub> /(TiO <sub>2</sub> /DEX)-TiO <sub>2</sub> generated by dipping (■) and nebulization (◆). Inset shows precursory layers for both methods, n=3.....	85
<b>Figure 5.5</b>	Non-contact AFM scan for nebulized architecture (PDDA/PSS) <sub>3</sub> /(TiO <sub>2</sub> /DEX)/(TiO <sub>2</sub> /PSS) <sub>3</sub> -TiO <sub>2</sub> . Scan area is 30x30 μm <sup>2</sup> . (a) 3-D topographical representation (b) slope shading.....	88
<b>Figure 5.6</b>	Non-contact AFM scan for nebulized architecture (PDDA/PSS) <sub>3</sub> (TiO <sub>2</sub> /PSS) <sub>3</sub> /(TiO <sub>2</sub> / DEX) /TiO <sub>2</sub> . 15x15 μm <sup>2</sup> scan area (a) 3-D rendering, (b) slope shading.....	89
<b>Figure 5.7</b>	Non-contact AFM scan for nebulized architecture (PDDA/PSS) <sub>3</sub> (TiO <sub>2</sub> /DEX)/(TiO <sub>2</sub> /PSS) <sub>3</sub> . 15x15 μm <sup>2</sup> scan area (a) 3-D rendering, (b) slope shading.....	89
<b>Figure 5.8</b>	Non-contact AFM scan for nebulized architecture (PDDA/PSS) <sub>3</sub> (TiO <sub>2</sub> /PSS) <sub>3</sub> /(TiO <sub>2</sub> / DEX). 5x5 μm <sup>2</sup> scan area (a) 3-D rendering, (b) slope shading.....	90
<b>Figure 5.9</b>	Zeta-potential alterations for nebulized films with TGFβ <sub>1</sub> -embedded in deep, double-layered, and superficial modalities, pH 7, n=7.....	93
<b>Figure 5.10</b>	Progressive film thickness for TGFβ <sub>1</sub> in the deep loading modality for assembly using (■) the substrate dipping method and (◆) nebulization, n=3.....	94
<b>Figure 5.11</b>	Progressive film thickness for TGFβ <sub>1</sub> in the double-layered loading modality for assembly using (■) the substrate dipping method and (◆) nebulization, n=3.....	95
<b>Figure 5.12</b>	Progressive film thickness for TGFβ <sub>1</sub> in the double-layered loading modality for assembly using (■) the substrate dipping method and (◆) nebulization, n=3.....	96
<b>Figure 5.13</b>	Live/Dead for TGFβ <sub>1</sub> (A) control, (B) TGFβ <sub>1</sub> in media, (C) TGFβ <sub>1</sub> -deep, (D) TGFβ <sub>1</sub> -double layered, (E) TGFβ <sub>1</sub> -superficial. A and C scale bar=50 μm, B, D, E scale bar=100 μm.....	100
<b>Figure 5.14</b>	MTT results for TGFβ <sub>1</sub> -embedded films produced by nebulization in deep (D), double-layer (DL), and superficial (SF) configurations. Results are compared with positive and negative controls and normalized to Day 4 controls, error bars equal 1 SD, n=3.....	101

<b>Figure 5.15</b>	DNA quantification for cell culture on TGF $\beta$ <sub>1</sub> nebulized substrates. Fluorescence intensity at 538 nm is background corrected to TE buffer, n=3.....	103
<b>Figure 5.16</b>	DIC images of fixed HDFs cultured on substrates with loading modalities (A) control and (B) culture with TGF $\beta$ <sub>1</sub> supplemented in the cell culture media. (C) TGF $\beta$ <sub>1</sub> -deep, (D) TGF $\beta$ <sub>1</sub> -double layer and (E) TGF $\beta$ <sub>1</sub> -superficial. The scale bar represents 25 $\mu$ m.....	105
<b>Figure 5.17</b>	BrdU localization for HDFs cultured on substrates with loading modalities (A) control and (B) culture with TGF $\beta$ <sub>1</sub> supplemented in the cell culture media. (C) TGF $\beta$ <sub>1</sub> -deep, (D) TGF $\beta$ <sub>1</sub> -double layer and (E) TGF $\beta$ <sub>1</sub> -superficial. The scale bar represents 25 $\mu$ m.....	106
<b>Figure 5.18</b>	Fluorescent image of collagen I immunoreactivity in HDFs cultured on TGF $\beta$ <sub>1</sub> -SF substrates at 21 days post-treatment. The scale bar represents 25 $\mu$ m.....	107
<b>Figure 6.1</b>	Illustration of cell encapsulation process, in which the negatively charged cell can be coated with polyelectrolytes (gray and red lines), as well as nanoparticles, or biologically relevant molecules (small circles).....	116
<b>Figure 6.2</b>	Surface charge inversions for encapsulated MSCs in PLL/HA and BMP <sub>2</sub> /HA bilayers .....	117
<b>Figure 6.3</b>	QCM for deposition two bilayers (PLL/HA) and (PLL/BMP <sub>2</sub> ) .....	120
<b>Figure 6.4</b>	Confocal Micrograph for MSC/PLL/HA. Confocal micrographs of MSCs encapsulated within PLL-FITC/HA at (A) three days post-encapsulation and (B) seven days post-encapsulation. Insets show phase micrograph for reference. (Leica Laser Scanning Confocal Microscope, SP2) .....	121
<b>Figure 6.5</b>	Live/Dead images of MSCs encapsulated within three bilayers of PLL/HA. Polyelectrolytes were suspended in deionized water (A-12 hrs post-encapsulation and B-7 days post-encapsulation), 0.5 M NaCl solution (C and D, 12 hrs and 7 days post-encapsulation), and HBSS (E and F, 12 hrs and 7 days post-encapsulation). The scale bars on each image represent 50 $\mu$ m .....	123
<b>Figure 6.6</b>	Bright field image of MSCs within PLL/HA shells at 6 days post-encapsulation. Polyelectrolytes were dissolved in HBSS. The image was acquired with Nikon system. Original magnification, 100X.....	124

<b>Figure 6.7</b>	MTT Assay for MSCs encapsulated within two bilayers of PLL/HA. Control cells were grown without deposition of multilayer shells. Polyelectrolytes were suspended in HBSS and then adsorbed onto MSCs as described above. A student's t-test with $p=0.05$ was used to determine statistical significance (denoted by the asterisks).....	125
<b>Figure 6.8</b>	Adsorption kinetics as monitored by zeta-potential for growth factor incorporation in films (D, DL, SF). Initial amount of cells used was $4.5 \times 10^6$ .....	128
<b>Figure 6.9</b>	QCM for encapsulated HDFs comparing TGF $\beta_1$ in the D, DL, SF Modalities .....	129
<b>Figure 6.10</b>	MTT results for various shell constituents. Control cells were grown without deposition of multilayer shells. Polyelectrolytes were suspended in HBSS and then adsorbed onto MSCs as described above. A student's t-test with $p=0.05$ was used to determine statistical significance, $n=3$ .....	131

## ACKNOWLEDGMENTS

This dissertation signifies both a transitional and culminating stage in my life that has been met with many demands and rewards. The support and encouragement of many must be acknowledged, for without their constant effort and good will, I would not have attained such a successful position.

My sincere gratitude is owed to my advisor, Dr. David Mills. I am thankful for his willingness to mentor me both academically and professionally. Without question, he has been extremely insightful, constantly reassuring, dedicated, inspirational, and understanding throughout my graduate education. I would also like to thank my advisory committee—Dr. Yuri Lvov, Dr. Mark DeCoster, Dr. Steven Jones, and Dr. Patrick O’Neal—for their time and input.

For access to equipment at the ULM School of Pharmacy, I gratefully acknowledge Dr. Alamdar Hussein and Dr. Sami Nazzal. For meaningful discussions, I thank Dr. Tanya Shutava, Nalinkanth Veerabadrán, Shantanu Balakundi, and other members of the Lvov group. I am also grateful to the IfM technical staff, especially Debbie Wood, Scott Williams, Donald Tatum, and Dr. Karen Xu for their assistance in many ways.

To my friends Jorge Roldan, Stephanie Tully, Sarah Bezucha, Anastasia Smith, DeJunne’ Jackson, and Katie Keeton I am grateful for the constant support, coffee breaks, entertainment, babysitting, and therapeutic counseling.

Most important, I am forever grateful to God for blessing me with a wonderful family. I thank my grandparents, Lillian and the late Warren Robinson, Sr., and my parents Georgette and Marvin Stewart for providing me with the tools for success at an early age and instilling in me a desire to “think and dream big”. My sisters, Amber and Sybil, as well as countless other family members have been nothing but uplifting. They have all sacrificed in many ways to get me where I am, and this is certainly an accomplishment of theirs as much as it is an accomplishment of mine. Finally, for being in the trenches with me and sharing in the blood, sweat, and tears of it all, I thank my husband Geoff.

## **CHAPTER 1**

### **INTRODUCTION AND BACKGROUND**

As the life expectancy of an aging US population continues to increase, there is great demand for therapies to heal fractures, replace joints and combat degenerative diseases [1, 2]. In particular, the complex architectural and functional characteristics of orthopedic and dental tissues make attempts to repair, replace, and regenerate these structures challenging. Impairments and disease states such as knee and hip fractures, periodontal disease, and tooth decay require over 600,000 surgeries yearly to restore functionality to the tissues of interest [3, 4]. Pure titanium and titanium alloys currently represent the prime standard for dental and orthopedic implants. A tell tale sign of long-term implant success is early osseointegration, whereby newly formed bone or dentin is directly apposed to the biomaterial surface, without the presence of a connective tissue layer [5]. In general, healthy, youthful patients see positive outcome of their implant surgeries, due to their large bone density. However, older patients are more likely to have low bone densities, and the outcome of their implant surgeries is often less than desirable. Fibrous capsule formation and ultimately implant failure are noted in instances where early osseointegration fails to occur. Thus, there is a need for expedited and enhanced bone-tissue formation at the implant-tissue interface.

Numerous mechanisms have been proposed for enhancing bone apposition to implant surfaces, to exert strict guidance over the cellular response. The currently applied theory is that implants of a higher surface roughness will provide a larger surface area to which existing bone can attach. Roughened titanium surfaces have been achieved through a number of methods, including plasma spraying, grit blasting, and acid etching. Overwhelmingly, these methods have resulted in undesired side effects such as ionic leaching into tissues, peri-implantitis, and surface embrittlement, despite their favorable mechanical characteristics and ability to enhance the adhesion of bone [5]. Surface modification of titanium surfaces with hydroxyapatite or other calcium phosphates can generate the desired increase in surface area and roughness, with an additional benefit. Hydroxyapatite and other bioactive ceramics can provide a biologically attractive layer which recruits certain proteins and further enhances cell attachment. Clinically, the deposition of hydroxyapatite onto titanium surfaces has been achieved by a combination of plasma spraying and grit blasting. The use of high heat and mechanical forces to achieve the coating results in chemical and structural changes to the hydroxyapatite crystal. Additionally, a major drawback of this technique is that it is unamenable to coating implants with complex geometries [5]. The delaminating of the hydroxyapatite coating from the titanium surface is yet another concern, as it can result in implant failure.

Considering the limitations of current orthopedic therapies and treatments, researchers have widely investigated alternative, more biomimetic approaches for restoration and improvement of tissue function. Evolutions in biomaterials, as well as advances in clinical medicine and basic science have made tissue engineering an intense

area of focus. Numerous preliminary and longitudinal works have documented the successes and practicality of engineered biomaterials, particularly those concerning osseous and dental tissue replacement [4, 6-9]. Clear evidence indicates that tissue-engineered products can drastically reduce the need for grafts, improve patient efficacy, and likewise circumvent the associated complications such as repeated surgeries, and immune rejection [10, 11].

Despite significant advancement in the development of dental, orthopedic, and reconstructive tissue-engineered products, there has yet to be one that is completely biocompatible and long-lived. This state of affairs is due principally to limitations in our understanding of cell differentiation, tissue formation, maturation, and remodeling. Thus, the realization of widespread, clinically implemented tissue-engineered products hinges on our obtaining a greater understanding of, and the ability to modulate cell-cell interactions, cell-substrate relationships, as well as the subsequent effects on the production of functional tissue. Each must be accounted for in the design of a tissue-engineered product to ensure functionality over the long term.

### **1.1 The Cellular Niche**

To successfully engineer functional neo-tissue, one must have a firm understanding of the native cellular milieu. For example, the process of bone formation is witnessed during embryonic development, human growth, and injury repair. Cell fate processes, and ultimately tissue architecture are directly modulated through the integration of biochemical and biomechanical signals present in the microenvironment, namely extracellular matrix (ECM) ligands, and soluble factors. It is the interaction of

these environmental cues with cell surface receptors that affect various signal transduction pathways, regulate gene expression, and modify cellular behavior [12, 13].

Within physiologic connective tissues, cells secrete and maintain intimate contact with the ECM, a highly organized, three-dimensional hydrated network of insoluble proteins and polysaccharides [12, 14]. Proteins, such as collagen and elastin, are the primary constituent of the ECM, supplying a structural framework for cells [14, 15]. There are of course, tissue specific variations in ECM content. Bone, for example, is about 25% organic matrix, 5% water, and 70% hydroxyapatite (bone mineral). The matrix of bone is approximately 90-94% collagen (I and V), before becoming mineralized [15]. Other non-collagenous glycoproteins which impart specific functions to bone and dentin are also found in the ECM, such as osteopontin, osteonectin, bone sialoprotein, and their analogues [15].

In addition to providing mechanical integrity for tissue stabilization, the ECM provides instructions for many other complex cellular behaviors through incorporation of other biomolecules, to include polysaccharides classified as glycosaminoglycans (GAGs). With the exception of hyaluronic acid, GAGs are covalently linked to a core protein, forming a proteoglycan. Proteoglycans are found both in the ECM and on the cell surface. Notably, cell surface proteoglycans such as perlecan and biglycan modulate cell adhesion, growth factor signaling, and ultimately tissue patterning [14, 16].

Among the many factors affecting the complex regulatory processes of cellular growth, differentiation, and migration, cell adhesion to the ECM has been noted as one of prime importance. Cell adhesion is a prerequisite for cell viability, cell cycle progression, and phenotypic expression. Abnormalities in the adhesive process often

result in pathologies such as wound healing and blood clotting difficulties, as well as malignant tumors and metastasis [17, 18]. In short, the lack of cell adhesion prevents maintenance of optimal cell function. In the context of tissue engineering and its application of biomaterials, the ability to induce and control cellular adhesion and associated responses directly affects the efficacy of the product.

It has been well documented that integrins, a class of membrane-bound linker proteins, play a key role in anchoring cells to substrates [12, 14, 19]. The study of these proteins has become a key area of focus in understanding cellular behavior, particularly inflammatory and host responses in the context of biomaterials, implants, and tissue engineered devices. Integrins can interact with attachment factors found in serum, adhesive ligands that have been engineered onto a surface, or ligands deposited by cells [20].

## **1.2 Orthopedic and Dental Tissue Engineering**

Contemporary tissue engineering strategies use a combination of cells, biomaterials, and bioactive molecules to restore, modify, repair, or improve tissue function [1, 10, 21, 22]. The synergistic relationship between the aforementioned components is meant to recapitulate the cascade of events common to the natural tissue's development so that cellular maturation is achieved, an extracellular matrix (ECM) is produced, and tissue function is restored. Cellular conditioning is the fundamental aim of a tissue-engineered system. This goal can be achieved by the use of a biomaterial scaffold and differentiating factors alone, or in combination with one another to provide mechanical stabilization, induce cellular signaling, achieve and maintain phenotypic characteristics, and optimize tissue growth.

### **1.2.1 Design Requirements**

Numerous biomaterials, biomolecules, and cell sources have been characterized, investigated, and identified as promising components of dental and orthopedic tissue-engineered systems. Some widely used biomaterials include titania, calcium phosphate and related ceramics. Examples of biomolecules shown to encourage bone formation include members of the transforming growth factor (TGF) superfamily, glucocorticoids, and components isolated from bone, such as dematerialized bone matrix. Overall, the key to producing and organizing functional neo-tissue is the selection of an ideal biomaterial that comprises osteoinductive, osteogenic, and osteoconductive factors.

#### **1.2.1.1 Osteoinductive component**

One essential requirement for correction of bone tissue dysfunction is an osteoinductive constituent [23]. Osteoinduction involves the *de novo* formation of bone in response to biochemical signals. In this process, immature, undifferentiated cells are recruited by chemotaxis, directed to proliferate, and eventually differentiate into bone-producing cells [24]. Soluble molecules such as bone morphogenetic proteins (BMPs) have been examined for their role in bone induction, specifically the differentiation of osteoprogenitor cells [11, 25-28]. Exposure to this class of proteins causes cells to upregulate expression of the bone specific markers alkaline phosphatase and osteocalcin, as well as produce mineralized structures. A recent study investigated the influence of BMP<sub>2</sub> on the osseointegration of roughened titanium screws into osteotomized rabbit femurs. Over an 8-week period, greater bone ingrowth and implant calcification was noted, when compared with non-BMP<sub>2</sub> coated titanium implants.

Other factors shown to direct cells of mesenchymal origin down an osteoblast lineage include ascorbate,  $\beta$ -glycerol phosphate, Dexamethasone (DEX), and 1,25 dihydroxy, vitamin D3, and retinoic acid [11, 27, 29, 30]. Of these factors, one favorable approach is the use of DEX, a synthetic glucocorticoid. As early as 1988, studies involving glucocorticoids and mesenchymal cells were conducted when Grigoriadis reported the positive effects of glucocorticoids on expression of the bone phenotype [31]. Specifically, he found that DEX could cause the differentiation of fibroblast-like cells into osteoblasts. The inclusion of DEX in or on an implant surface could prove very useful in modulating the occurrence of peri-implantitis while also recruiting cells to the implant area.

One concern with this and similar approaches is that the release of the drug or biologically active molecule would need to be well-regulated. For instance, inclusion of a bone-enhancing or anti-resorptive drug in an implant could lead to undesired over-production of bone in the implant area [32]. There is evidence that in supraphysiologic concentrations, growth factors can behave as pro-oncogenes, thus encouraging malignant tumor formation, growth, and metastasis [23].

#### **1.2.1.2 Osteogenic component**

Osteogenic cell sourcing is a requisite player in both the immediate and long-term feasibility of attempts to successfully engineer bone and dental tissues. A major obstacle lies in our present inability to create a renewable source of cells for inclusion in tissue-engineered products. Researchers have successfully isolated mature cells for use in auto-, allo-, and xenotransplants. Harvesting cells directly from the patient eliminates immune complications, however, autologous cells often have limited proliferative capacity, are

difficult to sustain in culture and can result in significant site morbidity [33]. Alternatively, donor cells (either human or non-human) can be used. Indeed, there are serious concerns with allo- and xenotransplantation, particularly the transmission of viruses and infections [33]. Consequently, there has been a movement towards the use of a cell source that can be readily grown, cultured extensively, and differentiated into multiple cell types while producing little, if any immune response [1, 33, 34]

The use of stem cells in tissue engineering and other therapeutic strategies has presented a solution to the problem of “regeneration competent” cells [33]. By definition, stem cells are capable of self-renewal, and have the capacity to differentiate into specific cell lineages [33, 35, 36]. Cell plasticity is a characteristic of natural embryonic development whereby an initial cell mass undergoes several transitions to ultimately produce tissues and organs. A great deal of debate surrounds the use of embryonic stem cells, which are obtained from 3-5 day-old embryos. Although these cells can be manipulated to give rise to nearly all cell types, ethical concerns about obtaining cells from destroyed embryos have stunted their widespread use in therapeutics [34]. Consequently, the use of stem cells from adult sources has become standard practice in tissue engineering applications.

Adult mesenchymal stem cells (MSCs), typically derived from bone marrow, have the capability to grow and renew over long periods of time [34, 35]. MSCs cannot be isolated only from bone marrow or peripheral blood but also from a variety of other sources like umbilical cord blood, adipose tissue and skeletal muscle [37]. While these cells cannot differentiate into all cell types, a number of major cell types can be obtained. These cells are said to be multipotent and can differentiate into a variety of mature cell

types, including those that give rise to bone, cartilage, fat and muscle [35, 38-40]. The lineage commitment is determined by the presence of suitable environmental cues. A number of studies suggest that these cells elicit little, if any immune response, further fueling their potential for use in therapeutics and clinical medicine [41-43]. Significant effort has been devoted to investigating the competency of progenitor cell populations derived from numerous sources including osseous tissues, dental pulp, and mesenchyme [44-46]. In principle, MSCs and other progenitor cells can be incorporated into a tissue engineered system and under appropriate stimuli—biological, chemical, and physical—recruit local cells to needed sites, proliferate, and differentiate into the appropriate cell type for functional tissue improvement.

Indeed, it is important to consider the morphological events concerned with the production of the tissue of interest, for example, the evolution of stem cells to mature osteoblasts or odontoblasts, and the environmental factors that facilitate these processes. The precise mechanisms through which cells can differentiate, dedifferentiate and transdifferentiate in response to environmental cues are largely unclear. Unveiling such intricacies, however, will provide a clear foundation for the design of neo-tissues which mimic native tissue.

### **1.2.1.3 Osteoconductive component**

Osteoconductive materials support the migration, attachment, proliferation, and differentiation of cells through microstructured components. Many novel materials are being developed to have osteoconductive features, and are typically similar in structure to cancellous bone [47]. Calcium sulfates, calcium phosphates, and demineralized bone matrix have been clinically implemented as osteoconductive biologics. Overwhelmingly,

these materials are successful in filling segmental defects, but because they do not induce bone healing, they have been recommended for use only as temporary void-fillers or graft-expanders for orthopedic applications. On the contrary, ceramics such as hydroxyapatite which are chemically similar to bone mineral have seen a great deal of success in supporting the attachment and ingrowth of dental tissue. The release of calcium phosphate into the local implant area increases the availability of biological fluids and causes a layer of natural apatite to form on the surface. It is well documented that this natural apatite serves as a supportive matrix for cellular attachment, and has led to increased clinical success when compared with similar uncoated dental implants [5]. Collagen can also be considered to have osteoconductive properties, as it has been known to enhance the attachment and differentiation of osteoblast-like cells [23, 48].

#### **1.2.1.4 Other factors**

Aside from the aforementioned design requirements, additional parameters should be considered in the design of an implant for bone or tooth repair, to maximize patient compliance and implant success over a long period of time. Ideally, the scaffold or implant should be fabricated so that it is able to withstand the mechanical loads that are experienced *in vivo*. For example, a high elastic modulus may be desirable for a load-bearing implant while a high stress capability could be beneficial for a dental implant. Still, more variations in the specific mechanical requirements would depend on the exact shape and location of the defect. To date, the use of an antibacterial, biodegradable poly (L-lactic acid) PLLA coating on titanium implants is being investigated, to reduce the infection rates associated with traditional titanium implants and support implant longevity [49]. Similarly, the ideal biological implant must be designed with a fine-tuned balance,

such that other factors such thermal stability, nutrient and waste transport, and vascularization are considered [2]. As has been shown here, biomaterials should be engineered to harbor multiple properties to accelerate and optimize tissue formation while also staving off infection and providing the desired mechanical stability. Certainly, these promising approaches to tissue engineering will necessitate a great deal of investigation and testing before they can be implemented clinically. Further experimental strides in the areas of materials science, biology, chemistry and other areas will assist in defining the particular clinical applications of newly developed products for tissue engineering purposes.

### **1.2.2 Dental and Orthopedic Biomaterials**

An examination of the history of biomedical materials reveals that initial goals were largely oriented toward implantation of inert materials. In the 1960s, polyethylene and stainless steel were among the first implanted materials. These first-generation biomaterials were selected based on availability of common materials (wood, gold, etc.) and many of the successes were accidental. Nonetheless, physicians desired to best match the structural properties of the replaced tissue while exerting a minimal immune response [50]. Among other implant materials used for orthopedic and dental tissue stabilization, titanium provides the desirable characteristics of biocompatibility, durability, and strength. However, its implementation does not address the unique problem of osseointegration. That is, complete and direct contact between bone and the implant surface [3, 4, 51]. In many instances, the average lifetime of a bone fixation implant is 10 to 15 years. Studies reveal that implant failure over time can be directly attributed to inappropriate selection of the implant material [51]. This choice promotes

the growth of both the desired bone tissue and unwanted soft, fibrous tissue. Fibrous tissue growth inhibits osseointegration, and eventually leads to disunion of the implant with surrounding tissue.

In the design of second-generation biomaterials, it was imperative to consider bioinertness, along with a new parameter—bioactivity. Bioactive components of an implant were designed to “elicit a controlled action and reaction in the physiological environment” and opened the door to development of bioactive glasses which reacts on the surface to yield hydroxyapatite, a bone equivalent [50]. As mentioned earlier, porous ceramics such as hydroxyapatite and calcium phosphates are being used to provide osteoconductive support, thus facilitating the ingrowth of bone and associated vascularized networks over time [50].

More recently, biostimulatory implantable devices are being tailored to bring about directed cellular responses at the molecular level. The development of these third-generation biomaterials has provided an excellent foundation for and has indeed overlapped into the field of tissue engineering [50]. It is evident that ideally engineered dental and osseous tissues must have the same complexity and properties as their native counterparts at several length scales.

### **1.2.3 Influential Factors for Cell-Substrate Interactions**

The ability to influence cell-cell and cell-substrate interactions is key in the design of tissue-engineered products [52]. It has become well accepted that cell-biomaterial interactions are mediated by protein absorption on the material surface in the context of topography, chemistry, and surface energy [23, 53, 54]. These parameters determine the quality of cell adhesion, attachment, and morphology. Numerous experimental efforts

have investigated cellular response to varied surface compositions and architectures; however, there is a lack of consensus as to what surface features are superior to others for enhancing cell growth and differentiation. It is clear that the degree to which certain factors influence cellular response may be attributed to differences in cell type and maturation state, fabrication methods, and culture conditions, among other parameters [55].

#### **1.2.3.1 Surface roughness**

Surface roughness is an important mediator of cellular functions in the area of biomaterials and tissue engineering, and can ultimately dictate the success or failure of an implant [15, 56]. Several studies have shown that cells are preferential towards specific topographies and roughness on both the nano- and micro-scales. For example, in a study using osteoblast-like cells grown on poly(L-lactic acid) (PLLA) scaffolds, cellular adhesion, uniformity, and growth were superior on island-patterned PLLA when compared with a smooth flat PLLA substrate [56]. Reportedly, osteoblast growth on commercially pure titanium (cpTi) was enhanced on a rougher, machined surface while periodontal ligament fibroblasts preferred smooth, electropolished cpTi [55]. Bone marker expression, however, was highest on smooth polished Ti surfaces versus rough, plasma-cleaned Ti [55]. In later work, osteoblasts cultured on Ti surfaces with a roughness between 4 and 7  $\mu\text{m}$  synthesized ECM, and subsequently produced mineralized nodules [57]. A surface roughness of 1-2  $\mu\text{m}$  is typical for oral implants, having the ability to influence protein adhesion, cell attachment, and mechanical stability [5]. Although cellular dimensions are on the order of microns, the portions of the cell which interact with the extracellular environment are associated with the nano- atomic

scales [15, 58]. Control of scaffold architectures and tissue implants in the nanoscale range is being increasingly accepted as a key modulator of cellular function [52, 59]. For example, *in vivo*, cells interact with nanoscale ECM topography [52, 60]. Within the corneal epithelial basement membrane, proteoglycan bridges are spaced in 60nm increments [52]. To mimic the *in vivo* environment, efforts are being channeled towards the production synthetic ECMs, such as Matrigel, which present natural nanoscale topographies [52]. Moreover, a number of parameters to include peptide density, substrate elastic modulus, and others have been implicated in affecting cell shape, gene expression, and other cellular responses [61].

#### **1.2.3.2 Surface chemistry and surface energy**

A well documented parameter known to critically influence interactions at the implant-tissue interface is surface chemistry, or the presence of certain functional groups. The ability to alter implant surface chemistry has clear implications for control over how cells respond to certain functional groups; however, the exact signaling pathways involved are largely unclear. One thing is sure: the way in which attachment factors and proteins interact with different chemical surfaces has an effect on the subsequent cellular attachment to a particular surface. For example, the incorporation of multiple calcium phosphates onto a surface alters the attachment mechanisms for certain calcium-binding proteins, and ultimately, the attachment of osteoblast cells [55]. The surface energy of a biomaterial relates to the charge density and overall charge. There is support for the hypothesis that cellular interactions are better on a hydrophilic, positively charged surface, due to the chemical makeup of the cell membrane and its net negative charge [62]. Based on this theory, cell adhesion is modulated by electrostatic interactions

between the oppositely charged species (cell membrane and material surface), as well as the covalent binding of proteins (attachment factors) to the substrate, which provide a suitable environment for subsequent cell attachment. However, other factors aside from surface hydrophobicity and charge must be considered to optimize cell adhesion [19]. Again, the much more complex processes, such as the manner in which proteins interact with a surface dictates the cellular response. Thus, certain molecular conditions are created with various surfaces to create a local surface tension and energy of adhesion [57].

### **1.2.3.3 Surface stiffness**

Cells have an inherent ability to probe their environment based on various contractile mechanisms. Recent reports indicate that adherent cells show a behavior known as mechanotaxis, or preferential migration toward stiff surfaces [63]. In response to substrates with certain elastic moduli, cytoskeletal reorganization in terms of myosin and actin filaments occurs. Substrate stiffness determines integrin clustering and the development of focal adhesions; thus cells are involved in a continual feedback process of sensing and responding to their mechanical environment with contractile forces. It is a well accepted fact that cell adhesion and spreading are increased with substrate stiffness, and the role of stiffness is beginning to be investigated in tissue histogenesis, disease states, and other phenomena [64, 65]. Myofibroblast differentiation has been shown to depend on substrate elastic modulus, and other researchers are beginning to investigate the elastic moduli of several other biomaterial surfaces for insight into how cellular behavior and function are affected [63].

As has been shown, numerous critical parameters for consideration must be accounted for to create an optimal cellular milieu in terms of biochemical and mechanical properties, towards to goal of properly repairing or producing functional neo-tissue [11, 21, 66]. These vastly different results concerning preferential cell substrates is proof that certain cell types may be preconditioned for adherence to specific surface features, and that material properties as well as fabrication techniques can profoundly affect cellular response.

### **1.3 Specific Aims and Novel Aspects**

The objective of this research was to address current limitations in orthopedic and dental tissue implants, specifically generation and integration of properly organized neo-tissue at the implant interface. It is clear that organization at all levels--macro, micro, nano, and atomic--has to be addressed if fully functional tissues are to be produced. In particular, the cellular response to nanoscale multimolecular assemblies comprised of soluble instructional factors and bioinert nanoparticles is investigated. It is expected that the design of a cellular milieu which integrates the fundamentals of developmental biology and nanotechnology will lead to increased understanding of how cells retrieve, interpret, and respond to physicochemical information presented to them at the micron and sub-micron levels.

The major challenge in terms of the current state of dental and orthopedic implants is that commonly used materials have suitable mechanical properties, but lack other, more advanced capabilities such as osteoconductivity [15]. Nanofabrication by self-assembly provides the ability to engineer structures with defined mechanical, biological, and chemical properties. Specifically, layer-by-layer (LbL) self-assembly is a

promising mechanism which can be exploited for functionalization of cellular platforms, scaffolds, and implant surfaces. It is a facile method for creation of nanofilms up to 500nm thick, where the resultant monolayers can be comprised of a variety of ionic substances including nanoparticles, enzymes, and proteins. Factors such as molecular chemistry, component density, and the number of layers can be optimized to generate specific film properties and encapsulate biomolecules for controlled release and targeted delivery [67-70]

It was hypothesized that through the use of LbL assembly, cell scaffolds could be functionalized with instructional molecules in an appropriate biocompatible carrier to modulate cellular differentiation and ultimately recreate a suitable *in vivo* microenvironment for improved or enhanced cellular function. Successful implementation of such a system will lead to tailored therapeutic products, which have the ability to produce properly organized orthopedic and dental tissues. The development of an “off the shelf” tissue-engineered product is promising, and in the near future, such products will reduce hospitalization and health care costs associated with surgeries and drug therapy while increasing patient quality of life.

To improve upon the current limitations of orthopedic tissue engineering systems, specifically elucidating certain factors which play a role in crafting the cellular microenvironment, three experimental approaches were investigated. The global project objective and hypothesis were addressed by the following specific aims:

**Aim #1:** Cells respond to biomolecules during development, growth, and repair. The construction controlled release systems containing a model drug, Dexamethasone (DEX) is described. Two schemes are evaluated, direct

surface modification of the drug with nanothin polyelectrolyte layers, and creation of DEX-loaded calcium alginate microspheres, further modified by deposition of polyelectrolyte layers.

**Aim #2:** Nanomaterial surfaces can be used as drug and biomolecule carriers. The development of biocompatible cellular scaffolds with varying surface chemistries and embedded chemical signals is presented. Using selected biocompatible polyelectrolytes and nanoparticles, the traditional LbL technique is modified using nebulization as a means of layer deposition.

**Aim #3:** Encapsulation of cells within protective matrices can be exploited for grafting and transplantation. The results of individual fibroblast and mesenchymal stem cells encapsulation within biocompatible thin-film shells, along with the embedding of signaling molecules within the cell coatings are discussed.

The global challenge at the forefront of tissue engineering is to design a system which combines cells, diffusible signals and supportive architectures such that defective tissue is produced by inducing histogenesis in a specified location. Collectively, these analyses provide a means through which electrostatic LbL assembly fundamentals can tailor substrates in a biologically relevant fashion, assess *in vitro* cellular behaviors, and examine their potential use for *in vivo* studies for dental and orthopedic tissue engineering applications. Specifically, the implications of this work are far-reaching, such as the ability to expeditiously coat implant surfaces with composite materials for enhanced functionality and the promise of improving viability and functionality of transplanted cells by priming in a 3-D environment.

It is hoped that the integration of this work with fundamental research concerning cell sourcing, scaffold characterization, tissue grafting, identification of molecules that control the cell environment, and developmental biologic processes will impact the development and clinical implementation of tissue-engineered technologies.

#### **1.4 Dissertation Overview**

This introductory chapter is followed by a literature review, encompassing a discussion of the fundamentals of LbL assembly and its use in surface modification for biological applications. In Chapter 3, the basic working principles for materials and cellular characterization are presented. Chapter 4 addresses the details of the first aim, specifically the preparation and characterization of calcium alginate microspheres and directly modified Dexamethasone aggregate systems for controlled release applications. Chapter 5 discusses cellular response to growth on multilayered platforms fabricated by nebulized LbL. The evaluation of LbL for creation of biocompatible cellular capsules is addressed in Chapter 6. Last, Chapter 7 provides a summary of the work, conclusions, and future directions.

## CHAPTER 2

### SELF-ASSEMBLY IN TISSUE ENGINEERING

This chapter details recent research efforts aligned with the major topics of the current work. The fundamentals of LbL assembly, as well as existing applications to cell culture and controlled release applications are addressed.

#### **2.1 Self-Assembly of Thin Films**

Fabrication of thin films via self-assembly of molecules is a powerful technique with gaining popularity in biomaterials applications. The ability to manipulate molecules on the nano- and atomic levels provides interesting possibilities for generation of novel materials, which may impart certain cell-friendly properties that encourage superior cell adhesion, modulate cellular differentiation, or promote cell motility. The basis of multilayered thin-film self-assembly is spontaneous interactions of molecules, in the form of ionic, covalent, van der Waals, or hydrogen bonds, which mimics the bottom-up self-assembly processes found in nature [71]. Advantages of self-assembly techniques include resistance to impurities, and limited architectural defects. Such is the case because of the thermodynamics and kinetics of film assembly [71]. Individual molecular chemistry and properties determine bulk film properties and functions. Thus, in the context of tissue-engineered products, film architectures can be tailored to generate novel

structures which may enhance implant coatings, improve wound dressings, or support the timed release of drug molecules.

Construction of thin-films fabricated using the Langmuir-Blodgett (L-B) technique and self-assembled monolayers (SAMs) has been thoroughly investigated in the past. However, pioneering work by Decher et al. using the layer-by-layer (LbL) self-assembly method has shown promise for generation of highly organized multilayer thin films based on alternate adsorption of molecules in oppositely charged aqueous solutions [72]. Over the years, this technology has been adapted to incorporate nanoparticles, enzymes, DNA, cells, and biological molecules, among other charged moieties [73, 74]. Moreover, it is superior to the other methods of thin film assembly because of its mild assembly conditions, facile principle of operation, and ability to generate precisely organized multilayers with advanced functionality.

To give some perspective on the uniqueness of the LbL technique, L-B films and SAMs are briefly discussed. The Langmuir-Blodgett technique involves transfer of molecules from a water surface to solid substrate. L-B films have a high degree of molecular order, a desirable characteristic of thin films [75]. Despite the fact that film thickness of 5 to 500 nm can be produced, L-B films have several limitations. These films are restricted to amphiphilic molecules, can be deposited only on planar substrates of a few square centimeters, and are easily disrupted by thermal or chemical environmental changes [71]. The fabrication of SAMs is based on the interaction of thiol or silane functionalized compounds with a surface. With this technique, films of 2-5 nm can be generated by immersion of a gold or silicon substrate in a solution containing appropriate functional groups. Film buildup can take anywhere from several seconds to

several hours, based on the molecules and solvent properties. The requirement of specific substrate chemistries and functional group modification of layer constituents, coupled with the inability to create films thicker than 2-5 nm, limits the use of SAMs to few industrial applications.

## **2.2 Nanofabrication by LbL Assembly**

The LbL technique produces nanofilms up to 500 nm thick by capitalizing upon electrostatic and covalent interactions between a substrate and subsequent molecular monolayers. These monolayers may be comprised of a variety of ionic substances to include nanoparticles, enzymes, and proteins. Factors such as the type of substance used to form layers, the component density, and the number of layers can be optimized to generate specific film properties. Because LbL is simple, economical, and versatile, it is being used more and more in the assembly of many types of thin films [67].

### **2.2.1 Fabrication of LbL Films by Substrate Dipping**

Substrate dipping, the traditional method of LbL assembly onto planar surfaces is straightforward. Beginning with a charged solid template, the surface is immersed in a polyelectrolyte (PE) solution of opposite charge. The layer adsorbed carries the charge of the solution, due to overcompensation of the surface charge. A critical parameter involved in LbL film assembly is solution concentration; a minimum concentration is required so that numerous ionic groups remain exposed at the surface to reverse the previous charge. An intermediate washing step in ultrapure water is required for removal of weakly adsorbed species [76]. Subsequent layer deposition then occurs in a similar manner, again immersing the newly charged substrate in a solution of opposite charge

followed by an intermediate rinse. Multiple architecture films containing PEs, proteins, DNA, inorganic particles, and virtually any other charged species can be engineered with LbL technology.

Later work in the field has adapted the LbL technique to non-planar substrates, such as colloidal particles, enzymes, dyes, drugs and cells [69, 74, 77, 78]. In a similar manner as with planar LbL assembly, the charged template is immersed in an oppositely charged solution. The only difference is that for non-planar substrates, intermediate washings are carried out via centrifugation, where the centrifugation time and speed are dependent on the size and fragility of the template structure.

One very practical outcome of LbL technology is the ability to tune individual layer thicknesses. Highly standardized layer thicknesses of one to several nanometers can be generated based on the film's chemical composition and assembly pH. These thicknesses can be further modulated by varying the ionic composition of the species solution, where low ionic concentrations solutions tend to result in the thickest films [79]. Reportedly, incorporation of low salt concentrations between 0.1 and 1 M slightly neutralizes the PE chains, causing formation of large loops [80]. The requisite time required to achieve PE layer deposition at a thermodynamic minimum is typically 10 to 15 minutes. After the saturation time, any additional deposition will not lead to increased layer buildup. This phenomenon is what makes the LbL technique extremely accurate. In aqueous solution, LbL films have been shown to double in thickness; in the dried state, approximately 5-10% of water remains within the film architecture [81]. Nonlinear film growth is typical with the first few PE layers, because of uneven charge densities. In this segment of film buildup, thin and unevenly distributed layers are typical until sufficient

charge covers the entire substrate area. Therefore, precursory layers are typically used for accurate characterization of film kinetics [82].

### **2.2.2 Fabrication of LbL Films by Spraying**

The steady-state adsorption of PEs onto a charged substrate is the rate-limiting step for the LbL technique. Traditionally, it is necessary to allow a deposition time of up to 20 minutes for each PE layer, followed by several rinses in pure water at 5-10 minutes each [83]. In recent years, researchers have found that aerosol spraying of PEs onto substrates significantly reduces the LbL deposition time while maintaining similar layer characteristics as conventional substrate dipping [83]. In this manner, the spray axis and substrate are oriented perpendicularly to one another. Due to drainage of excess material, the rinsing step can be omitted while retaining film quality and integrity. Others have extended the spray technology beyond traditional PEs to include colloidal nanoparticles and dendritic compounds [84]. More recently, spraying by ultrasonic nebulization has been explored as a tool for expedited LbL assembly [85]. Details regarding the mechanistic differences between spraying and conventional dipping of electrostatically assembled films are still poorly understood. Yet, the advantages and further possibilities of sprayed multilayers are sure to be continually probed for industrial and biological applications.

## **2.3 Multilayered LbL Films for Biological Applications**

Conventionally, LbL was used for production of systems with novel optoelectronic characteristics [86]. However, as early as 2000, the promise of LbL technology for biological systems was realized. Serizawa et al. were among the first to study

coagulation properties of whole human blood on PE films comprised of chitosan and dextran sulfate [87]. Since then, many others have studied a variety of biological systems at the interface of well-organized LbL-assembled platforms.

The use of multilayered LbL assembled films offers numerous advantages over other self-assembly methods, particularly the ability to modify surfaces independent of their geometry, thus opening the door to production of surfaces with enhanced biocompatible functionality. Today, the versatility of LbL technology in the context of designing unique tissue-engineered products is evidenced by the immense variety of materials incorporated into films, including nanoparticles, protein-growth factors, and other biomolecules to achieve a desired biological effect [67, 68, 88-93].

### **2.3.1 Cell Culture on Polyelectrolyte LbL Films**

Uniquely coated biomaterial surfaces are of increasing interest for the engineering of biomedical systems, especially dental, orthopedic, and wound-healing applications. The use of LbL films as coatings in biological applications offers the ability to tune surface chemistry, topography, and other physicochemical parameters in a desirable manner. Assessment of protein-biomaterial surface interactions is an important first step in controlling immune responses, cell adhesion and other, more advanced cellular functions [94]. Therefore, protein adsorption onto LbL films consisting of various PEs is an intense area of research because of the promising implications for biomaterials.

The design of protein- and cell-selective coatings has been realized by many researchers. Reportedly, serum protein adsorption was detectable on PLL-terminated films but not on PGA-terminated films [95]. This study further found that the adhesion force of chondrosarcoma cells to PLL- and PGA-terminated films followed suit. That is,

cells cultured on PLL-terminated films in the presence of serum showed noticeable adhesion forces, with the highest forces on films of the architecture (PLL/PGA)<sub>9</sub>-PLL while, cells cultured on PGA-terminated films demonstrated little to no substrate adhesion. Tryoen-Toth and colleagues investigated the growth of osteoblast-like and periodontal cells on LbL films comprised of several PEs, including PLL and PGA [96]. Based on morphological observations, expression of phenotypic markers, and cell adhesion assays, their findings indicated that both PEs were suitable film endings, and could be used as coatings for implantable medical devices. PE films with non-specific protein resistant properties have been fabricated by employing a terminal layer of PLL-g-PEG. However, in this same study, biotinylation of the PLL-g-PEG layer allowed specific binding to the protein streptavidin [97]. A multilayered film consisting of the natural PEs, PLL and HA was produced on chitosan-coated glass towards the goal of fabricating a completely biocompatible thin-film [98]. In this instance, blood mononucleolar cell adhesion was decreased on PLL/HA films when compared with adhesion on standard tissue culture plates, likely because of the large volume of HA incorporated within the film assembly. Cai and colleagues demonstrated that the biocompatibility of PDLLA surfaces could be enhanced by the electrostatic deposition of chitosan-containing films [99]. Overall, the protein interaction and apparent cellular tolerances for various PE surfaces could be due to a number of underlying factors, including surface chemistry, roughness, and inherent cellular makeup, however, many of the details regarding these influences are currently unknown.

### **2.3.2 Cell Culture on Nanophase LbL Films**

Although traditional multilayered PE films have been shown to impart some degree of preferential cell adhesion at their surface, these films lack an important parameter which has been shown to affect cellular function—nanotopography. Incorporation of colloids and nanoparticles within the LbL film allow for the presence of this critical component by directly influencing surface roughness. Moreover, a high degree of structural control can be attained through incorporation of nanoparticles within the film [67]. It was demonstrated that by coating CdTe nanoparticle/polycation films with layers of collagen/poly(acrylic acid), cell viability was achieved on otherwise cytotoxic nanoparticle films [100]. In another example, human dermal fibroblast and mesenchymal stem cell adhesion was notably largest on LbL films embedded with TiO<sub>2</sub> nanoparticles when compared with controls. Moreover, incorporation of an increasing number of TiO<sub>2</sub> nanoparticle layers resulted in even greater cellular adhesion, largely due to the increased surface area available for cell attachment generated by successive nanoparticle layers [68, 101]. Most recently, mouse neural stem cell growth and differentiation has been achieved on carbon nanotube/PE multilayer films. Cellular function on these films was similar to that on the traditionally used poly(L-orthine) substrate for neural cell growth. From the results of their work, it is anticipated that the signal transduction capabilities of carbon nanotubes will assist in the generation of unique neuroprosthetics [102]. Unfortunately, only a limited number of reports which aimed to incorporate inorganic nanomaterials within LbL films for biological applications. However, the efforts highlighted here have clearly established the potential for creation

of novel, hybrid nanobiomaterials. They offer the possibility to preserve the nanoparticle material properties while also imparting biocompatibility.

### **2.3.3 Incorporation of Bioactive Species in LbL Films**

Investigations into LbL films functionalized with peptides, proteins, growth factors and other biologically relevant molecules have presented promising opportunities to overcome challenges and obstacles associated with tissue-engineered products, such as peri-implantitis, seamless integration of neo-tissue into existing tissue, uncontrolled tissue growth, and short half lives regarding biomolecule delivery [90, 103]. Interestingly, anti-inflammatory agents such as  $\alpha$ -MSH and piroxicam have been incorporated into PE films [89]. The authors showed a dose-dependent response to these agents, whereby human monocyte response was controlled by the position of the molecule within the film. Alternation of the antimicrobial peptide HEWL with PLGA in the form of an electrostatically assembled film was shown to decrease the colonization of the bacterium *M. luteus*, with increasing affectivity noted for films with larger HEWL content [91]. The facile embedding of ECM proteins in multilayer films has been acknowledged. Fibronectin-terminated LbL films of varying compositions were shown to affect the morphology of human umbilical endothelial cells [93]. Similarly, collagen-I LbL films supported the growth of C2C12 and PC12 cells [104]. Films containing other proteins including  $\alpha$ -lactalbumin, human serum albumin, myoglobin, ribonuclease A, and lysozyme have also been assembled using the LbL technique [105]. The growth factors BMP<sub>2</sub> and TGF $\beta$ <sub>1</sub> were successfully incorporated into multilayered films, having the ability to differentiate embryoid bodies into cartilage and bone when the two proteins were combined within the same film [88]. Acidic FGF/heparin multilayer films were

shown to enhance collagen I production in fibroblasts, specifically when cultured on five bilayered substrates [90]. Furthermore, the films retained their functionality after being stored for three months at -20 C. In another study, BMP<sub>2</sub> release from PAH/DNA and PDL/DNA multilayer films was shown to be greatest when incorporated after each bilayer. Rat bone marrow cells were differentiated into osteoblasts on these films, where calcium deposition was controlled by the specific BMP<sub>2</sub> loading modality [92].

Still in their infancy, these efforts are limited to acute analyses of cellular response on protein-embedded LbL films. It is proposed that numerous factors affect protein release from the film architectures, including diffusion, film degradation, and desorption [89, 106]. The signaling pathways through which cells function in response to these films have yet to be fully elucidated, and are critical for prediction of *in vivo* performance and clinical implementation. These exemplary studies, however, demonstrate the promise of LbL-assembled coatings for the control of cellular interactions with biomaterials.

**CHAPTER 3**

**METHODS AND INSTRUMENTATION USED**

**FOR EXPERIMENTAL QUANTITATION**

**AND ANALYSIS**

This chapter briefly describes the principle of operation for the methods and instrumentation used in quantitation and analysis of experiments conducted in this project.

**3.1 Materials Characterization Methods**

A number of techniques that provide information about LbL film characteristics during and after film assembly. The specific techniques selected are dependent upon the types of data desired. Adsorption kinetics for thin film assembly can be easily monitored by the quartz crystal microbalance (QCM) method, which detects changes in mass on the order of nanograms.  $\zeta$ -potential measurements are taken at each deposition step to provide information about colloidal surface charge properties. Another method, UV-visible spectroscopy generates a linear increase in absorbance with respect to analyte concentration and is helpful in quantifying release characteristics. Various microscopic techniques to include confocal microscopy and atomic force microscopy (AFM) are helpful in visualizing nanofilms properties and surface characteristics for assessment of

film morphology and quality. Ultrasonic nebulization, one of the novel methods used in this work to expedite LbL film fabrication is discussed in principle.

### **3.1.1 Quartz Crystal Microbalance Technique**

The Quartz Crystal Microbalance (QCM) technique has been widely used for real-time characterization of LbL films comprised of PEs, proteins, and other macromolecules. A QCM is a quartz crystal covered with metal electrodes. When an alternating electric current is applied across the electrodes, the crystal oscillates at its fundamental frequency. Upon deposition of mass onto the QCM surface, the oscillation frequency is dampened. This decrease in frequency can quantify the amount of mass and thickness deposited, based on empirical relationships derived from the well-known Sauerbrey equation [107, 108]:

$$\Delta m \text{ (ng)} = -0.87 \times \Delta f \text{ (Hz)} \text{ and } \Delta t \text{ (nm)} = -0.017 \times \Delta f \text{ (Hz)}.$$

Therefore, a 1 Hz decrease in oscillation frequency corresponds to deposition of 0.87 ng in mass or 0.017 nm in thickness. The deposition of proteins, PEs and nanoparticles was monitored through QCM analysis for this work.

### **3.1.2 Zeta-Potential Analysis**

The surface charge of colloidal suspensions is important for monitoring LbL assembly, and is accomplished through zeta- ( $\zeta$ ) potential measurements. Simply put,  $\zeta$ -potential is the measure of the electrostatic interactions within a colloidal system. Under an electric field, particles move through solution to an electrode of opposite charge, and  $\zeta$ -potential measures the potential difference between the particle and the dispersion medium. Thus,  $\zeta$ -potential is directly influenced by pH, ionic strength, and other environmental conditions. It is commonly accepted that particulate dispersions with  $\zeta$ -

potential values with absolute values of 30 mV or more are stable due to the large degree of electrostatic repulsion [109]. In this work,  $\zeta$ -potential measurements were used to monitor film interactions with colloids and cells.

### **3.1.3 Ultraviolet-Visible Spectroscopy**

Ultraviolet-visible (UV-vis) spectroscopy is used to quantify the amount of an analyte within a sample, and was used in this work specifically for quantitation of DEX release. When light at a specified wavelength (UV, 200-400 nm or visible, 400-800 nm) is passed through a sample, a characteristic optical behavior is observed. The light intensity is altered based on the amount photons that are transmitted through or absorbed by the sample. The Beer-Lambert law describes the relationship between the intensity of light passing through a sample and its concentration:

$$A = \epsilon \cdot c \cdot l = \log \left( \frac{I_0}{I_t} \right)$$

Thus, the absorbance (A) of a sample is directly proportional to the absorption coefficient ( $\epsilon$ ), concentration (c), and the path length (l), at a specified wavelength. In a typical acquisition setup,  $\epsilon$  and l are constant, so that the concentration directly influences absorbance [110].

### **3.1.4 Laser Scanning Confocal Microscopy**

Laser Scanning Confocal Microscopy (LSCM) provides the ability to view thin optical sections, an unavailable characteristic in conventional fluorescence microscopy. This optical slicing is accomplished in two ways: single-point illumination of the sample and elimination of out-of-focus light at that point. Laser light passes through the microscope objective, exciting the fluorescent sample; the emitted light passes back

through the objective and a pinhole aperture, thus accepting only the in-focus light at that sample point. The sample is scanned in this way at various points in the x- and y- directions, to reconstruct the image. Furthermore, a 3-D image can be produced by combining 2-D images at various depths [111]. In this study, LSCM was used to image DEX aggregate geometry.

### **3.1.5 Atomic Force Microscopy**

The Atomic Force Microscope (AFM) uses a small probe placed close to a sample surface for acquisition of topographic information at high resolution. The AFM operates by measuring changes in repulsive or attractive intermolecular forces between the probe and the sample surface. In the repulsive “contact” mode, the probe touches the sample, and deflections in height are recorded as scanning occurs. In “non-contact mode”, which was used for this work, the probe vibrates at a fundamental frequency. Changes in the frequency as the probe approaches a sample surface are correlated to changes in the attractive forces, ultimately gleaned information about topography. The characterization of sample surfaces in this way is non-destructive, yet highly resolved [112].

### **3.1.6 Ultrasonic Nebulization**

An ultrasonic nebulizer (UN) uses high-frequency ultrasonic waves to convert liquids into aerosol, with typical output volumes of 1-6 mL/min and particle sizes of 1-6  $\mu\text{m}$ . The power setting determines the output while the frequency at which the UN operates determines the particle size. The UN used in this particular study requires that the solution be placed within a nebulizing chamber. A fan then evacuates the aerosol from the chamber and through plastic tubing [113]. An UN was explored as a means of expediting layer deposition in the LbL process.

## **3.2 Cellular Characterization Methods**

Techniques used to determine cellular response are numerous. For example, the Live/Dead Assay is used as a measure of cell viability and can provide critical information pertaining to cytotoxicity. Assays such as WTS-1 and MTT can give an indication of changes in cellular metabolic activity after a given treatment. Pico-Green can quantify cellular double-stranded DNA content and immunocytochemistry can be employed to confirm the presence of extracellular matrix proteins or other markers indicative of changes in cellular function. In this study, these methods were used to analyze changes in cellular response in a comprehensive manner.

### **3.2.1 Live/Dead Assay**

The Live/Dead Assay provides a simple method for distinguishing between live and dead cells, through the use of a two-color fluorescence based technique. Live cells convert the non-fluorescent calcein acetoxymethyl (Calcein-AM), into the molecule Calcein, which emits a green fluorescence. Dead cells, having damaged membranes, fluoresce red when their nucleic acids bind to ethidium homodimer-1 (EthD-1) or propidium iodide (PI) [114]. This technique is desirable because of low background fluorescence, and its ability to be used for extremely high throughput quantitative analysis such as flow Cytometric.

### **3.2.2 Cellular Metabolic Activity Assays**

Two colorimetric assays for the measure of cellular viability were used in this work, 4-[3-(4-iodophenyl)-2-(4-nitrophenyl)-2H-5-tetrazolio]-1,3-benzene disulfonate (WST-1) and 3-(4,5-Dimethylthiazol-2-yl)-2,5-diphenyltetrazolium bromide (MTT) [115]. These assays are based on the cellular conversion of the tetrazolium salts into

colored formazan products. WST-1 forms a yellow-orange product with a peak absorption between 440-460 nm while the MTT precipitate is blue-purple, having a peak absorption around 570 nm. The product of WST-1 is water soluble, unlike that of MTT. The fact that a solubilization step is not required for the WST-1 Assay can be beneficial; however, not all cell types can process the molecule owing to the wide-use of MTT as a standard measure of cell metabolic activity [115].

### **3.2.3 PicoGreen Assay**

PicoGreen is a fluorescent nucleic acid stain used to quantify double-stranded (ds) DNA within a sample [116]. This assay is highly sensitive, able to detect as little as 250 pg/mL dsDNA within a 200  $\mu$ L sample. A linear relationship between dsDNA concentration and fluorescence emission at  $\sim$ 520 nm provides quantitative information. The contribution of RNA, salts, proteins, and other molecules to the fluorescence signal is minimal with this technique, when compared with traditional Hoechst- or UV absorbance-based dsDNA quantification methods. Thus it is a viable method for quantitation of DNA under various environmental conditions.

### **3.3.4 Immunocytochemistry**

Immunocytochemistry (ICC) is a molecular biology technique that detects specific cellular antigens through the use of antibodies. With ICC, the precise location of the target antigen within a cell can be determined and visualized. To execute ICC, cells must first be fixed, to retain the natural positioning of the antigen. Subsequently, a primary antibody is applied. The primary antibody can be tagged with a secondary antibody which is further coupled with a chromagen, fluorescent marker, or enzyme, depending on the intended application. The ICC technique can be adapted to the

simultaneous detection of several antigens through the application of distinctly different antibodies and markers [117].

## **CHAPTER 4**

### **CONTROLLED RELEASE OF DEXAMETHASONE**

#### **USING ELECTROSTATIC LAYER-BY-LAYER**

#### **ASSEMBLY**

##### **4.1 Introduction**

Tissue-engineered constructs for improvement of function in dental, maxillofacial, and orthopedic pathologies have received much attention in recent years. Although researchers have improved the design of biocompatible, mechanically apt materials, implant failures still occur, largely from inflammation as a result of wear at the surface, loosening, or microbial contamination over the long-term [118, 119]. Control over the implant-host response is critical in extending the longevity of the implant, and improving patient quality of life. The delivery of glucocorticoids by injection is a clinically effective treatment for control of inflammation; however, the duration and potency needed to achieve a certain level of relief is still uncertain [120]. Dexamethasone (DEX), for example, has potent anti-inflammatory abilities but it causes serious systemic side-effects such as increased risk of infection when dosages are not well-regulated [121, 122]. Recent studies have attempted to achieve targeted and timed release of drugs, proteins, and other therapeutics in the context of tissue engineering. Many advanced drug-delivery systems operate on this principle of controlled- release.

Controlled-release technology is advantageous over the traditional drug formulations because a certain amount of the biomolecule is delivered over a specified time in a predictable manner. Such systems can augment bioavailability and specificity while maintaining a specified therapeutic range [123, 124]. Numerous controlled-release systems for inclusion tissue-engineered constructs have been investigated over the past several years [124-128]. It has been well established that delivery systems using biodegradable polymers offer great promise for use in biomaterial applications. In comparison with polymers such as poly(lactide-co-glycolide) (PLG) that are hydrophobic and processed under harsh conditions, hydrated polymers known as hydrogels are hydrophilic, can be easily fabricated, and have protein and polysaccharide constituents comparable to those of natural ECMs [129, 130].

Hydrogels are a class of polymers that swell when they come in contact with water. Parameters such as the structure, chemical composition, and the method and degree of crosslinking, can affect biocompatibility, material properties and performance. In addition, the interface between the biomaterial and surrounding tissue is thought to be improved with hydrogel use, as the crosslinking provides increased mechanical stability at implant site [129, 131]. A great deal of focus has been on the development of degradable hydrogels for drug delivery and tissue engineering applications, mainly as this type of system would not necessitate the removal of an implant. Synthetic hydrogels including poly(lactic acid) (PLA), poly(ethylene glycol) (PEG), and poly(vinyl alcohol) (PVA) offer extreme control of mechanical properties and have been investigated for entrapment of growth factors and cells [131, 132]. Natural hydrogels such as hyaluronic acid (HA), alginate, and collagen are particularly attractive for use as delivery vehicles in

a tissue-engineered system because they are components of, or are molecularly analogous to portions of the natural ECM [129]. Moreover, these molecules are capable of directing cellular behavior, and can be naturally degraded by proteases such as collagenase and hyaluronidase, allowing the process to be facilitated by cells in the engineered tissue [129, 130].

Alginate hydrogels have been widely explored as vehicles for the delivery of drugs, enzymes and cells because of the mild gelling conditions and low toxicity [129]. Alginate, derived from seaweed, is a linear polysaccharide composed of (1-4) linked  $\beta$ -D-mannuronic acid (M) and  $\alpha$ -L-glucuronic acid (G). Crosslinking occurs when divalent cations such as calcium, barium, or strontium, interact with the G monomers [129, 130]. Entrapment of glucose oxidase within calcium alginate microspheres has resulted in successful retention of the enzyme's bioactivity [133].

Recently, researchers have described methods by which DEX could be encapsulated using LbL assembly [69, 70]. Surface modification using this technique provides a diffusion barrier to retard the release of the molecule from both aggregate systems and alginate hydrogels [69, 77, 133, 134]. LbL exerts precise control over controlled-release systems since each adsorbed layer is a few nanometers in thickness. Moreover, the resulting thin films can be tailored to destabilize under specific conditions such as pH, based on the isoelectric points of the layer constituents [77].

Thus, the goal of this work was to construct a controlled-release system containing DEX and evaluate the potential for its use in a tissue-engineered construct. The application of LbL for surface modification of micronized DEX aggregates and dexamethasone-loaded calcium alginate microspheres (DLCAMs) was investigated.

Incorporation of nano-thin layers onto DEX aggregates provides enhanced drug release while layer deposition onto DLCAMs retards drug release, each of which could be valuable for a specified therapeutic application. Acute *in vitro* assessment of the DEX aggregate system is also, included as a means of establishing initial biocompatibility and cytotoxicity results.

## **4.2 Materials and Methods**

We selected two schemes for delivery, (i) physical immobilization of DEX within calcium alginate microspheres, which were further modified with nanothin films using LbL, and (ii) direct adsorption of nanothin films onto DEX aggregate cores. Through use of the LbL process, electrostatic interactions cause the template surface to carry the overall charge of the solution in which it is immersed. The newly charged template can again be immersed in an oppositely charged solution, and the process can be repeated until a desired thickness or layering architecture is achieved. The ability to apply this to any charged surface makes it attractive for drug delivery applications.

### **4.2.1 Preparation of Polyelectrolyte and Drug Solutions**

The polyelectrolytes poly(dimethylallyl ammonium chloride), 20% (PDDA, MW 400,000), poly(styrene sulfonate) sodium salt, 30% (PSS, MW 70,000), chondroitin-6 sulfate (CS, MW 60,000), protamine sulfate from salmon salt (PS, MW 5,000-10,000), gelatin type-A (GelA, MW 50,000-100,000) and gelatin type-B (GelB, MW 50,000-100,000) were purchased from Sigma Aldrich and prepared at a concentration of 1-5 mg/mL in either deionized water for  $\zeta$ -potential characterization (DI H<sub>2</sub>O) or 10 mM phosphate buffered saline (PBS) for other experimental efforts. DEX (MW 392.46,

Sigma) was prepared in DI H<sub>2</sub>O and diluted in culture media or DI H<sub>2</sub>O to give a desired final concentration. The fluorescent marker fluorescein-5-isothiocyanate (FITC, Sigma) was used to label polyelectrolytes for ease of visualization in fluorescence microscopy.

#### 4.2.2 Fabrication of Calcium Alginate Microspheres

Calcium alginate microspheres were fabricated in a manner similar to that used by Brown et al. for entrapment of glucose oxidase (see Appendix A for detailed information) [133]. DEX was incorporated within sodium alginate matrices while stirring with a propeller style mixer (Figure 4.1). A water-in-oil emulsion was formed with the use of isooctane, and ultrasonication was used to reduce microsphere size. Calcium chloride was added as a final cross-linking agent and the microspheres were washed in deionized water before experimentation.

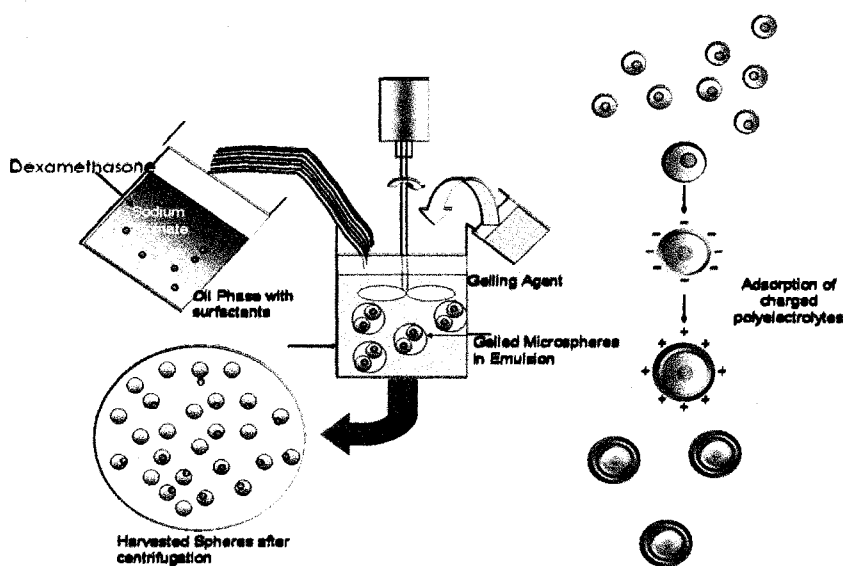
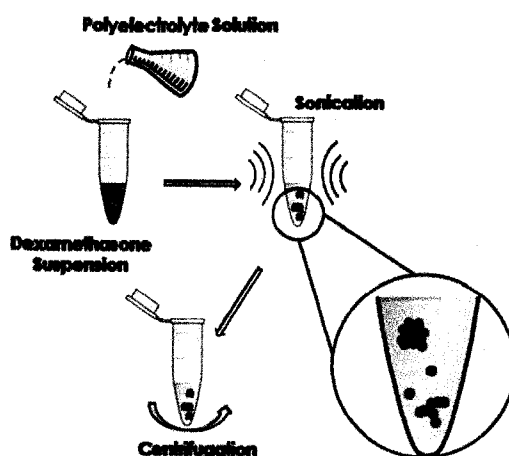


Figure 4.1. Schematic of dexamethasone-loaded calcium alginate microspheres, adapted with permission from Brown et al [133].

#### **4.2.3 Surface Modification of Release Systems Using LbL Assembly**

Deposition of polyelectrolyte layers onto calcium alginate microspheres and drug aggregate cores is straightforward. LbL was begun within two hours of microsphere fabrication. Calcium alginate microspheres were used as an anionic template at neutral pH, and modified with various PS and PSS for assessment of their affects on DEX release. The net charge of DEX can be tuned, based on the pH of the solution in which it is dispersed [69]. Polycations PS and GelB, and polyanions PSS and CS (1-5 mg/mL) were added to either microsphere suspension or drug aggregates and sonicated for 15-30 minutes to reduce the particle size. The mixtures were then centrifuged at 3000 rpm for 5 minutes to remove any excess unadsorbed polyelectrolyte. Three centrifugation washings in deionized water were completed before addition of the complementary PEs to generate a complete bilayer (either PS/PSS or GelB/CS). The process was again repeated (without sonication) until the desired layer architecture was achieved (Figure 4.2).



**Figure 4.2.** Schematic of LbL surface modification of micronized dexamethasone for production of dexamethasone aggregates.

### **4.3 Results and Discussion**

#### **4.3.1 Influence of Layer Architecture on Aggregate Assembly**

DEX, a synthetic glucocorticoid, was chosen as the model drug because of its low cost, anti-inflammatory properties, and use as a mesenchymal stem cell differentiation factor [69]. The addition of polyelectrolyte layers to micronized DEX was expected to both solubilize and delay the release of the hydrophobic drug.

The layering scheme chosen was dictated by the isoelectric point (pI) of each molecule, or the pH at which there is an equal amount of positive and negative charge. Table 4.1 provides the isoelectric points for the molecules considered for use in the layering of the drug aggregates and calcium alginate microspheres as detailed in this chapter.

**Table 4.1** Polyelectrolytes, Biomolecules and their Isoelectric Points

<b>MOLECULE</b>	<b>ABBREVIATION</b>	<b>pI</b>
Chondroitin sulfate	CS	3.2-3.5
Dexamethasone	DEX	5
Gelatin, type A	GelA	7-9
Gelatin, type B	GelB	4.7 – 5.4
Poly(styrene sulfonate)	PSS	2
Protamine sulfate	PS	10-12
Polydiallyldiethyl ammonium	PDDA	12

A number of layering schemes were investigated using  $\zeta$ -potential measurements to confirm charge reversal, an indication of successful LbL assembly (Table 4.2). It was hypothesized that oppositely charged constituents which provided the greatest charge difference with each layer deposition would generate a stiffer capsule, thus slowing diffusion of the drug core. Those combinations that showed surface charge reversal and large changes of magnitude for alternating charges were selected for use in further

experimentation. It is important to note that an additional goal was to use natural or biocompatible polyelectrolytes, because the systems would be evaluated in cell culture. Thus, layer architectures employing PDDA and PEI were not analyzed, despite their strong cationic nature [135].

The shell buildup onto the drug crystals was monitored through quartz crystal microbalance (QCM) and  $\zeta$ -potential measurements. Table 4.2 shows the mean  $\zeta$ -potential readings for ten measurements.

**Table 4.2** Layering Schemes and Surface Charge Measurements for Potential Surface Modifications of Dexamethasone.

<i>SCHEME</i>	<i>LAYER</i>	<i><math>\zeta</math>-POTENTIAL (mV)</i>
A - DEX(PSS/PS) pH 4	DEX	21.62
	DEX/PSS	-50.81
	DEX/PSS/PS	30.66
B - DEX(PSS/GelA) pH 4	DEX	24.57
	DEX/PSS	-50.43
	DEX/PSS/GelA	-43.51
C - DEX(CS/PS) pH 4	DEX	23.60
	DEX/CS	-10.98
	DEX/CS/PS	14.10
D - DEX(CS/GelB) pH 4	DEX	27.34
	DEX/CS	- 11.93
	DEX/CS/GelB	5.34

As shown in schemes A through D, DEX carries a moderate positive charge at pH 4, which is in agreement with the fact that its isoelectric point is 5. At pH 4, the adsorption of PSS onto DEX aggregates causes a strong reversal of the surface charge, to around -50 mV. Given that PSS is a strong polyelectrolyte with pI of 2, a large negative charge is expected.

In scheme A, adsorption of PS onto the anionic PSS layer causes charge reversal to a net positive. Considering that the solvent has a pH of 4, relatively far from the isoelectric point of PS, one would expect a strong positive surface charge. Schemes B

and D involve the use of gelatins. When working at pH 4, GelA is expected to have a positive net charge, based on its pI 7-9. As seen from scheme B in Table 4.2, GelA did not provide the anticipated surface charge reversal when used with anionic PSS. Further investigation of the  $\zeta$ -potential measurements demonstrates that GelA reduces the magnitude of surface charge from -50.43 to -43.51 causing it to become less negative.  $\zeta$ -potential measurement of GelA at pH 4 in DI H<sub>2</sub>O reveals that it carries a small positive charge of 2.23. It is likely that although GelA has a net positive charge under these conditions, its magnitude is not enough to cause complete surface charge reversal. GelA is a much bulkier than DEX and PSS; thus there is no indication that the gelatin molecule cannot “cover” the DEX and PSS molecules during the self-assembly process. In fact, the bulky nature of gelatin and its ability to swell may interfere with the formation of a compact monolayer, leading to disorganization or delocalization of charge, termed “charge stripping” [77]. Another explanation may be that the molecules act other than electrostatically, altering the global charges of the composite layers. Based on these preliminary results, Schemes A and D were selected for further investigation.

### **4.3.2 Comparison of PSS/PS-Modified Release Systems**

#### **4.3.2.1 Zeta-potential measurements**

As shown in scheme A, particles were assembled at a pH 4, where DEX is strongly positive and can be alternated with PSS and PS, which are both strong PEs. Because these structures were to be tested in a cell culture system, the surface charge under physiologic conditions at pH 7 was analyzed. DEX, having an isoelectric point of 5, is negative at physiologic pH [69]. The results for  $\zeta$ -potential characterization of layer

deposition onto DEX aggregates and DEX loaded calcium alginate microspheres (DLCAMs) are provided in Figures 4.3 and 4.4, respectively.

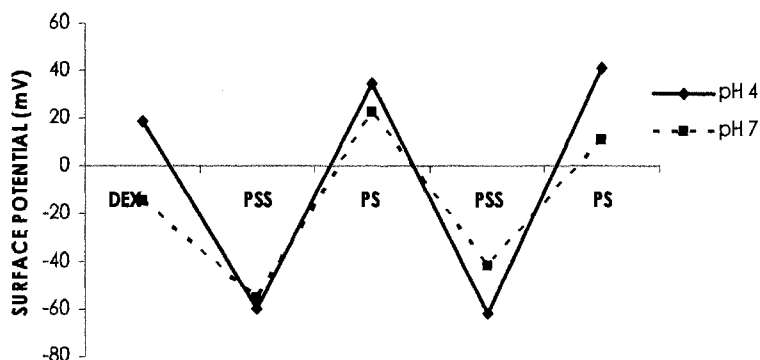


**Figure 4.3.** Net surface charge characteristics following deposition of PSS and PS monolayers onto dexamethasone aggregates assembled at pH 4 and resuspended at pH 7

Comparison of  $\zeta$ -potential measurements for DEX/(PSS/PS)<sub>2</sub> aggregates assembled at pH 4 and resuspended in pH 7 PBS indicate the polyelectrolytes become less charged under simulated physiologic conditions, indicating a decrease in interlayer electrostatic attraction and a potential means of drug release (Figure 4.3). Thus, when aggregates assembled at pH 4 are immersed in pH 7 aqueous solution, such as cell culture media, the PEs are not as charged, and thus have a tendency to bulk up. Moreover, the presence of ions, such as those present within PBS and HBSS further contribute to the bulkiness of the layer architecture. Simply put, the weakened layer interactions induced by a change in pH likely contribute to drug release. Direct tinplating of DLCAMs with two bilayers of PS/PSS reveals that the surface charge reverses with deposition of each layer, demonstrating successful electrostatic assembly (Figure 4.4).

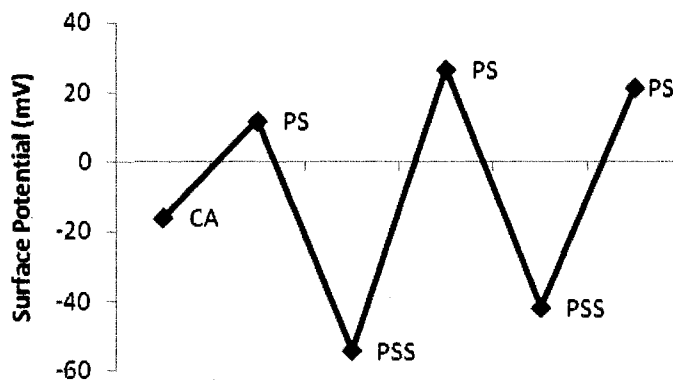


**Figure 4.4.** Net surface charge characteristics following deposition of PS and PSS monolayers onto dexamethasone-loaded calcium alginate microspheres at pH 7.

#### **4.3.2.2 QCM measurements**

As a means of determining the mass deposited and layer thickness of each step, LbL assembly was performed on a silver 9 MHz QCM electrode. After each layer deposition, the electrode was dried in a stream of N<sub>2</sub> and its frequency shift recorded. The thickness deposited on both sides of the electrode with each adsorption step is correlated to a decrease in the resonant frequency of the electrode, based on the following empirically derived relationship [76, 108]:

$$\Delta L = -0.017\Delta F$$

The multilayer architecture (PSS/PDDA)<sub>2</sub>/(PSS/DEX)/(PSS/PS) was characterized to determine the thickness of the PSS/PS bilayer, where the first five monolayers were used as precursors (Figure 4.5).

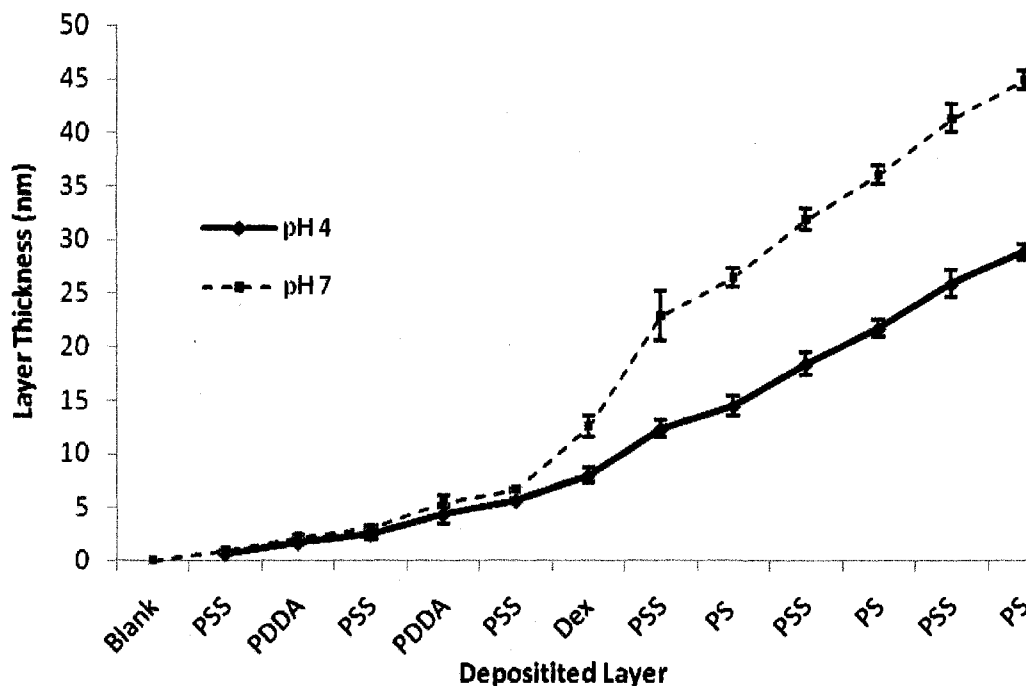


Figure 4.5. Progressive film thickness after deposition of PSS and PS monolayers as obtained from QCM measurements,  $n=3$ .

Precursory layers are essential for subsequent stable film deposition. As shown, linear film assembly is noted with the addition of each polyelectrolyte layer. The slope of the line differs for measurements obtained from precursors (first five cycles) and the active layers of interest. This observation is most notable for the films assembled at pH7. As shown in Table 4.3, comparison of QCM results obtained at pH 4 and pH 7 reveals that thicker coatings are obtained at pH7.

**Table 4.3** Average Monolayer Thickness for PSS and PS Layers Deposited on Dexamethasone Aggregates at pH 4 and pH 7

<i>Polyelectrolyte</i>	<i>Mean Thickness (nm)</i>	
	pH 4	pH 7
PSS	$4.15 \pm 0.17$	$7.04 \pm 2.86$
PS	$2.79 \pm 0.59$	$3.73 \pm 0.29$

One possible explanation for this observation is that the molecules carry a greater charge at pH4, as evidenced from the  $\zeta$ -potential data. Given that the charge is greater under these circumstances, the monolayers are highly attracted to one another, and thus adopt a more flattened conformation when layered. Immersion of these aggregates in a pH7 solution, which is closer to the isoelectric point of PS, causes the polyelectrolytes to assume a bulky conformation. The electrostatic attraction between the PSS and PS monolayers is weakened at this pH, and the resulting layers are thicker. An additional point of observation is that the bilayers generate thicknesses greater than the expected 1-2 nm growth step. Both the solution pH and the ionic content of PBS are likely contributors to creating coiled, bulky layers, resulting in large steps of thickness growth. It is assumed that similar bilayer thicknesses exist for deposition of PS and PSS onto the calcium alginate cores, thus the buildup of these layers specifically onto calcium alginate was not studied.

#### **4.3.2.3 Dexamethasone release testing**

The rate of release of DEX from the PSS/PS modified systems was measured in a Side-bi-Side® diffusion chamber (PermeGear, Inc.). This apparatus uses two, 3 mL chambers (a donor and acceptor), separated by a 0.2  $\mu$ m filter. The temperature was kept at a constant 35 °C, and the samples were stirred continuously to ensure homogeneity. For each of the testing setups, samples were collected at regular time intervals and replaced with fresh PBS of the same volume. The absorbance value for each sample was determined at 239nm, and converted to concentration, based on a predetermined calibration curve for DEX.

The cumulative release profiles obtained from dissolution testing of unencapsulated DEX, PSS/PS surface-modified DEX (termed: DEX aggregates) assembled at pH4, and DLCAMs are shown in Figure 4.6. Over a three-hour period, DEX release was 42%, 48%, and 13%, respectively, for each of the aforementioned preparations. It can be observed that the addition of PSS/PS bilayers to DEX aggregates expedites the drug release while inclusion of DEX within the calcium alginate matrix significantly retards the release rate of the drug.

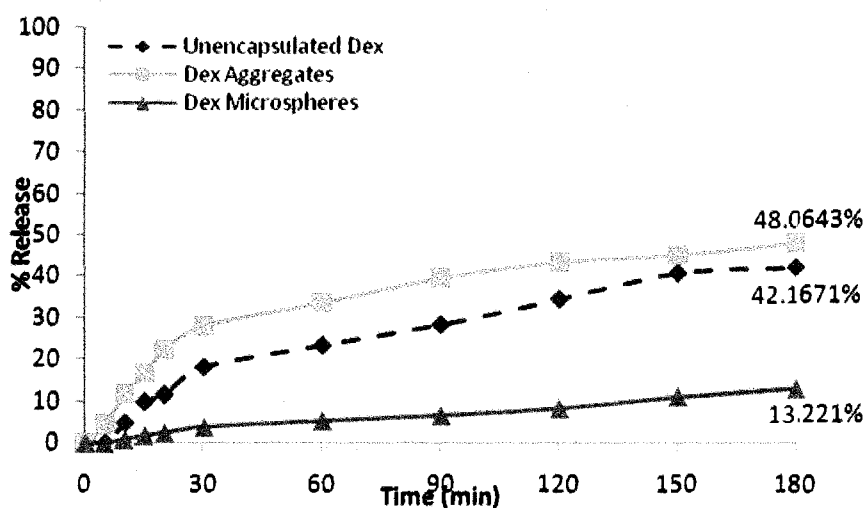


**Figure 4.6.** Release profile for PSS/PS modified DEX aggregates, DEX in alginate microspheres, and unencapsulated DEX, 3 mg preparations used, release testing in PBS.

A substantial burst release (28%) of DEX is shown for the surface-modified aggregate system over the first 30 minutes of drug dissolution. Conversely, only about 4% of DEX was released over the first 30 minutes from the calcium alginate microspheres. The zero-order release kinetics were determined for both drug release systems (Figure 4.7).

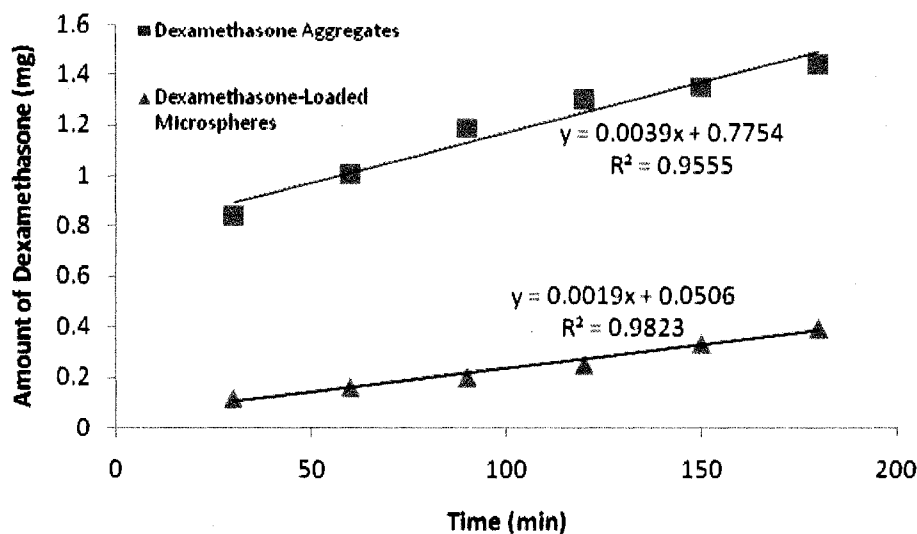


**Figure 4.7.** Steady-state release kinetics for dexamethasone aggregates and dexamethasone-loaded microspheres

Table 4.4 details the encapsulation efficiency of both drug preparations, as well as the amount of drug release per minute, following the burst phase of drug release. The polymer to drug ratio for each delivery scheme is provided. Encapsulation efficiencies were determined by measuring the amount of DEX present in the supernatant after each centrifugation step.

**Table 4.4** Zero-Order Release Kinetics for Dexamethasone Delivery Systems

<i>System</i>	<i>Polymer/ drug ratio (w:w)</i>	<i>Encapsulation efficiency (%)</i>	<i>Release rate mg/min</i>	<i>Time for complete drug release (h)</i>
DEX aggregates	0.00023:1	72.77	0.003	11.86
DLCAMs	250:1	84.14	0.001	48.67

About 27% of DEX is lost when the PSS/PS bilayers are directly applied to the DEX aggregates while only ~16% is lost after application of the same layers onto the loaded calcium alginate microspheres. The differences in encapsulation efficiency are attributed to differences in the drug preparations. With the DLCAMs the drug is

physically immobilized, whereas with the DEX aggregates it is simply entrapped electrostatically. The calcium alginate microspheres release about 1  $\mu\text{g}/\text{min}$ , resulting in a complete drug release over about 48 hours, whereas a release of 3  $\mu\text{g}/\text{min}$  and total drug release time of almost 12 hours is expected for the surface modified DEX aggregates. Although there is not a large difference in the zero-order release, the small total release time of the DEX aggregate system can be directly attributed to the 30% burst effect which occurs initially. A further analysis of the systems indicates that the polymer/drug ratio for the calcium alginate system far exceeds that of the surface modified DEX aggregate system, supporting the result of slower release from the alginate. The drug has a much greater pathlength to travel when encapsulated in alginate, versus being directly coated with nanothin polyelectrolyte films. Increased dissolution of the PSS/PS modified DEX aggregates when compared with the unencapsulated DEX is most likely due to increased motility of the drug. DEX is insoluble in aqueous media; however, adsorption of water soluble polyelectrolyte layers onto the drug crystals increases their solubility allowing the solvated DEX to more freely diffuse.

Notably, it may be desirable to have expedited or slowed release of therapeutics for inclusion in a tissue-engineered product, depending on the application. For example, expedited release may be warranted for release of an anti-inflammatory agent such as DEX, immediately after dental implantation to reduce the occurrence of acute peri-implantitis. The noted burst effect could be useful for the enhanced delivery of certain therapeutics, and could be lessened by either application of different polyelectrolytes, a greater number of polyelectrolyte layers, or a combination of polyelectrolytes that can be crosslinked. Likewise, slower release of growth factors such as BMPs in an alginate

matrix may extend the half-lives of these and other biomolecules, allowing them to be effective over longer time-periods.

#### 4.3.2.4 Confocal microscopy

The geometry and size of the PSS/PS modified DEX aggregates were characterized through confocal microscopy (Leica TCS SP2, Wetzlar, Germany). For this application, the terminal layer of PS was tagged with FITC (Appendix B), so that the resulting architecture deposited onto the DEX core was (PSS/PS/PSS/PS-FITC). Figure 4.8a is an image of several FITC-labeled DEX aggregates, and Figure 4.8b is the fluorescence intensity profile along a selected DEX aggregate.

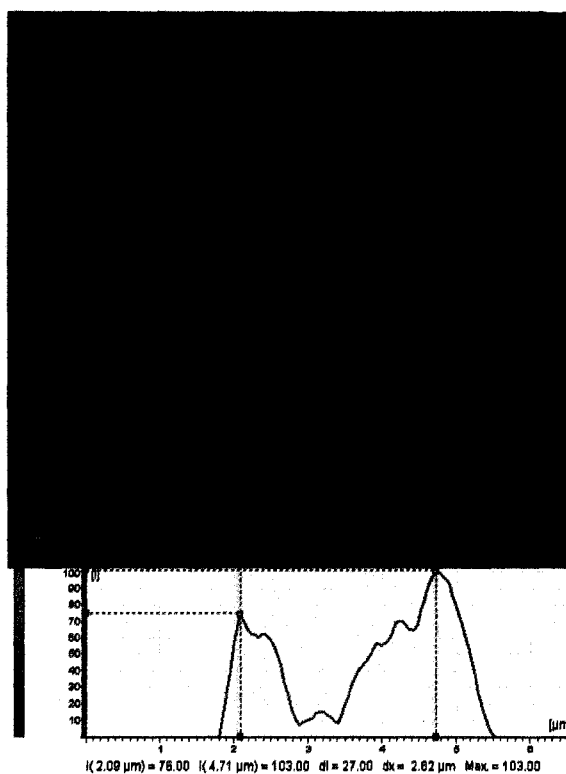


**Figure 4.8.** Confocal micrograph and line profile of PSS/PS modified dexamethasone aggregates

From the line profile, the approximate particle size can be directly obtained, and is 2.62  $\mu\text{m}$ , the distance between the two peaks of intensity. Similar measurements of

other DEX aggregates indicate the average particle size is in the 2-3  $\mu\text{m}$  range. It is widely accepted that polyelectrolyte layers swell significantly in aqueous solution. This is a possible reason for observation of coatings that are greater than the anticipated 10 nm thickness.

#### **4.3.2.5 *In vitro* analysis of fibrochondrocyte response**

To determine whether the presence of the PSS/PS polyelectrolyte films affected DEX activity, and whether addition of the layers induced any acute cytotoxic response, an *in vitro* culture system was selected.

Cartilage tissue was aseptically excised from the temporomandibular joint (TMJ) discs of bovine specimens obtained from the Louisiana Tech University abattoir. Fibrochondrocytes (FCs) from the posterior band were isolated through standard pronase/collagenase enzymatic digestion and filtration. Primary FC cultures were seeded at a density of  $5 \times 10^6$  cell/mL and regularly maintained in Dulbecco's Modified Eagle's Medium (Mediatech, Herndon, VA) supplemented with 10% fetal calf serum (Hyclone, Logan, UT) and 1X 1% penicillin/streptomycin (Mediatech, Herndon, VA) in 37C, 5% CO<sub>2</sub> humidified air. The medium was changed every other day and FCs were passaged at 80% confluence using trypsin/EDTA.

Passage four FCs were used for *in vitro* experimentation. The control group cells were cultured in the presence of complete culture media only (termed: No DEX). The two experimental groups were grown in completed media further supplemented with micronized DEX or PSS/PS surface modified DEX aggregates. Micronized DEX and surface modified DEX aggregates were added to culture media at 10 nM concentration. Assessment of cell viability and mitochondrial activity were used as a measure of cellular

response to the DEX aggregates. Furthermore, immunocytochemical analysis for detection of the extracellular matrix proteins collagen II and aggrecan was performed to determine whether the augmented release of DEX resulting from the PSS/PS layers caused alterations in protein regulation.

#### **4.3.2.5.1 Cell viability and morphology**

The Live/Dead (Biovision, Mountain View, CA) Assay was used as a measure of cytotoxic response to the DEX aggregates. FCs were seeded onto glass coverslips at a density of 10,000 cells/cm<sup>2</sup>, supplemented with completed media, and allowed to attach overnight. After verifying attachment, the existing media was decanted, and appropriately supplemented media (DEX or DEX aggregates) was added for each group of cells. The staining solution was prepared as per the manufacturer's protocol and incubated for 30 minutes at 37C. Cells were observed using a fluorescent microscope (Nikon Eclipse TS 100) coupled to a Nikon Digital camera. For each treatment group, images were acquired at 0, 12, and 36 hours post-media change. Brightfield images were taken for assessment of changes in cell morphology. Live and dead cells were imaged using the FITC and TRITC filters, respectively. The numbers of live and dead cells were quantified using Image Pro Plus software.

Cell viability across all groups was above 90% over the 36-hour experimentation period. As shown in Figure 4.9, no significant difference in cytotoxicity was noted between treatment groups at 0 and 12 hours.

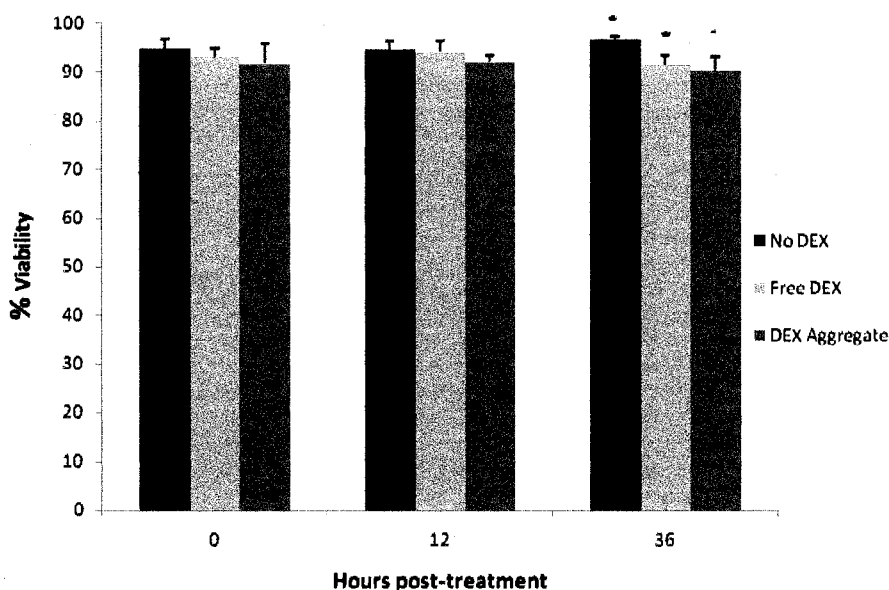


**Figure 4.9.** Percent cell viability for treated and control cultures,  $n=3$ , symbols denote statistically significant difference,  $p<.05$ , one-tailed t-test.

At 36 hours, a significant decrease in cell viability was noted for cells supplemented with DEX and DEX aggregates when compared with controls. However, there was no significant difference between the two treatment groups at 36 hours. This observation leads to the conclusion that 10 nM DEX causes a slight cytotoxic response, but deposition of polyelectrolyte layers does not further affect drug cytotoxicity. In the literature, no standard concentration of DEX used to differentiate FCs. Rather, a range of concentrations are used [136, 137]. It is possible that the cytotoxic response is due to a non-optimal drug concentration either for the cell type or cell density used here. Given that the range of concentrations is generally 1-100 nM, small variations in concentration could profoundly affect cytotoxic response and cellular function.

Immediately after the treatment ( $t=0$ ), each group of cells contains an admixture of three subpopulations of cells. As can be seen in Figure 4.10 A, D, and G, there are ovoid shaped, chondrocyte-like cells, larger polygonal shaped cells, and spindle-shaped

fibroblast-like cells within each sample. The latter two subpopulations also have multiple cellular extensions, which anchor them to the glass substrate. At 12 and 36 hours post-treatment, the control cells (Figure 4.10 B, C) appear to have a similar distribution of the three subpopulations seen initially.

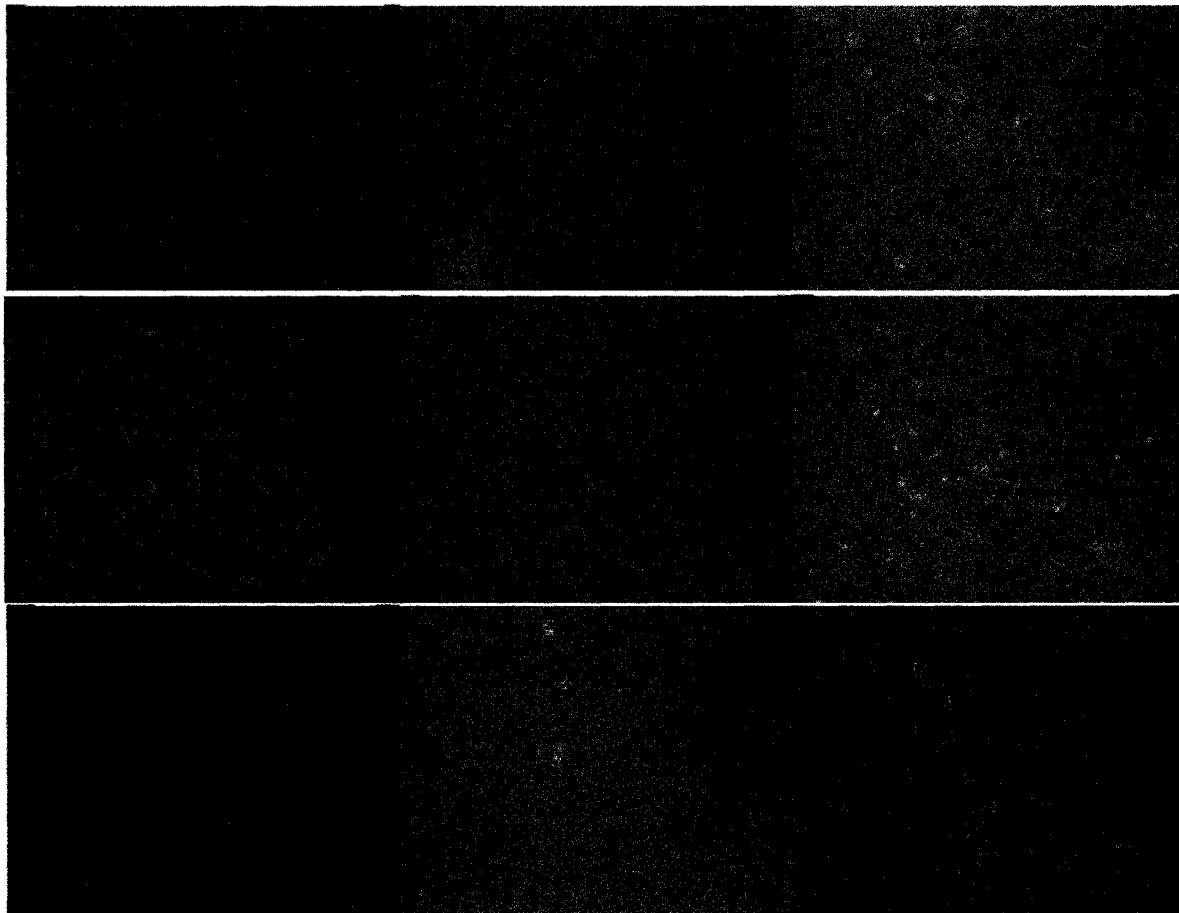


**Figure 4.10.** Cell morphology of treated and control cultures at  $t=0$ , 12, and 36 hours, A-C, controls, D-F, cells cultured in media supplemented with unencapsulated dexamethasone, G-I, cells cultured in media supplemented with dexamethasone aggregates. Original magnification 100X, scale bar=15  $\mu\text{m}$ .

FCs cultured in media containing 10 nM unencapsulated DEX begin to acquire a bipolar, elongated shape at 12 hours post-treatment, with most cells having two filopodia (Figure 4.10 E). There are still other ovoid, chondrocyte-like cells, and few polygonal cells having more than two filopodial extensions. A similar population of cells can be

observed for the FCs cultured in the presence of unencapsulated DEX At 36 hours post-treatment. Interestingly, FCs cultured in media containing surface modified DEX appear to differentiate towards a more chondrocytic phenotype after 36 hours of exposure. This phenomenon can be observed in Figure 4.10 H and I, where rounded cells in lacunae comprise the majority of the cell population. Characterization of DEX aggregates in section 4.3.2.3 of this chapter indicated that release of the drug was expedited when compared with unencapsulated DEX. Therefore, cells cultured in the presence of encapsulated DEX are likely exposed to higher local concentrations of DEX when compared with cells cultured with unencapsulated DEX. It is also important to note that in preparation of the DEX aggregates, sonication was employed and the drug's particle size was greatly reduced in comparison to the manufacturer-provided micronized DEX. For instance, a 30 minute sonication of DEX with the first PE solution caused a particle size reduction from 1934.1 nm and polydispersity of 0.582 to a mean size of 837.3 nm and polydispersity of 0.005. This could account for the increased drug dissolution. There are no noticeable morphological differences between the control FCs (Figure 4.10 A-C) and FCs cultured with micronized DEX (Figure 4.10 D-F), an observation that further supports the conclusion that the surface modified DEX aggregates induce acute morphological changes. Taken together, the results from this study indicate the possibility for DEX to modulate TMJ fibrochondrocyte phenotypic expression in a delivery-dependent manner.

#### **4.3.2.5.2 Cellular metabolic activity**

FC metabolic activity in the presence of DEX-supplemented media (termed free DEX) and surface modified DEX aggregates was determined by assessing the cells'

ability to convert the tetrazolium salt, WST-1 (EMD Chemicals, Gibbstown, NJ) to a colored, water soluble formazan product (see Appendix C for a detailed protocol). Only metabolically active cells can achieve this chemical conversion; thus the mitochondrial activity is an indirect measure of cellular metabolic activity. Proliferating cells are generally more active than non-proliferating cells, so this assay can provide some measure of cellular proliferation based on a standard calibration curve. Although these types of assays are conventionally used for quantitation of cellular proliferation, it is somewhat inaccurate to present data in terms of proliferative or viable cell number since there can be variations between mitochondrial activity within the same cell population [115]. Therefore, the data in Figure 4.11 are presented as a measure of relative metabolic activity, normalized to the untreated cells at t=0 hours.

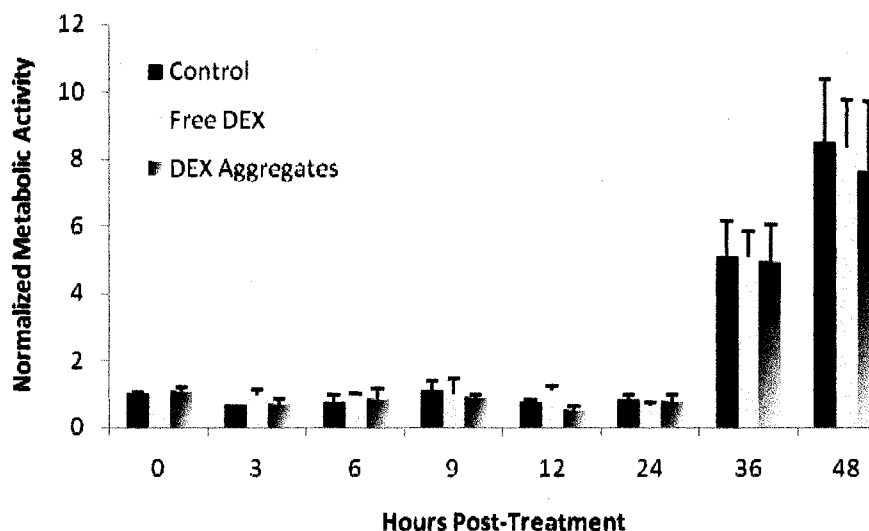


**Figure 4.11.** WST-1 Assay for determination of cellular metabolic activity for fibrochondrocytes cultured in complete media, media supplemented with unencapsulated dexamethasone, and media supplemented with dexamethasone aggregates. Measurement data obtained at 440nm, reference 690 nm using a Tecan Spectrophotometer. Seeding density 10,000 cells/well, n=3.

Across all treatment groups, there is a general trend of increasing metabolic activity of FCs over the 48-hour period. From the results obtained earlier in Section

4.3.2.5.1 it was determined that DEX aggregates are mildly cytotoxic. The results here indicate that while there is a difference between the control group and the FCs cultured with DEX aggregates at 48 hours post-treatment, there is also an increase in metabolic activity between 36 and 48 hours for both the DEX and DEX aggregates group. These increases in metabolic activity are less than those noted for the control and could be attributed to alterations in cellular functionality induced by exposure to DEX. This suggests that there is some inhibition of FC metabolic activity from exposure to both DEX and DEX aggregates. It is possible that DEX aggregates could have a cytostatic effect on FCs; however, this hypothesis would have to be tested through BrdU analysis. Differences in metabolic activity can be attributed to the three FC subpopulations observed earlier in Figure 4.10. Based on the previous analysis of acute FC morphology, it is reasonable that the control and micronized DEX groups would have comparable levels of metabolic activity. On a similar note, 36 and 48 hours FCs exposed to DEX aggregates show less metabolic activity when compared with controls. It is typical to see reduced metabolic activity or proliferation when differentiation is occurring [138]. Again, metabolic activity can to some degree quantitate the number of proliferating cells, but other analyses concerning DNA synthesis or biochemical composition would provide a more complete assessment of cellular response to DEX aggregates.

#### **4.3.2.5.3 Aggrecan and collagen II immunocytochemistry**

FCs were seeded at a density of 20,000 cells/cm<sup>2</sup> and allowed to adhere overnight. Freshly supplemented media was applied containing micronized DEX or DEX structures. The cells were washed with HBSS and fixed with 95% ethanol at 0, 12, 24, 36, and 48 hours post-media change. Immunocytochemistry for detection of aggrecan and collagen

II (mouse monoclonal antibodies) obtained from Calbiochem, LaJolla, CA) was performed using an anti-mouse/HRP/AEC kit purchased from Spring Biosciences (Fremont, CA) Staining was performed using diaminobenzidine (DAB) or the HistoMark ORANGE peroxidase substrate kit (Kirkegaard & Perry Laboratories, Inc., Gaithersburg, MD) and nuclei were counterstained with either hematoxylin or contrast green. See Appendix D for a detailed protocol.

To ensure that no nonspecific binding occurred, negative controls were performed by replacing the primary antibodies to aggrecan and collagen II with blocking serum. Images of the negative controls for aggrecan and collagen II localization in FCs are shown in Figure 4.12 A and B. FC nuclei are stained green while the remainder of the cell body is transparent and lacks a brown color, indicating that the secondary antibodies had no affinity for any endogenous antigens. The results for immunocytochemical localization of aggrecan for the control, micronized DEX and DEX aggregates group at  $t=0$  are presented in Figure 4.13.

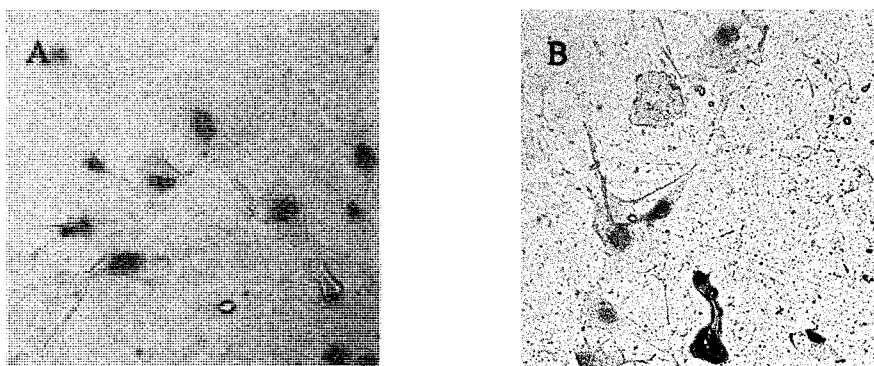


**Figure 4.12.** Negative controls for (a) aggrecan and (b) collagen II. Primary antibodies were replaced with blocking serum. Original magnification 400X.

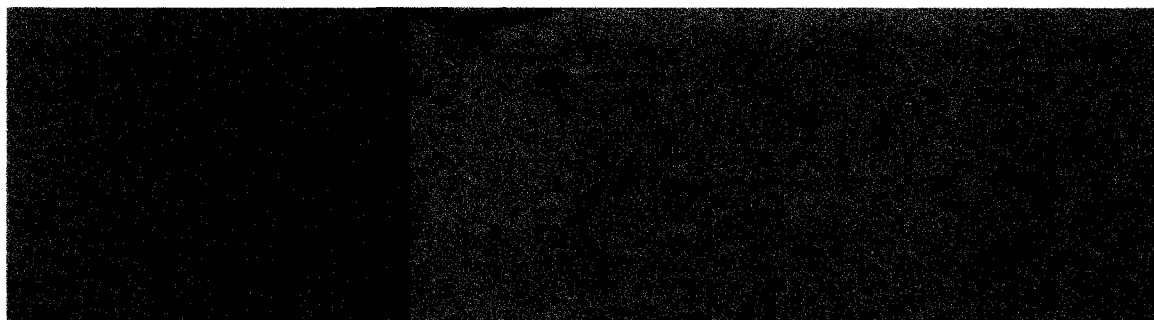


**Figure 4.13.** Immunocytochemical results for aggrecan localization at  $t=0$  hours (a) control FCs cultured without dexamethasone supplement, (b) FCs cultured with unencapsulated dexamethasone, (c) FCs cultured with dexamethasone aggregates. Original magnification 100X.

Figures 4.13 A and B were stained with Histomark Organe and Contrast Green, and Figure 4.13 C was stained with DAB and Hematoxylin. In each case, there is a positive reaction for aggrecan in the extracellular matrix, as is evidenced by the light brown staining outside the nuclei. The presence of various subpopulations of FCs are also observed, including rounded chondrocyte-like cells, spindle shaped fibroblast-like cells, and polygonal cells. Figure 4.14 shows aggrecan localization in FC cells at  $t=12$  hours.



**Figure 4.14.** Immunocytochemical results for aggrecan localization at  $t=12$  hours (a) control FCs cultured without dexamethasone supplement, (b) FCs cultured with unencapsulated dexamethasone, (c) FCs cultured with dexamethasone aggregates. Original magnification 100X

As shown in Figure 4.14 A-C, the FCs show a positive reaction for aggrecan, with those cultured in the presence of micronized DEX having the most intense staining at 12 hours post-treatment (Figure 4.14 B). The other groups (Figure 4.14 A and C) have markedly less staining. Results for 24 hours post-treatment are shown here in Figure 4.15. The images show aggrecan localization in the extracellular matrices for all groups of cells. The amount of aggrecan present for FCs cultured without DEX or with DEX aggregates at 24 hours (Figure 4.15 A and C), appears to be similar to that observed for 12 hours (Figure 4.14 A and C). In comparison with Figure 4.14 B (12 hours), aggrecan production for FCs cultured with micronized DEX has been substantially downregulated (Figure 4.15 B). In Figure 4.16 aggrecan localization at 24 hours post-treatment is denoted by the light-brown staining around the nuclei. Figure 4.17 A-C shows the results of aggrecan ICC for FCs in each group at 48 hours post-treatment. Immunoreactivity with aggrecan is noted in each of the images.

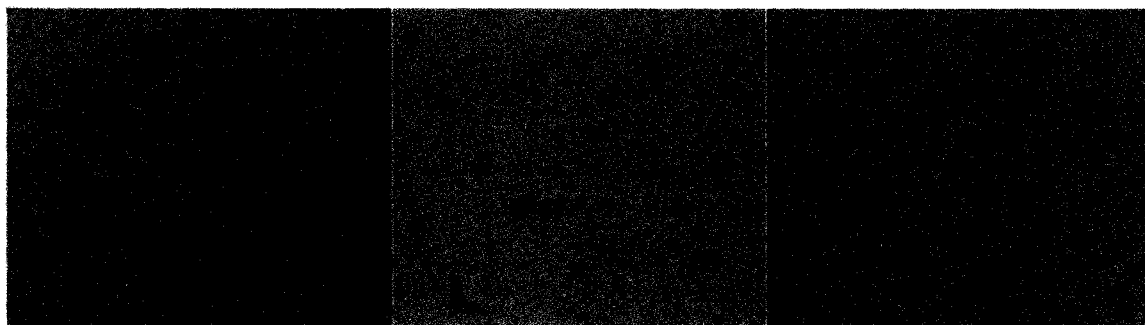


**Figure 4.15.** Immunocytochemical results for aggrecan localization at  $t=24$  hours (a) control FCs cultured without dexamethasone supplement, (b) FCs cultured with unencapsulated dexamethasone, (c) FCs cultured with dexamethasone aggregates. Original magnification 100X.

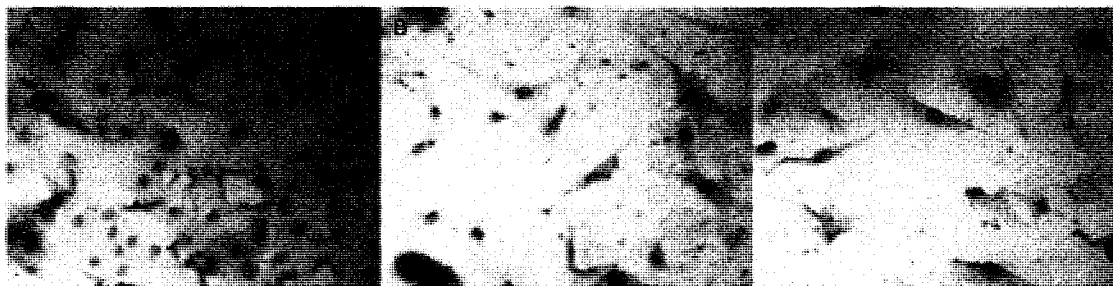


**Figure 4.16.** Immunocytochemical results for aggrecan localization at  $t=36$  hours (a) control FCs cultured without dexamethasone supplement, (b) FCs cultured with unencapsulated dexamethasone, (c) FCs cultured with dexamethasone aggregates. Original magnification 100X.



**Figure 4.17.** Immunocytochemical results for aggrecan localization at  $t=48$  hours (a) control FCs cultured without dexamethasone supplement, (b) FCs cultured with unencapsulated dexamethasone, (c) FCs cultured with dexamethasone aggregates. Original magnification 100X.

The results of collagen II localization in FCs for each treatment group at  $t=0$  are shown in Figure 4.18. At this time point each of the samples have approximately equal intensity staining, indicating similar collagen II content. As shown in Figure 4.19, FCs without any supplement (Figure 4.19 B) have a higher reactivity for collagen II when compared with the FCs cultured with micronized DEX and DEX aggregates (Figure 4.19 A and C).



**Figure 4.18.** Immunocytochemical results for collagen II localization at t=0 hours (a) control FCs cultured without dexamethasone supplement, (b) FCs cultured with unencapsulated dexamethasone, (c) FCs cultured with dexamethasone aggregates. Original magnification 100X.



**Figure 4.19.** Immunocytochemical results for collagen II at t=12 hours (a) control FCs cultured without dexamethasone supplement, (b) FCs cultured with unencapsulated dexamethasone, (c) FCs cultured with dexamethasone aggregates. Original magnification 100X.

Figure 4.20 depicts collagen II localization for each of the FC groups at 36 hours post-treatment. It is noted that intense staining is present for the micronized DEX group (Figure 4.20 B), suggesting that collagen II production has been upregulated since 12 hours. There is medium intensity staining for collagen II in the unsupplemented FC cultures (Figure 4.20 A) and a smaller amount of collagen II present in FCs supplemented with DEX aggregates (Figure 4.20 C).



**Figure 4.20.** Immunocytochemical results for collagen II at  $t=36$  hours (a) control FCs cultured without dexamethasone supplement, (b) FCs cultured with unencapsulated dexamethasone, (c) FCs cultured with dexamethasone aggregates. Original magnification 200X.

Collagen II staining at 48 hours post-media change is shown in Figure 4.21. It may be observed that the FCs supplemented with micronized DEX (Figure 4.21 B) have the least amount of staining when compared with the other treatment groups (Figure 4.21 A and C) at this sample point.



**Figure 4.21.** Immunocytochemical results for collagen II at  $t=48$  hours (a) control FCs cultured without dexamethasone supplement, (b) FCs cultured with unencapsulated dexamethasone, (c) FCs cultured with dexamethasone aggregates. Original magnification 200X.

Both aggrecan and collagen II immunoreactivity was readily apparent in the ECM of FCs cultured under each of the experimental conditions. One significant finding was that aggrecan content was nearly constant over the 48-hour experimental period for unsupplemented FCs and FCs supplemented with the surface modified DEX aggregates. Aggrecan immunoreactivity was strongly positive at 12 hours and then returned to a

baseline level at 24 hours for FCs exposed to micronized DEX. This was the only treatment group for which variation in aggrecan content could be qualitatively determined. One possible explanation for the observed peak in aggrecan production at 12 hours is the amount of DEX available for the cells to uptake. In comparison to the surface modified DEX aggregates, the micronized DEX dissolves more slowly. Notably, the amount of DEX delivered to the cells in micronized form could have been received in an irregular manner, due to the noted burst release in the first 30 minutes. It is likely that the difference in DEX delivery methods and delivery rates led to the differential aggrecan expression. Similar levels of aggrecan staining for the unsupplemented FCs and the FCs supplemented with DEX aggregates over the 48-hour period could be attributed to the quick release of DEX from PSS/PS bilayers. DEX could be losing its bioactivity early on before the cells can respond, or the expedited release of DEX could have a delayed affect on cellular behavior that was not seen in the 48 hour time span.

The data show that collagen II immunoreactivity peaked at 36 hours post-treatment. For the FCs not supplemented with any form of DEX, the weakest reactivity for collagen II occurred at the  $t=0$  time point. The collagen slides for  $t=24$  hours had to be discarded due to errors with the staining protocol, thus there are no results for that time point. In analyzing the ICC results, one must take into account several possibilities. The cell culture medium was not decanted and replaced during the 48-hour time frame. Therefore, at some point the DEX could have lost its potency, given that it has a half life of around 48 hours [139]. Last, it has been well documented that cell seeding density can affect phenotypic expression. This notion could very well explain inconsistencies in morphological results when compared with Section 4.3.2.5.1.

Aggrecan and collagen II were used as markers of fibrocartilaginous matrix characteristics in the bovine TMJ disc, as they are the predominant ECM proteins found in cartilage [140]. *In situ*, collagen II is used to resist compression forces while aggrecan is a critical component of cartilaginous tissues. The immunocytochemical staining for ECM these markers were analysed on a qualitative basis only. In many cases, the results were difficult to interpret and compare because the images were not acquired under the same illumination. Collagen I as well other markers such as vimentin and  $\alpha$ -smooth muscle actin have been differentially expressed in TMJ samples from various species [140, 141]. It would certainly be helpful to test for the presence of these and other molecules to fully characterize and detail changes in phenotypic expression concerning the plasticity of TMJ disc cells. In addition, further long-term, quantitative analyses should be done to better gauge the effect of DEX aggregates on FC behavior.

#### **4.3.3 Comparison of CS/GelB-Modified Release Systems**

DEX aggregates and microspheres were prepared in a similar manner as described previously, however, two different PEs were selected for surface modification. GelB and CS were used as counterions for LbL assembly. The  $\zeta$ -potential measurements for the assembly of thin films onto micronized DEX and DEX-loaded calcium alginate microspheres are presented in Figure 4.22. At pH 7, the negative templates have a surface potential of  $\sim -15$  mV. The addition of the GelB layer confers the surface positively charged, having a  $\zeta$ -potential measurement of  $\sim +10$  mV. Deposition of alternately charged CS reverses the charge, forming a negative surface. The CS layers are weakly charged with surface potentials around  $-5$  mV.

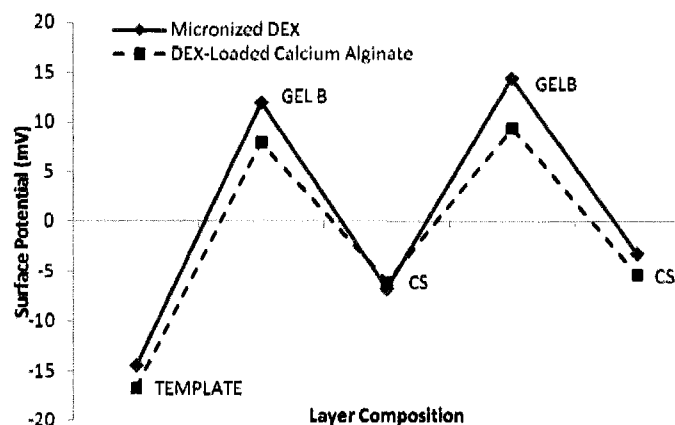


**Figure 4.22.** Net surface charge characteristics following deposition of CS and GelB monolayers onto dexamethasone aggregates and dexamethasone-loaded calcium alginate micropsheres, n=7.

#### 4.3.3.1 QCM measurements

Film buildup onto QCM electrodes was accomplished as previously described. The results for quantitation of CS and GelB bilayers are presented in Figure 4.23. Precursory layers of (PSS/PDDA)<sub>3</sub> were used before deposition of the layers of interest. Each CS growth step is roughly 1.5 nm in thickness while GelB layers are nearly 10 nm thick. The molecular weights of CS and GelB are 60 and 50 kDa, respectively. Larger growth steps are allowable for GelB deposition steps since the molecule is a hydrogel and is able to bind water [69].

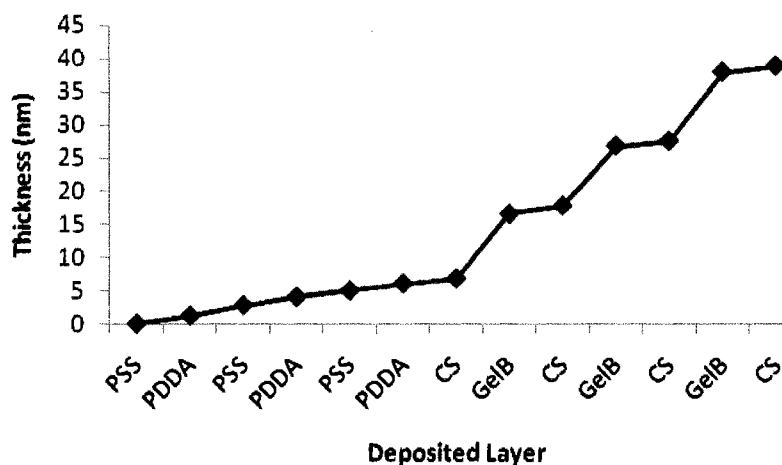


Figure 4.23. Progressive film thickness following deposition of CS and GelB monolayers, n=3.

#### 4.3.3.2 Dexamethasone release testing

The release profile for DEX from DEX aggregates and DLCAMs modified with two bilayers of GelB/CS is provided in Figure 4.24. Over a seven-hour timeframe, DEX aggregates release approximately twice as much drug when compared with the DLCAMs.

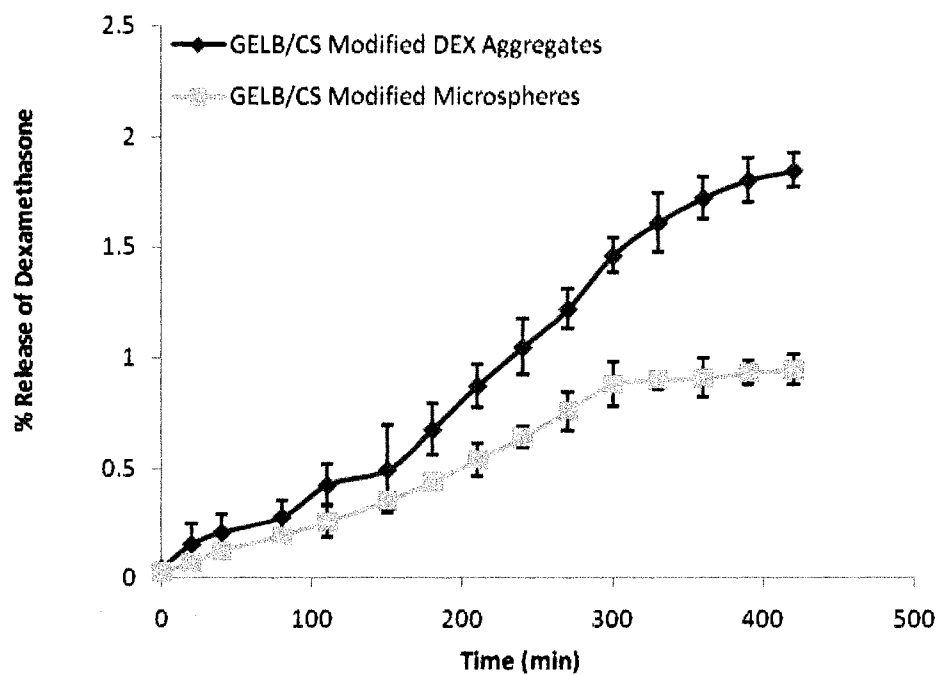
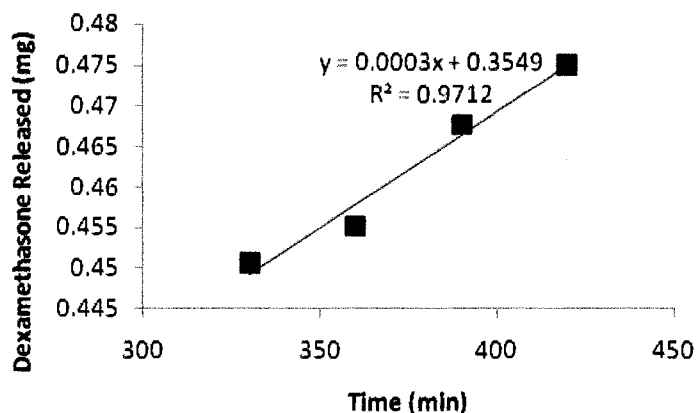


Figure 4.24. Release profile for GelB/CS modified dexamethasone aggregates and dexamethasone loaded calcium alginate microspheres. 50 mg initially incorporated into each drug formulation, n=3.

GelB/CS modified DEX aggregates release roughly 2% of the drug after 420 minutes of testing while the surface modified DLCAMs release approximately 1%. The DEX aggregates follow a near linear release profile over the testing period, however, it is possible that the system is still undergoing burst release, and that the profile shown here is not the steady-state behavior of the system. The particle size reduction as a result of the sonication step in combination with the thin layer barrier likely contribute to expedited DEX release from the surface modified aggregate systems when compared with the alginate microspheres.

The release behavior of DEX from the microsphere preparations is biphasic, having two distinct release profiles. The burst release of DEX from the microsphere preparations occurs over the first 300 minutes of dissolution. The steady-state behavior of the system is presented in Figure 4.25.



**Figure 4.25.** Steady state release kinetics for dexamethasone loaded calcium alginate microspheres modified with GelB and CS layers. These results show the amount of dexamethasone released in the linear phase, the burst phase is removed.

The zero-order behavior of the GelB/CS modified DLCAMs shows a release rate of 3 ng/min, having a theoretical release time of 114 days, or nearly four months. The *in vitro* behavior of this system would have been tested to verify these results. The results in

this portion of the study were not compared with unencapsulated DEX, however, use of non-linear PE layers, such as gelatin, onto DEX aggregates has been shown to significantly retard the release of DEX, when compared with enhanced release typical from aggregates modified with smaller PEs [69].

#### **4.4 Conclusions**

In this work, the LbL fabrication technique was used to assemble nanothin biocompatible layers onto DEX aggregates and DLCAMs (calcium alginate microspheres containing DEX). The acute *in vitro* response of bovine TMJ fibrochondrocytes to the DEX aggregates was established, whereby exposure to DEX in the surface-modified form causes differentiation toward the chondrocyte phenotype after 36 hours. In terms of collagen II and aggrecan immunoreactivity, a transient response to the DEX aggregates was noted, indicating that protein production can be modulated based on the delivery mechanism. Moreover, comparisons of the DEX aggregates with DLCAMs showed expedited DEX release, both when modified with bilayers of PS and PSS or CS and GelB. A higher encapsulation efficiency and lengthier drug release time was noted with DLCAMs. However, the drug loading of the DEX aggregates is over 1000 times greater than that of the DLCAMs, and can certainly be advantageous when fabrication costs are considered. The *in vivo* cell characterization results are quite promising, in that the fibrochondrocytes can be encouraged to assume a different phenotype. Given the results from cell culture, this system could be implemented or used in conjunction with a TMJ disc implant for control of associated inflammation as well as cell morphology and protein expression. However, fibrochondrocyte response in this work was limited to a period of 48 hours. Future work should investigate the response of other maturation

states (passages), as well as this and other cell types such as progenitor populations to both the aggregates and microspheres over the long term, in the context of protein production, morphology, and biochemical composition. Moreover, the precise mechanisms involved in drug release from each of the preparations is unknown. The promise of extended release over a four-month period was demonstrated by incorporating of 50 mg of DEX into the calcium alginate microsphere preparation; however, it is unknown if the drug can retain its potency for such a time period. Additional characterization of the systems concerning structure, geometry, chemical makeup would be helpful in uncovering their degradation properties over the course of their use, and is critical for clinical implementation. Similarly, protein interactions with the surfaces are an important indicator of *in vivo* behavior.

Key questions still remain to be answered; however, the results demonstrate the potential for LbL surface modification as a means of controlling the delivery of proteins, biomolecules and other therapeutics within a tissue-engineered construct while retaining biological activity. The use of this technology for incorporation therapeutics within a scaffolding system is presented in Chapter 5.

**CHAPTER 5**

**FABRICATION AND CHARACTERIZATION OF**

**CELL-SUPPORTIVE SUBSTRATES USING**

**NEBULIZED LAYER-BY-LAYER**

**ASSEMBLY**

**5.1 Introduction**

Successful *in vitro* tissue engineering strategies must account for the reproduction of the native tissue's microenvironment. The dynamic cellular microenvironment requires deployment of growth factors in a controlled manner to initiate, assemble, and maintain proper tissue architecture [142, 143]. *In vivo*, a host of growth factors including TGF $\beta$ s, BMPs, VEGF, and FGFs play a critical role in cellular maturation, matrix deposition, and associated protein synthesis [23, 142, 144-146]. In particular, BMPs have a marked influence on the morphogenesis of progenitor stem-like cells into mature cells. *In vitro* regulation of these molecules offers a significant challenge, given that growth factors have short half lives and diffuse rapidly from their point of origin [147]. For example, the growth factor BMP<sub>2</sub> is rapidly degraded *in vivo* by extracellular body fluids, having a half-life of 7-16 minutes [23, 86, 148].

In a clinical setting, regulation of an effective concentration requires intermittent addition of the therapeutic molecule at the desired site via injections or infusion, which

can be especially uncomfortable to the patient. Furthermore, administration of supraphysiologic amounts of growth factors is expensive, can lead to systemic toxicity, and have the potentiality cause the proteins to behave as prooncogenes [23].

Strategically assembled multilayer scaffolds offer much potential in creating an optimal cellular microenvironment which can incorporate necessary proteins, growth factors and other biomolecules. Since its inception in 1992, layer by layer assembly (LbL) has been exploited for a number of purposes, including the design of electronic, optical, and biological systems [72, 149, 150]. Fabrication of nano-organized thin films via LbL is accomplished through sequential deposition of oppositely charged polyelectrolytes (PEs) onto a charged template. Traditionally, the substrate is immersed in a PE solution of opposite charge allowing for surface charge reversal, and then rinsed to remove any unbound PE. Subsequently, the newly charged surface undergoes the same process. The cycle of immersion in an oppositely charged PE followed by rinsing in water is repeated until the desired layer architecture has been reached. The steady-state adsorption of PEs onto a charged substrate is the rate-limiting step for the LbL technique. Traditionally, it is necessary to allow a deposition time of up to 20 minutes for each PE layer, followed by several rinses in pure water at 5-10 minutes each [151]. Recently, methods for expeditious fabrication of electrostatically organized thin-films have been described using aerosol spraying. Spraying of PEs onto substrates significantly reduces the required PE contact time while maintaining similar layer characteristics as conventional substrate dipping [150, 151]. To expand upon these recent efforts, ultrasonic nebulization was explored as a tool for creating multilayered, multicomponent assemblies.

This work combines the principles of electrostatic layer-by-layer nanoassembly with ultrasonic nebulization for expedited layer fabrication. Efforts in our lab have been directed towards the use of nebulization to create biocompatible substrates for a variety of tissue engineering applications. In our previous works multilayer architectures functionalized with active layers of protamine sulfate (PS), chitosan (CHI), and chondroitin sulfate (CS) were fabricated using nebulization. Mist distances of 1.5 or 3.0 cm generated films up to twice the thickness achieved from dipping when polyelectrolyte concentrations between 3-5 mg/mL were used. An additional observation noted in the case of nebulized films was the evenly distributed surface, as demonstrated through AFM studies. Moreover, mouse mesenchymal stem cells (MSCs) showed preferential attachment to the nebulized substrates over a two-day period when compared with similarly organized dipped substrates. These preliminary results demonstrated the potential to create superior cellular microenvironments through nebulization [85].

The work detailed herein extends our past efforts to include analysis of nanoparticle- and growth factor-embedded nebulized nanofilms. Nebulized films comprised of  $\text{TiO}_2$ , a material widely used in orthopedic and dental implants were produced. Similar films were also fabricated containing  $\text{TGF}\beta_1$ , a potent growth factor implicated in the wound-healing process. Film growth was monitored using the QCM method, and surface topography was imaged with AFM. The results demonstrate that varying surface morphologies of dense, nanoscale organization can be created using nebulization for production of LbL films.

## 5.2 Materials and Methods

### 5.2.1 Preparation of Polyelectrolyte, Nanoparticle, Protein, and Drug Solutions

For this work, materials suitable for LbL assembly were selected. Those chosen include traditional PEs with charged functional groups, charged colloidal nanoparticles, and water soluble proteins. The PEs poly(dimethylallyl ammonium chloride), 20% (PDDA MW 400,000) and poly (styrene sulfonate) sodium salt, 30% (PSS) were purchased from Sigma Aldrich and prepared in sterile deionized water (DI H<sub>2</sub>O) at a concentration of 3 mg/mL. Titanium Dioxide (P25 Degussa AG, Germany) diameter ~21 nm, was prepared in DI H<sub>2</sub>O at a concentration of 6 mg/mL and adjusted to pH 4 with dilute HCl. A stock solution of 0.4 mg/mL Dexamethasone (MW 392.46, Sigma) was prepared in DI H<sub>2</sub>O and further diluted in either cell culture media or DI H<sub>2</sub>O to give a final concentration of 10 nM. Growth factors were prepared according to the supplier's recommendations. Briefly, 1 µg of TGFβ<sub>1</sub> (ProSpec, Israel) was reconstituted in 4 mM HCl containing 1 mg/mL of Bovine Serum Albumin (Sigma) to yield a stock solution of 1 µg/mL. The growth factor stock solutions were then diluted with either cell culture medium or buffer, as appropriate for experimental use, to give a final concentration of 10ng/mL. Table 5.1 details the molecules used and their associated isoelectric points.

**Table 5.1** Isoelectric Points of Polyelectrolytes, Nanoparticles, and Biomolecules

<b>MOLECULE</b>	<b>ABBREVIATION</b>	<b>PI</b>
Dexamethasone	DEX	5
Poly(styrene sulfonate)	PSS	2
Poly(dimethylallyl ammonium chloride)	PDDA	12
Protamine Sulfate	PS	10-12
Titanium Dioxide	TiO <sub>2</sub>	5
Transforming Growth Factor Beta-1	TGFβ <sub>1</sub>	8.9

### 5.2.2 Fabrication of Multilayered Substrates

Glass slides (VWR) were first immersed overnight in 70% isopropyl alcohol (IPA). They were then cleaned by sonication in 70% IPA for 20 minutes and allowed to air dry. An ultrasonic nebulizer (SigmaNeb) was used to deposit various 14-layered architectures onto the negatively charged slides. To carry out the assembly process, ~3 mL of PE, nanoparticle, or drug solution was placed in the nebulizing chamber. The glass substrates were sprayed with the appropriate solution for varied times and mist distances. When indicated, substrates were rinsed between layer cycles by 30 seconds of nebulization in DI H<sub>2</sub>O. As illustrated in Figure 5.1, layers were deposited by vertically orienting glass substrates so that the receiving surface was perpendicular to the nebulizer output. The orientation of the substrate in this manner allows for maximal drainage of the solution runoff [151]. Three bilayers of (PDDA/PSS) were deposited as a precursory foundation for further layer assembly.

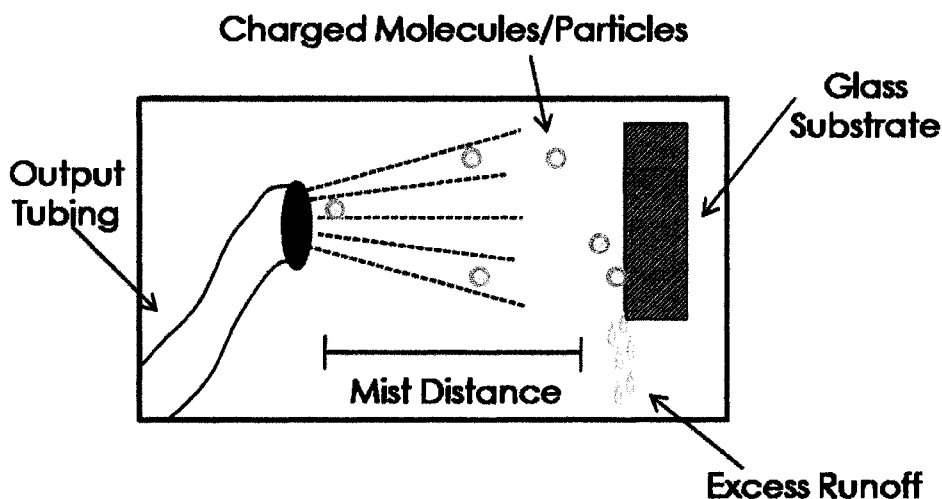


Figure 5.1. Diagram of experimental setup for LbL film deposition by nebulization.

An important facet of this work was the evaluation of how various deposition parameters affected film properties, before use for *in vitro* testing. An initial set of experiments was performed in which LbL films comprised of PEs and polymers were assembled while individually varying nebulization parameters and the resulting films were analyzed for thickness and surface morphology. The results of these preliminary experiments are provided in Table 5.2. The deposition parameters selected for further experimentation was based on these findings.

**Table 5.2** Qualitative Outcome of Varying Individual Nebulization Parameters for LbL Films Composed of Synthetic and Natural PEs.

PARAMETER	Range	Qualitative change over parameter range
Solution concentration (mg/mL)	3 – 5	No noticeable trend
Regulator output (intensity)	Min-Max	Increase in thickness
Mist distance (cm)	1.5 - 3.0	Decrease in thickness Decrease in surface clustering and aggregation (density)
Mist time (sec)	30 – 180	Increase in surface clustering and aggregation (density)
Rinse time (sec)	0 – 30	No effect

The polyelectrolytes PSS, PEI, CS, and PS were used to generate 14- or 15-layered multiassemblies. In general, there was no noticeable trend in thickness change for solution concentrations between 3 and 5 mg/mL as measured with QCM. In some instances, concentrations of 3 mg/mL yielded higher film thicknesses than those assembled using 5 mg/mL. In other situations, the exact opposite was observed. Most likely, the chemical composition of the substance has some influence, and solution concentration alone had no significant effect on film thickness.

The regulator output was dialed to the maximum position for generation of the thickest films within a specified time frame. Conversely, film deposition performed when the regulator output was at the minimum setting resulted in thinner films. A mist distance of 1.5 cm generated slightly larger film thickness than those assembled using a mist distance of 3.0 cm. The higher film thickness at 1.5 cm, however, was also met with a higher level of particle clustering and aggregation when compared with those films whose surface was 3.0 cm away from the nebulizer output. These observations raise the issue of a tradeoff between film thickness and film density. It was assumed that film density could possibly be adjusted by fine-tuning the concentrations of each PE, however, this was outside the scope of the current work. Increasing the mist time from 30 sec to 180 sec led to an increase in clustering and aggregation. Rinsing of the substrate was found to be unnecessary, most likely because any loosely adhered moieties are simply removed in vertical run off from the surface.

Based on these results, it was determined that suitable LbL assembly via nebulization could be achieved using a mist distance of 3.0 cm, and a deposition time of 30 sec without rinsing between layers. The regulator was kept at the maximum setting, and the PE concentration was used within a range of 3-5 mg/mL.

### **5.3 Results and Discussion**

#### **5.3.1 LbL Nebulized Thin Films Functionalized with TiO<sub>2</sub> and Dexamethasone**

Four layering schemes were identified for characterization and testing. The glass substrates were assembled so that each contained one layer of DEX and alternating layers of TiO<sub>2</sub> nanoparticles with PSS. The specific architectures along with the nebulization

parameters used for film fabrication are summarized in Table 5.3. In each case, the layers were sprayed for 30 seconds at a distance of 3 cm from the substrate. The substrates were rinsed after deposition of each layer. The first architecture,  $(\text{TiO}_2/\text{DEX})/(\text{TiO}_2/\text{PSS})_3$  was assembled onto the precursory  $(\text{PDDA}/\text{PSS})_3$  nebulized films. In an identical manner, a film with architecture  $(\text{TiO}_2/\text{PSS})_3/(\text{TiO}_2/\text{DEX})$  was deposited onto the precursory layers. These films were created for comparison of DEX release, as the first film contained DEX near the bottom of the film (D-DEX) and the latter contained DEX in a superficial position within the film (SF-DEX). Similar films of architecture  $(\text{TiO}_2/\text{DEX})/(\text{TiO}_2/\text{PSS})_3/\text{TiO}_2$  and  $(\text{TiO}_2/\text{PSS})_3/(\text{TiO}_2/\text{DEX})/\text{TiO}_2$ , termed DEX-D- $\text{TiO}_2$ , and DEX-SF- $\text{TiO}_2$ , respectively, were also fabricated to determine the effect of adding a terminal layer of  $\text{TiO}_2$ . The materials characterization and comparison of these films with conventional dipping are included in this section.

**Table 5.3** Layering Architectures for Nebulized Films Functionalized with  $\text{TiO}_2$  and Dexamethasone.

SCHEME	ARCHITECTURE
DEX-D	$(\text{PDDA}/\text{PSS})_3/(\text{TiO}_2/\text{DEX})/(\text{TiO}_2/\text{PSS})_3$
DEX-SF	$(\text{PDDA}/\text{PSS})_3/(\text{TiO}_2/\text{PSS})_3/(\text{TiO}_2/\text{DEX})$
DEX-D- $\text{TiO}_2$	$(\text{PDDA}/\text{PSS})_3/(\text{TiO}_2/\text{DEX})/(\text{TiO}_2/\text{PSS})_3/\text{TiO}_2$
DEX-SF- $\text{TiO}_2$	$(\text{PDDA}/\text{PSS})_3/(\text{TiO}_2/\text{PSS})_3/(\text{TiO}_2/\text{DEX})/\text{TiO}_2$

### 5.3.1.1 Zeta-potential measurements

Thin film surface charge and layer interactions were studied through  $\zeta$ -potential measurements (Zetaplus Zetasizer). Anionic polybead carboxylate microspheres (Polysciences Inc.) of diameter 450 nm were prepared at a concentration of 10 mg/mL. The desired layering scheme was achieved by immersing the microsphere solution in the

nanoparticles, drug, or polyelectrolytes for ten minutes in a sequential fashion. Following deposition of each layer, the microspheres were rinsed thrice in DI H<sub>2</sub>O by centrifugation at 5000 RPM for five minutes. The net surface charge characteristics for the nebulized films embedded with TiO<sub>2</sub> and DEX are presented in Figure 5.2.

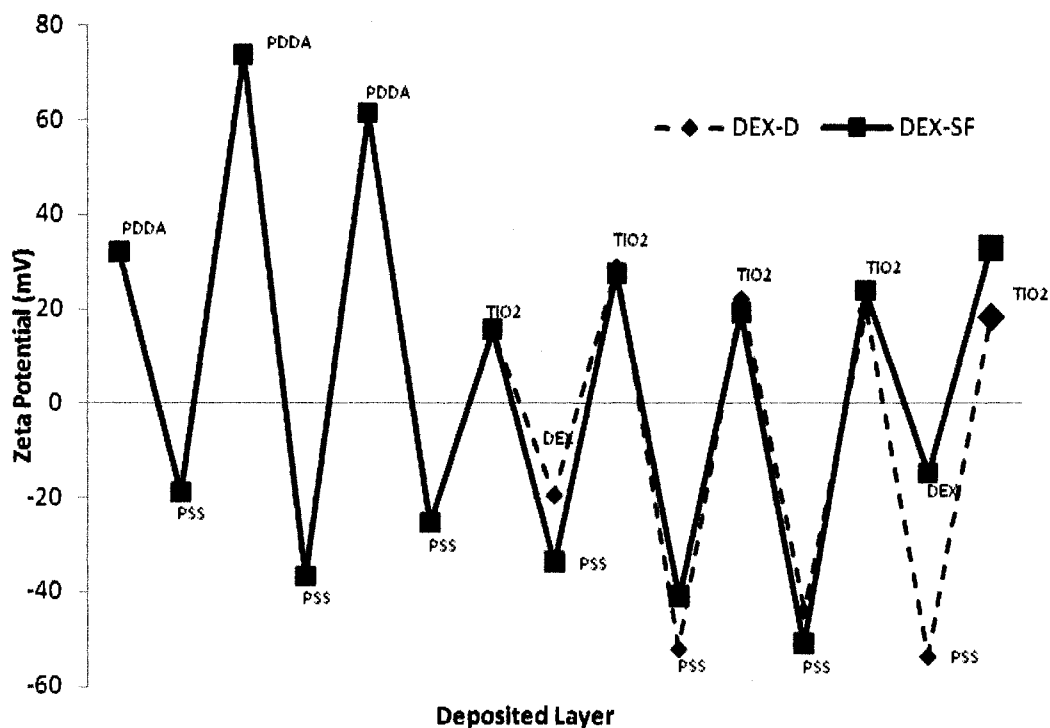


**Figure 5.2.** Net surface charge characteristics following deposition of thin films comprised of TiO<sub>2</sub> and PSS functionalized with dexamethasone (■) as a superficial layer and (◆) as a deep layer, n=10.

The first six layer cycles shown are the precursory layers. The potential of the first PDDA layer is ~ +30 mV. After deposition of PSS, the surface is negatively charged (~ -20 mV). With each additional layer, there is charge alternation from positive to negative. The noted charge reversal is an indication of overcompensation of the previous charge and indirect verification of film growth. One can notice that when DEX is embedded deep within the film, the surface charge at that layer is ~ -20 mV. When that same layer is replaced with PSS, the surface charge carries a larger magnitude of ~ -30

mV. In a similar manner, inclusion of DEX as a superficial layer results in a surface charge of  $\sim -20$  mV and replacement of that layer with PSS yields a surface potential of  $\sim -50$  mV. The  $\text{TiO}_2$  nanoparticle layers stabilize around  $+25$  mV, with terminating layers of  $+18$  mV for DEX-D films and  $+33$  for DEX-SF films.

### 5.3.1.2 QCM measurements

For the purpose of monitoring film buildup, silver electrode QCM crystals (Supplier) with a 9 MHz resonant frequency were used as substrates. After immersion in or spraying of the appropriate solution, the crystal was dried in a stream of  $\text{N}_2$ . The frequency shift after deposition of each layer was monitored and correlated to a change in thickness. The comparison of film thicknesses generated by dipping and nebulization for the architecture  $(\text{PDDA}/\text{PSS})_3/(\text{TiO}_2/\text{DEX})/(\text{TiO}_2/\text{PSS})_3/\text{TiO}_2$  is provided in Figure 5.3.

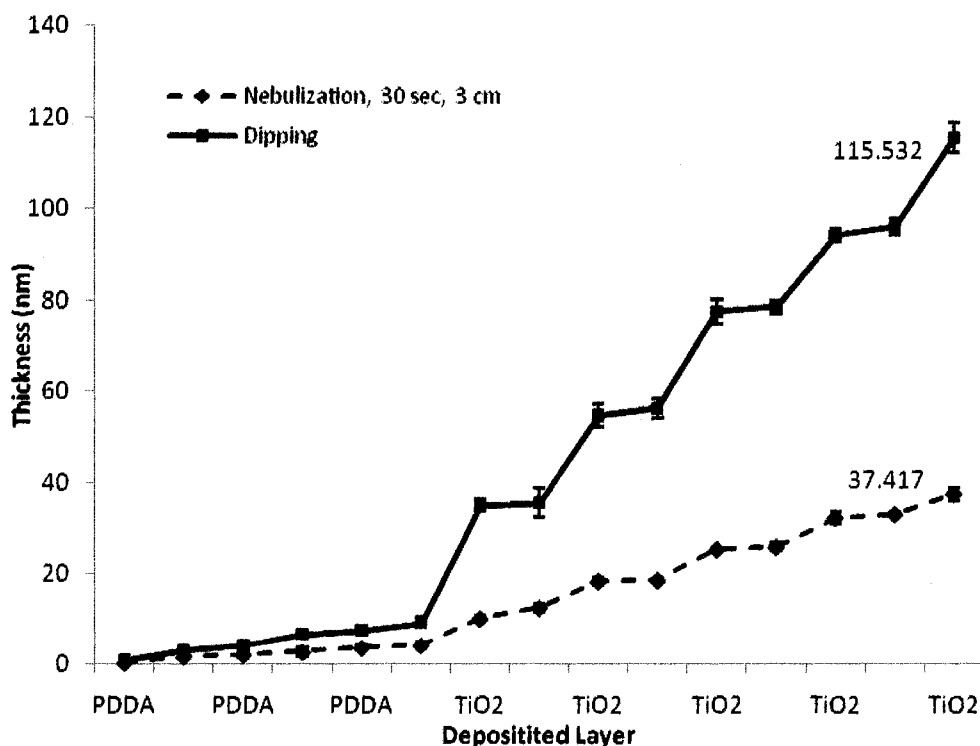


**Figure 5.3.** Progressive film thickness for  $(\text{PDDA}/\text{PSS})_3/(\text{TiO}_2/\text{DEX})/(\text{TiO}_2/\text{PSS})_3/\text{TiO}_2$  generated by dipping (■) and nebulization (◆),  $n=3$ .

The film growth for the precursory layers is small for both the nebulization and dipping methods, owing to the fact that there is inhomogeneous charge density on the substrate surface with these initial layers. The dipping process produces a precursory thickness of 9.613 nm, when compared with 4.131 nm for those produced by nebulization of the same layer configuration. A bi-phasic linear increase in film thickness is noted for both film preparation methods. The total thickness generated from dipping is 117.419 nm while nebulization produces a total film thickness of 37.417 nm. For the film produced by dipping, the first TiO<sub>2</sub> nanoparticle layer measures around 20 nm, however, the subsequent layers measure around 10 nm, about half the particle size. The difference in thickness between the first and successive TiO<sub>2</sub> layers is attributed to packing and interconnectivity of the PE layers with those of the nanoparticles [152]. The even further reduced layer thickness (~ 5nm) for TiO<sub>2</sub> produced by nebulization could be due to the fabrication procedure. Conceivably, the ultrasonic pulses induce particle size reduction.

For this film configuration, DEX is located near the bottom of the film. The approximate monolayer thickness for DEX is around 2 nm for nebulization, and around 0.5 nm for the dipping method. The small thickness of the DEX monolayer generated by dipping is attributed to two possibilities. First, the previous TiO<sub>2</sub> layer could have facilitated loss of DEX subsequent to the rinses in water. Additionally, a lengthier deposition time may have been necessary for the optimal thermodynamic stability to be achieved. It is well understood that drugs, proteins, and polypeptides assume much more complex molecular configurations than polyelectrolytes, and thus their adsorption kinetics differ greatly [153].

Similar precursory coatings of three bilayers of PDDA/PSS were used in the second layer architecture, however DEX was incorporated near the surface of the composite film, so that the configuration was  $(\text{PDDA/PSS})_3/(\text{TiO}_2/\text{PSS})_3/(\text{TiO}_2/\text{DEX})\text{-TiO}_2$ . As shown in Figure 5.4, the precursory layers follow a linear trend with deposition of each layer.

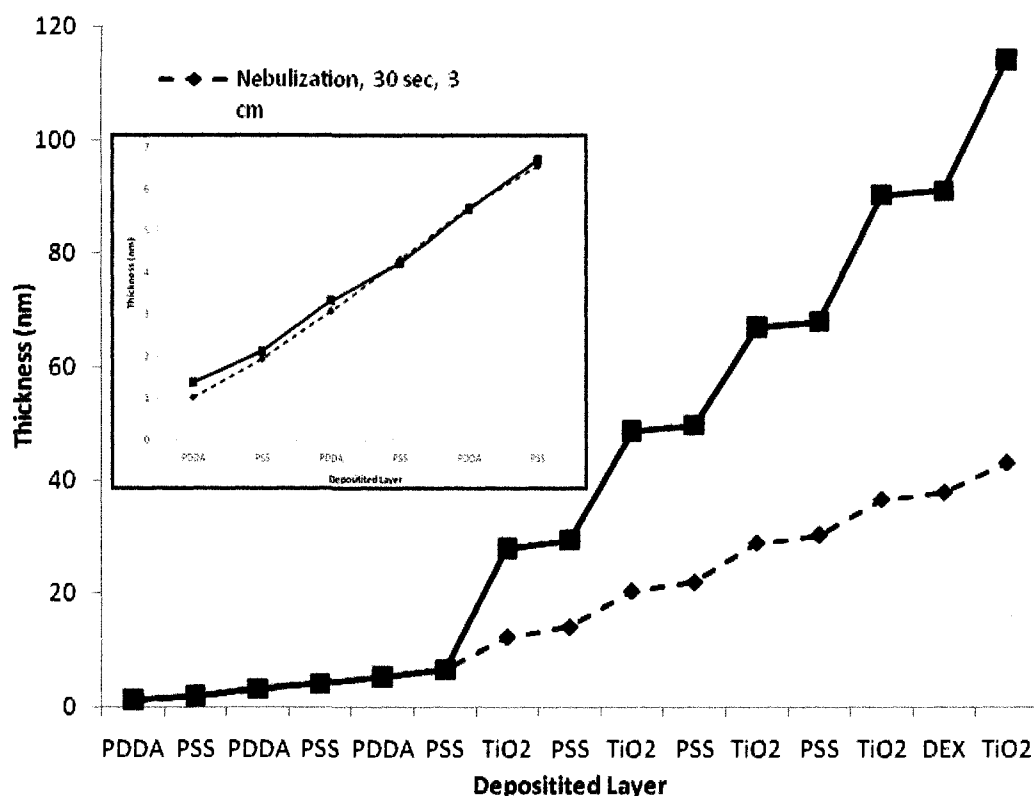


**Figure 5.4.** Progressive film thickness for  $(\text{PDDA/PSS})_3/(\text{TiO}_2/\text{PSS})_3/(\text{TiO}_2/\text{DEX})\text{-TiO}_2$  generated by dipping (■) and nebulization (◆). Inset shows precursory layers for both methods,  $n=3$ .

The cumulative precursory layer thicknesses generated by nebulization and dipping are 6.71 nm and 6.57 nm, respectively. An increase in the slope of film growth is noted with addition of the TiO<sub>2</sub> nanoparticle layer for both preparations, however, the TiO<sub>2</sub> layer is much thicker when the conventional dipping method is employed. The cumulative thickness achieved with dipping is 114.07 nm while that achieved through

nebulization is 43.04 nm. The average layer thicknesses produced by both the dipping and nebulization techniques are elaborated below in Table 5.4.

**Table 5.4** Average Layer Thicknesses Produced by Dipping and Nebulization.

LAYER	THICKNESS (nm)	
	Dipping	Nebulization
TiO <sub>2</sub>	20.6 ± 2.39	6.11 ± 0.65
TiO <sub>2</sub> /PSS	21.2 ± 2.31	7.75 ± 0.71
DEX	0.63 ± 0.18	1.78 ± 0.73

The data in Table 5.4 show that on average, nebulization produces smaller TiO<sub>2</sub> nanoparticle layers and larger DEX layers when compared with those generated using the conventional dipping process. For each bilayer, the PE/PE pairs create thinner layers than the TiO<sub>2</sub>/PE pairs. This phenomenon is easily explained, given that the nanoparticles are rigid and have fixed dimensions. In comparison, polyelectrolytes are pliable and can adsorb electrostatically to achieve a thermodynamic minimum. It is thus noted that the thickness of the layers is largely dependent on the incorporation of TiO<sub>2</sub> nanoparticles. As stated earlier, smaller TiO<sub>2</sub> layers are likely produced because the energy of the ultrasonic pulses breaks the nanoparticles up into smaller pieces. One way to verify this would be to comparing particle sizes of the drug as received from the supplier and after ultrasonication. The DEX layers produced by nebulization could be larger than those produced by dipping because of the chemical composition, charge density, or some other underlying phenomenon. Under the deposition conditions used, the TiO<sub>2</sub> and DEX are moderately charged (based on  $\zeta$ -potential and considering their isoelectric points). Particle aggregation of TiO<sub>2</sub> is another possibility, which resulted in the large growth steps for dipping as observed in Figure 5.4. Moreover, the weak

interfacial attraction between the nanoparticle and polyelectrolyte moieties could also account for the large growth steps seen here. For a final comment, the nanoparticle and drug solutions were prepared in different pH solutions, and it is unknown what effect this may have had on the layer adsorption kinetics.

In the current available literature there exist some inconsistencies surrounding whether sprayed films are thicker than those produced by the conventional dipping method [150, 151]. In our previous works using nebulization we demonstrated that thicker films could be obtained when compared with the conventional substrate dipping method [85]. Izquierdo showed that sprayed and dipped films had the similar film thicknesses, where the only difference was the amount of time required to build the films. In this work it was also demonstrated that through use of longer spraying times, thicker films could be generated. It is the opinion of this author that films of varying thicknesses (equivalent to, thicker than or thinner than those achieved by dipping) can be produced depending on the spraying technique (aerosol vs. nebulization), film composition, and ionic strength of the solutions, among other possible factors. The mechanisms by which nanoparticles interact with the nebulization or aerosol machinery are likely very different than the way in which proteins or simple polyelectrolytes are expelled from the same.

#### **5.3.1.3 AFM measurements**

A Quesant Q-Force AFM operated in non-contact mode was used to assess the topography of the various films fabricated on glass slides. For each sample, a scan area of  $40 \times 40 \mu\text{m}^2$  was imaged. In some instances, smaller areas were desired. Typical images were obtained using a scan rate of 1-2 Hz. A histogram analysis was performed for each film architecture, to obtain values for roughness parameters. Several

measurements of island (particle) size were determined by dimensional analysis available through the AFM software. Other aspects of the physical film characteristics were noted. An AFM image of the nebulized film architecture  $(\text{PDDA/PSS})_3/(\text{TiO}_2/\text{DEX})/(\text{TiO}_2/\text{PSS})_3/\text{TiO}_2$ , is shown in Figure 5.5.

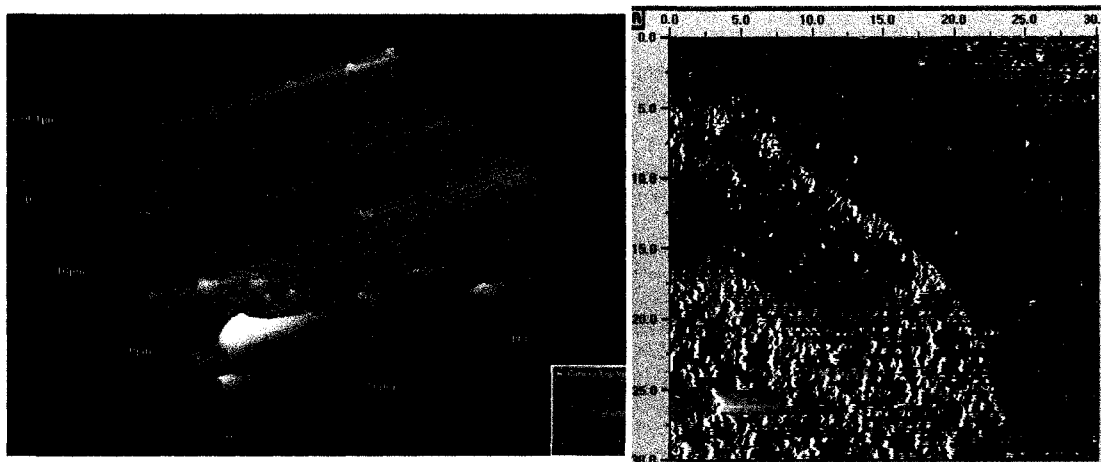


**Figure 5.5.** Non-contact AFM scan for nebulized architecture  $(\text{PDDA/PSS})_3/(\text{TiO}_2/\text{DEX})/(\text{TiO}_2/\text{PSS})_3/\text{TiO}_2$ . Scan area is  $30 \times 30 \mu\text{m}^2$ . (a) 3-D topographical representation (b) slope shading

As seen in this image, the film has a number of rounded surface features which are roughly similar in size. These clusters have an approximately uniform size of  $1 \mu\text{m}$  in the x and y directions while the height in the z-direction is around  $100 \text{ nm}$ . There is some particle aggregation, denoted by the large  $\sim 1 \mu\text{m}$  high feature. The underlying film surface is relatively smooth and even. The parallel striations on the surface (5.5 a) are an artifact from the AFM cantilever tip, and do not accurately reflect the film's surface topography. The film configuration  $(\text{PDDA/PSS})_3/(\text{TiO}_2/\text{PSS})_3/(\text{TiO}_2/\text{DEX})-\text{TiO}_2$  in which there is a superficial layer of DEX, terminated with a layer of  $\text{TiO}_2$  is shown below in Figure 5.6.

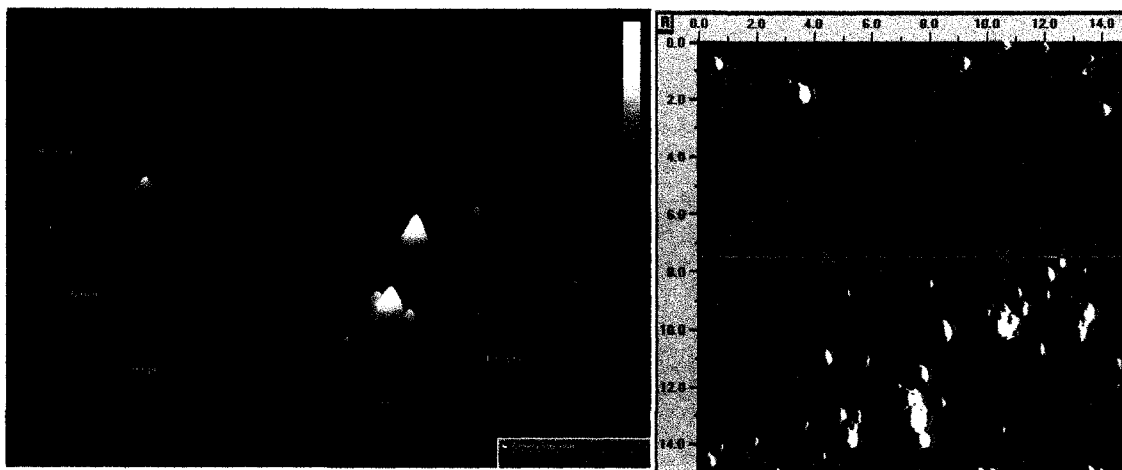


**Figure 5.6.** Non-contact AFM scan for nebulized architecture  $(\text{PDDA/PSS})_3/(\text{TiO}_2/\text{PSS})_3/(\text{TiO}_2/\text{DEX})/\text{TiO}_2$ ,  $15 \times 15 \mu\text{m}^2$  scan area (a) 3-D rendering, (b) slope shading

This film has a fairly homogeneous granular background (Figure 5.6 b), with some larger clusters and aggregates protruding from the surface. The average cluster size was 941 nm across, with some of the features exceeding 2  $\mu\text{m}$ . The cluster heights range from around 75-285 nm. Figure 5.7 represents a typical surface scan of film configuration  $(\text{PDDA/PSS})_3/(\text{TiO}_2/\text{DEX})/(\text{TiO}_2/\text{PSS})_3$ , where DEX is near the bottom of the film and the terminal layer is PSS.

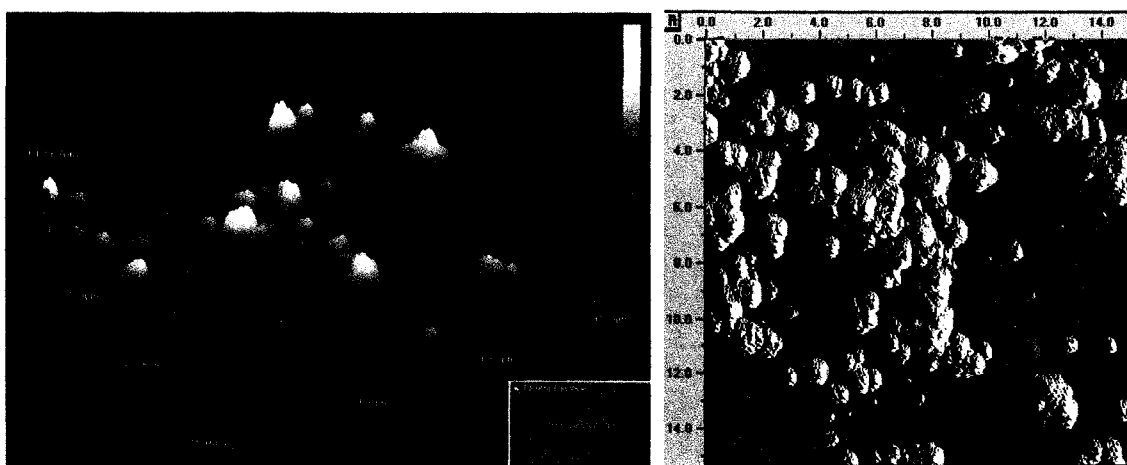


**Figure 5.7.** Non-contact AFM scan for nebulized architecture  $(\text{PDDA/PSS})_3/(\text{TiO}_2/\text{DEX})/(\text{TiO}_2/\text{PSS})_3$ ,  $15 \times 15 \mu\text{m}^2$  scan area (a) 3-D rendering, (b) slope shading.

The film's surface has several clusters within the substrate plane. The clusters are here have flattened plateaus, much different than the sharply pointed clusters seen in Figure 5.6. Also in there are concentric steps in the background of the film, probably due to pulsation of the nebulizer output. Figure 5.8 shows a typical AFM images for the film  $(\text{PDDA/PSS})_3/(\text{TiO}_2/\text{PSS})_3/(\text{TiO}_2/\text{DEX})$ , in which there is a terminal layer of DEX.

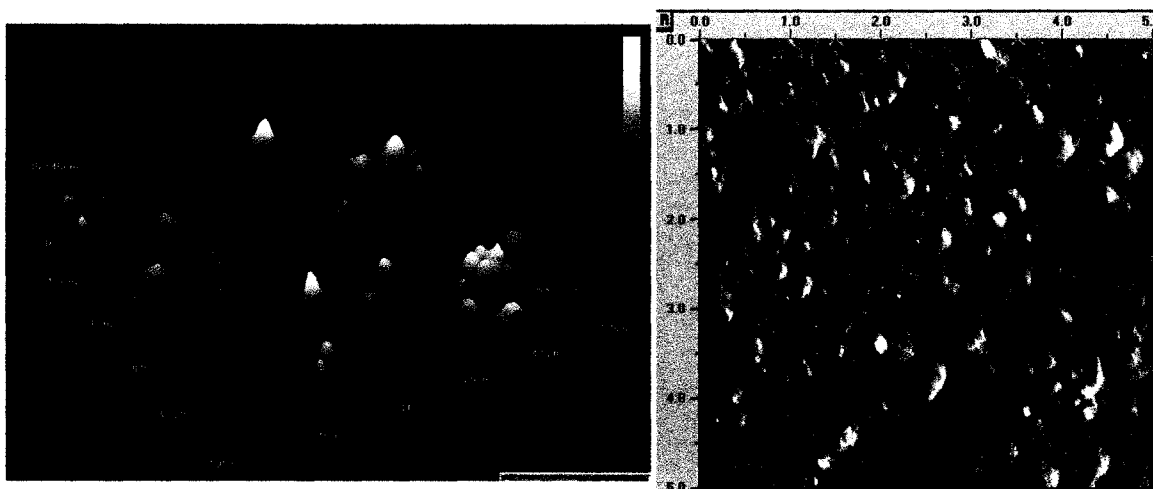


**Figure 5.8.** Non-contact AFM scan for nebulized architecture  $(\text{PDDA/PSS})_3/(\text{TiO}_2/\text{PSS})_3/(\text{TiO}_2/\text{DEX})$ .  $5 \times 5 \mu\text{m}^2$  scan area (a) 3-D rendering, (b) slope shading.

When compared with the other three films, this one has a much finer structure and very closely packed features. This surface also appears to be rougher than the others, but one must take into consideration that the scan area is much smaller than that of the other images.

Overall, the nebulized films have a certain degree of regularity, with the clusters within a specific film configuration assuming similar geometries. It is important to note, however, that the nebulization process can generate irregular film densities in areas not directly perpendicular to the output tubing. The morphology of a PSS-terminated film is different from that of a  $\text{TiO}_2$ - or DEX-terminated surface. This result is not surprising

since PEs such as PSS are typically more flexible when compared with more complex moieties such as drugs and inorganic nanoparticles. Generally, polyelectrolytes can arrange themselves into more stable films. Taking the AFM results together, addition of a terminal layer of TiO<sub>2</sub> appears to make the surface smoother, perhaps by covering the underlying grains. The PE layers are probably coating the previous TiO<sub>2</sub> NPs in such a way that the NP features are not distorted. It would be of interest to image the surface at each step during the film buildup process to confirm the inferences made here.

The size of clusters and surface domain features were obtained from surface section line profiles. Table 5.5 provides a summary of the data acquired from AFM measurements, including the average film height, feature sizes, and 3-D delta A, a software generated measure of surface roughness in the x-, y-, and z-directions.

**Table 5.5** Surface Parameters for Nebulized TiO<sub>2</sub> Films Obtained from AFM Measurements

SCHEME	Average thickness (nm)	Feature size (nm) n=3	3-D Delta A
DEX-D	63.872 ± 6.804	1044.00 ± 96.804	0.1073
DEX-SF	27.643 ± 5.065	707.66 ± 22.481	0.0338
DEX D-TiO <sub>2</sub>	301.94 ± 46.89	870.07 ± 33.559	0.6797
DEX SF-TiO <sub>2</sub>	68.312 ± 7.634	941.28 ± 59.833	0.1652

The films terminated with TiO<sub>2</sub> nanoparticles are thicker than their counterparts that are not terminated with TiO<sub>2</sub>. The cluster sizes generated from nebulization are between 0.7-1.0 μm in the substrate plane. These particle sizes are on the lower end of the reported values for a typical nebulizer output [113]. The 3-D delta A, which is a measure of film roughness is directly proportional to film thickness. That is, those films with the largest thickness also have the largest roughness in 3-dimensions. This result is

in agreement with other works, which have shown the trend of increased surface roughness with increasing layer thickness [90].

### **5.3.2 LbL Nebulized Thin Films Functionalized with TGF $\beta$ <sub>1</sub>**

Multilayered films were assembled on glass substrates in the manner described in section 5.2.2. Transforming growth factor-beta (TGF $\beta$ <sub>1</sub>) was incorporated as an active component in either deep (D), double layered (DL), or superficial (SF) 14-layer film architectures [92]. Table 5.6 provides a description of each scheme. The materials characterization and cellular response associated with these films are detailed in this section.

**Table 5.6** Nebulized Layer Architectures Functionalized with TGF $\beta$ <sub>1</sub>

SCHEME	ARCHITECTURE
D	(PDDA/PSS) <sub>3</sub> /(PDDA/TGF $\beta$ <sub>1</sub> )/(PDDA/PSS) <sub>3</sub>
DL	(PDDA/PSS) <sub>3</sub> /(PDDA/TGF $\beta$ <sub>1</sub> ) <sub>4</sub>
SF	(PDDA/PSS) <sub>6</sub> /(PDDA/TGF $\beta$ <sub>1</sub> )

#### **5.3.2.1 Zeta-potential measurements**

Each layer scheme was built up on anionic microspheres in the manner as previously described. Three precursory bilayers of PDDA/PSS were used to establish a foundation of uniform charge density for proper LbL fabrication of the layers of interest. As shown in Figure 5.9, the first six layer cycles for each scheme have nearly identical  $\zeta$ -potential values, where the PDDA layers are strongly positive, and the PSS layers are moderately negative.

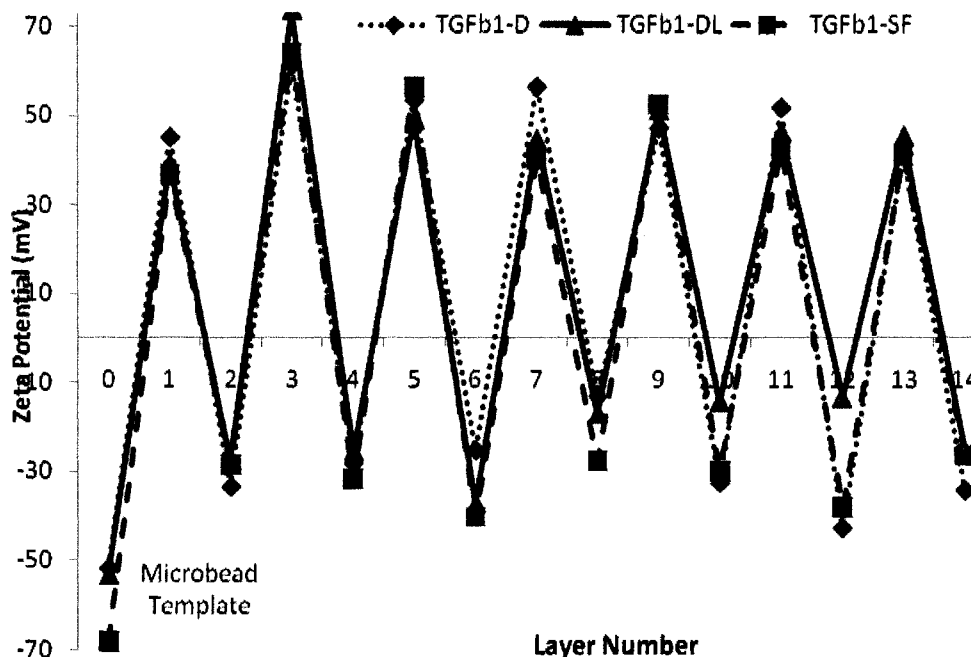


**Figure 5.9.** Zeta-potential alterations for nebulized films with TGF $\beta_1$ -embedded in deep, double-layered, and superficial modalities, pH 7, n=7.

The zigzag trend that occurs with each successive layer confirms that the layers are being assembled electrostatically. The  $\zeta$ -potential values for the TGF $\beta_1$  deposition steps are indicated in red, for clarification. In each instance, the steps for inclusion of the growth factor are weakly negative, having a  $\zeta$ -potential value of  $\sim 15$  mV. The layer steps involving PSS are also negatively charged, but more so than those which incorporate TGF $\beta_1$ . Throughout the LbL assembly, the PDDA deposition steps are very strongly charged, with  $\zeta$ -potentials between +50 and +60 mV.

Upon initial inspection, the negatively charged values for TGF $\beta_1$  are incongruent with the fact that its isoelectric point lies at pH 9. One would expect the protein to be positively charged at pH 7. However, in preparation of the TGF $\beta_1$ , the protein BSA was incorporated as a carrier molecule. It is likely that incorporation of negatively charged BSA (MW 66 kDa, isoelectric point pH 4.7) occupies many of the positively charged

ionizable groups in the protein (MW ~44 kDa), and even overcomes the protein's charge, due to the larger size. Moreover, several have commented on the capability to easily incorporate proteins within an LbL film, whether it is anionic or cationic [88, 89, 92]. Evidence supports the fact that proteins do not form their own intact layers but rather are solubilized by the adjacent layers [91].

### 5.3.2.2 QCM measurements

The QCM technique was employed to determine the thickness of TGF $\beta_1$ -embedded films, and measurements were performed as previously described. The results show a linear increase in thickness with each deposited layer pair (Figures 5.10-5.12).

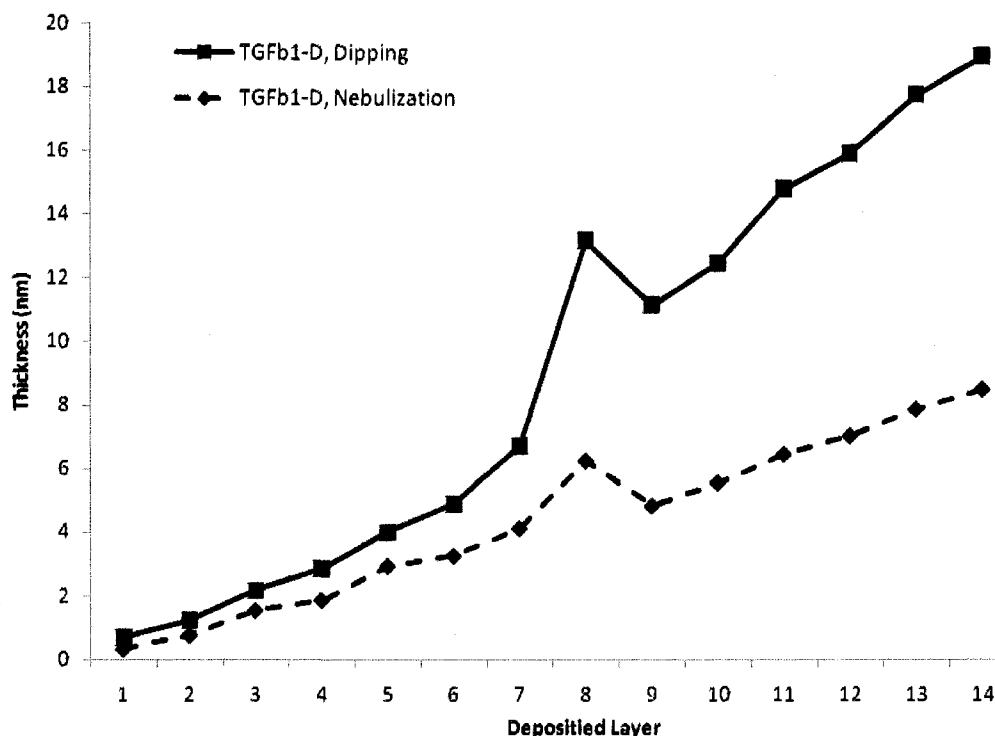


**Figure 5.10.** Progressive film thickness for TGF $\beta_1$  in the deep loading modality for assembly using (■) the substrate dipping method and (◆) nebulization, n=3.

For the scheme  $\text{TGF}\beta_1\text{-D}$ , consisting of  $(\text{PDDA}/\text{PSS})_3/(\text{PDDA}/\text{TGF}\beta_1)$   $(\text{PDDA}/\text{PSS})_3$ , the nebulization process produces a cumulative thickness of 8.49 nm while the conventional substrate dipping technique produces a cumulative thickness of 18.95 nm. The peaks shown at deposition step 8 correspond to the incorporation of  $\text{TGF}\beta_1$  within the film assembly.

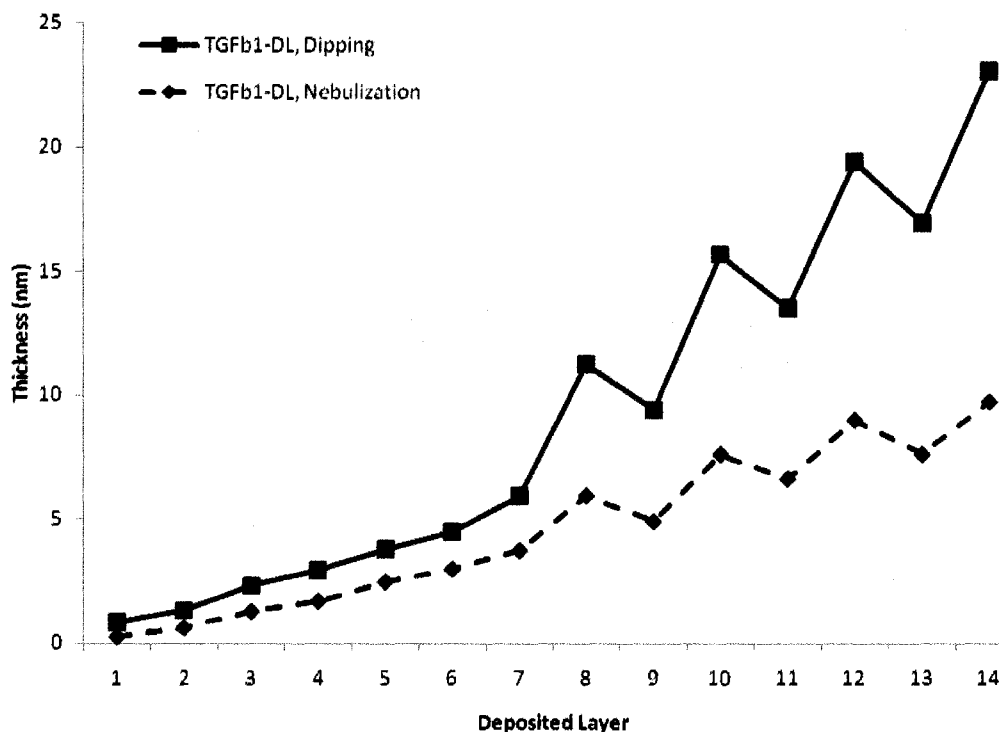


**Figure 5.11.** Progressive film thickness for  $\text{TGF}\beta_1$  in the double-layered loading modality for assembly using (■) the substrate dipping method and (◆) nebulization,  $n=3$ .

For the scheme in which  $\text{TGF}\beta_1$  is incorporated after each PDDA layer ( $\text{TGF}\beta_1\text{-DL}$ ), nebulization yields a cumulative layer thickness of 9.7077 nm. In this instance, the substrate dipping technique produces a total film thickness of 23.06 nm. Large growth steps of  $\sim 6$  nm occur when the growth factor is incorporated within the film, as shown here at deposition steps 8, 10, 12, and 14.

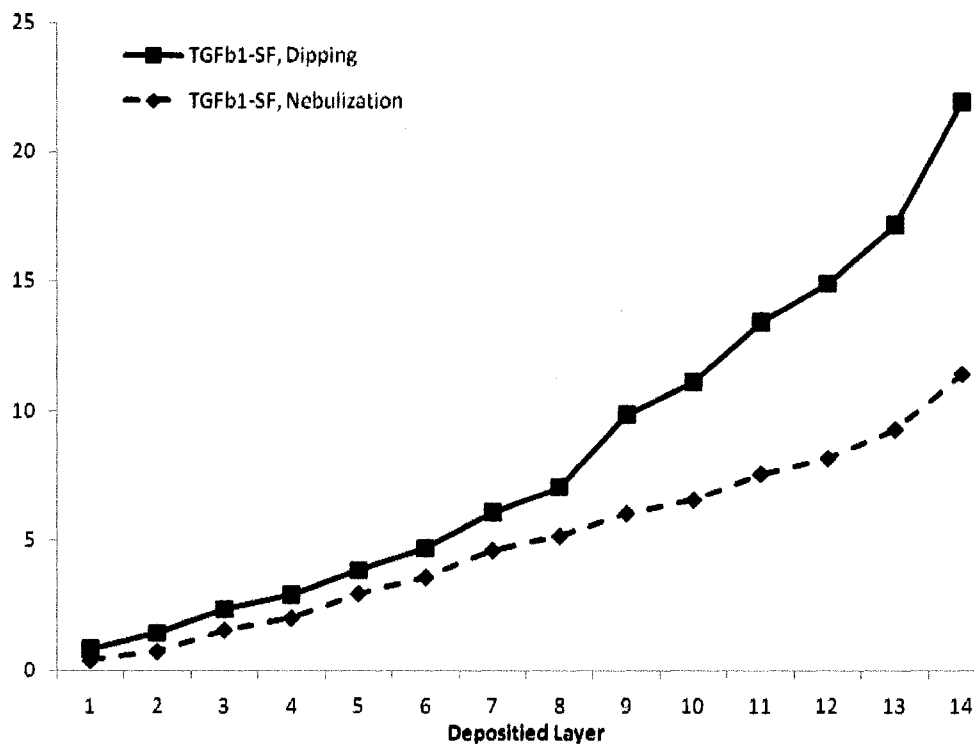


**Figure 5.12.** Progressive film thickness for TGFβ<sub>1</sub> in the double-layered loading modality for assembly using (■) the substrate dipping method and (◆) nebulization, n=3.

When TGFβ<sub>1</sub> was incorporated as a terminal film layer (TGFβ<sub>1</sub>-SF), the cumulative film thickness reached 11.42 nm. Layer 14 is step at which the growth factor is incorporated into the film. For both the substrates coated with TGFβ<sub>1</sub>-D and TGFβ<sub>1</sub>-DL loading modalities, deposition of the protein increases the film thickness and subsequent adsorption of PDDA leads to a decrease in film thickness. The total growth step for a bilayer of TGFβ<sub>1</sub>/PDDA fabricated by nebulization is ~1 nm while the substrate dipping process produces TGFβ<sub>1</sub>/PDDA bilayers which correspond to a growth step of ~4 nm. In each case, it is implied that some of the previously adsorbed protein layer becomes solubilized upon deposition of PDDA, however, there is enough charge exposed for electrostatic adsorption of a subsequent layer. The molecular conformation of the protein within the film structure is non-uniform and complex, as proteins can be larger

and less flexible than PE chains. This behavior in terms of QCM adsorption kinetics is commonplace for LbL deposition of proteins while polypeptides and polyelectrolytes are more uniformly charged allowing for preservation of a continuously increasing film structure [91].

The fabrication of 14-layered films by spraying process was achieved over a matter of minutes, a time frame in which only one layer could be deposited using the substrate dipping method. For instance, a 30 second substrate-PE contact time was required for deposition of the initial PE layer, followed by a 30 second rinse in DI H<sub>2</sub>O. Typically a time of 1-2 minutes was required between PE deposition steps to decant residual PE solution, rinse out the nebulizer chamber with DI H<sub>2</sub>O, and add the subsequent PE solution. Also during this time, additional evaporation and drainage could occur [151]. Thus, the deposition of one layer using the nebulization technique was accomplished in 3 minutes, giving a total fabrication time of about 42 minutes for a 14-layered film. With the traditional substrate dipping method, only about four layers can be built up within this same timeframe; LbL buildup in this fashion requires minimum contact times of 10-15 minutes, as well as 3-minute rinses in DI H<sub>2</sub>O. Therefore, it would take between 3-4 hours to fabricate a film consisting of 14 layers. Hence, LbL assembly by nebulization can scale up the fabrication process by at least 6-fold. Moreover, smaller spraying times of 1-10 seconds have been investigated by others, offering the possibility for fabrication of multilayer films even more expeditiously [150, 151].

There are still some unknown or uncontrollable parameters within the nebulization process, such as the power output and the density of droplets through the

nebulizer and the nebulizer tubing. Mist droplet size, for example, could not be directly controlled, but is notably an important factor to consider both for the coating process and the resultant effect on the cellular response. Residual solution in the nebulization chamber is a potential drawback of using the technique as a method of film-buildup. One way in which this issue was circumvented was to deposit layers on several substrates until the flow rate was affected. The maximum volume of the chamber was 5 mL, and it was discovered that to maintain a constant efflux of solution, a minimum volume of about 3 mL needed to remain in the chamber. In some cases the solutions could be reused for deposition of other layers. However, after deposition of TiO<sub>2</sub> nanoparticle layers, for example, the chamber had to be rinsed with copious amounts of isopropanol, followed by several additional rinses in DI H<sub>2</sub>O to prevent contamination of subsequent solutions.

### **5.3.2.3 Cell culture**

An identical set of TGFβ<sub>1</sub> nebulized substrates were prepared as previously described for cell culture experimentation. The coated substrates used were cut into 0.25 cm<sup>2</sup> pieces, sonicated in 70% isopropyl alcohol for 15 minutes, and placed into the wells of a 24-well culture dish. Immediately before cell seeding, the substrates were UV-irradiated for 30 minutes and rinsed thrice in Hank's Balanced Salt Solution (HBSS). Human Dermal Fibroblasts (HDFs) were then seeded onto the substrates at a density of 5000 cells/cm<sup>2</sup> and allowed to adhere overnight. Cells were then cultured in 1 mL of Dulbecco's Modified Eagle's Medium (Cellgro), supplemented with 10% fetal calf serum (Hyclone), and 1% penicillin/streptomycin (Mediatech). The cultures were maintained in 95% humidified air, 5% CO<sub>2</sub> environment at 37°C.

To investigate the influence of nebulized films on the growth and function of HDFs, cells were seeded on uncoated glass substrates and used as a negative control. Three experimental cell culture groups were established based on layer composition and architecture. The cells grown on substrates coated with architectures of TGF $\beta$ <sub>1</sub>-DL, TGF $\beta$ <sub>1</sub>-SF, and TGF $\beta$ <sub>1</sub>-D were cultured in completed DMEM. Furthermore, as a positive control, cells seeded on uncoated glass were grown in DMEM containing 10ng/mL TGF $\beta$ <sub>1</sub> (termed TGF $\beta$ <sub>1</sub>-M). Cell culture medium (with or without growth factor supplements) was replenished every two days in a volume of 1 mL. Each experimental group was maintained and analyzed for a period of 21 days.

Cells cultured on the nebulized nanosubstrates were characterized for mitochondrial activity, double-stranded DNA, and the presence of the ECM protein, type-I collagen.

#### **5.3.2.3.1 Cell viability**

Live/Dead viability of HDFs was analyzed at 4, 7, 14, and 21 days post-seeding. A Live/Dead working solution (Invitrogen) was prepared by diluting 20  $\mu$ L of ethidium homodimer-1 (EthD-1) and 5  $\mu$ L of calcein acetoxymethyl (Calcein AM) in 10 mL of HBSS without phenol red. After rinsing substrates thrice in HBSS without phenol red, samples were incubated in 100  $\mu$ L of Live/Dead solution for 30 minutes.

Samples were viewed on an Olympus IX51 microscope in brightfield, FITC, and TRITC modes. Use of the FITC filter (excitation 485 nm) allowed for detection of live cells, which convert the cell permeant, non-fluorescent calcein AM to the fluorescent product, calcein. In the TRITC mode (excitation 540 nm), dead cells fluoresce due to EthD-1 traversing damaged membranes. Images were acquired with a monochrome

camera (type) and saved as tag image file format (TIFF) files. 8-bit grayscale images were colorized and merged to show dual fluorescence using Adobe Photoshop. Figure 5.13 shows the Live/Dead images for HDFs at 14 days post-treatment for each of the experimental groups.

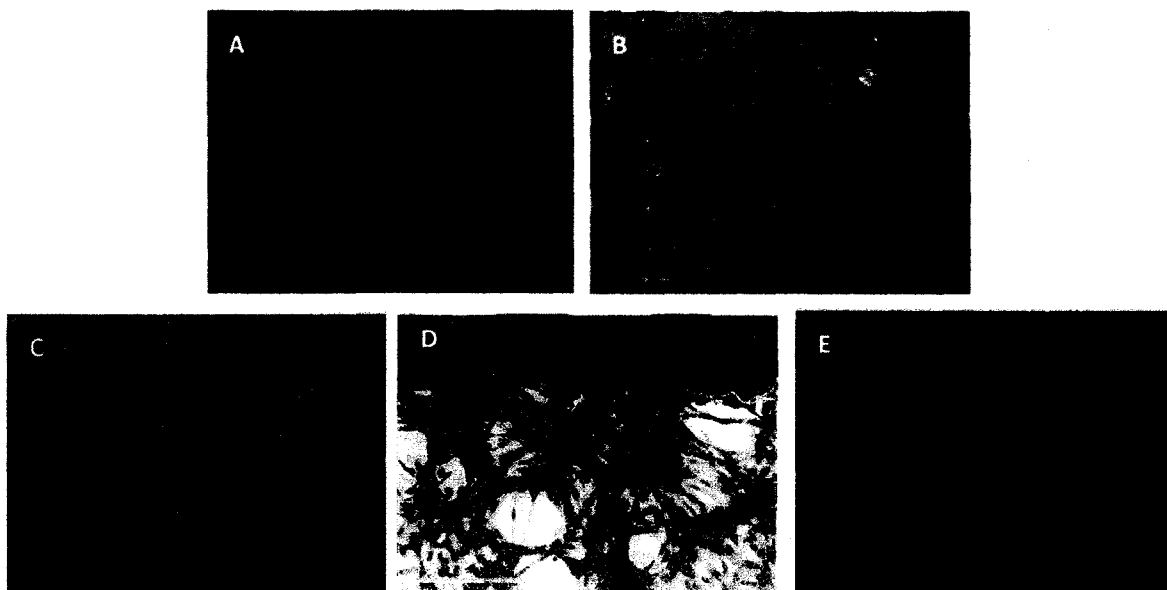


**Figure 5.13.** Live/Dead for TGF $\beta_1$  (A) control, (B) TGF $\beta_1$  in media, (C) TGF $\beta_1$ -deep, (D) TGF $\beta_1$ -double layered, (E) TGF $\beta_1$ -superficial. A and C scale bar=50  $\mu\text{m}$ , B, D, E scale bar=100  $\mu\text{m}$ .

The figures here are representative of cytotoxic response to HDF culture in the presence of TGF $\beta_1$ -embedded nebulized films. Overall, it can be seen that there are show that there are few dead cells (red fluorescence) in comparison to the live cells (green fluorescence) which are apparent within images of the various experimental groups.

#### **5.3.2.3.2 Mitochondrial activity**

Cellular viability was measured through the MTT Assay. MTT is a reduced to a purple formazan product in mitochondrially active cells (Appendix E). A stock solution of (3-(4,5-dimethylthiazol-2-yl)-2,5-diphenyltetrazolium bromide (MTT) was prepared at 5 mg/mL in PBS. The stock solution was further diluted in completed DMEM in a 1:10

ratio. The 10% working solution was freshly prepared before each use. For each sampling point (4, 7, 14, 21 days) cell culture media was decanted and the glass substrates for each treatment were rinsed thrice in HBSS without phenol red. A volume of 100  $\mu\text{L}$  of MTT working solution was added to the samples and the cells were incubated for a period of 24 hours at 37C. After the incubation time, the purple formazan precipitate was dissolved with 100  $\mu\text{L}$  of 70% isopropyl alcohol. The solutions were then transferred to 96-well plates and absorbance was immediately measured at 570 nm using a reference wavelength of 690 nm (Tecan Sunrise Spectrophotometer). An average of three measurements for each sample was obtained. The results appear in Figure 5.14.

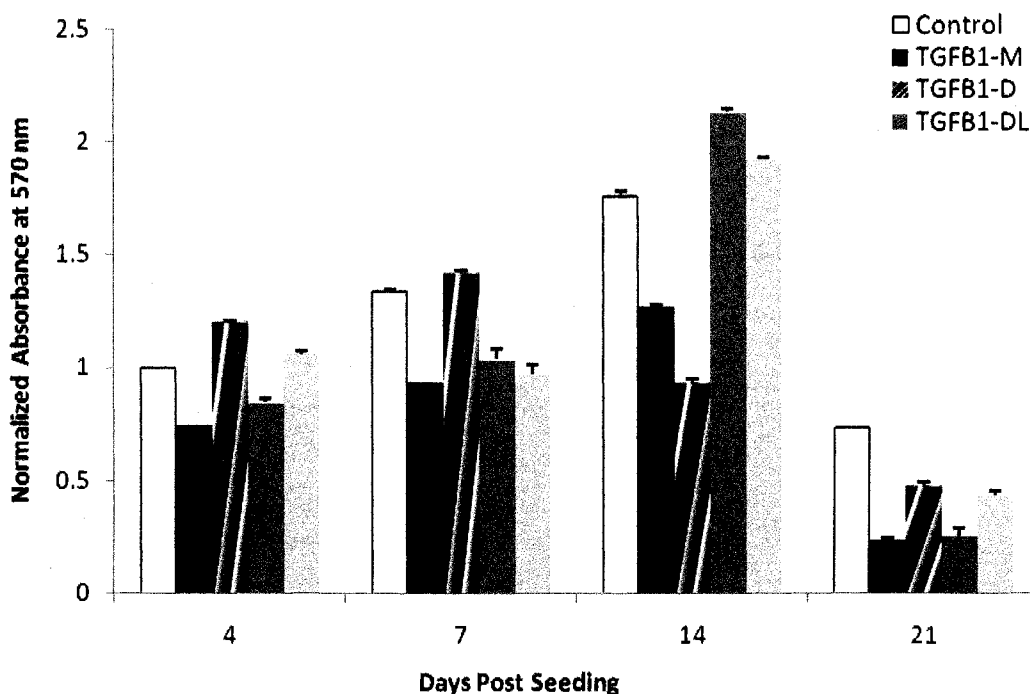


**Figure 5.14.** MTT results for TGF $\beta_1$ -embedded films produced by nebulization in deep (D), double-layer (DL), and superficial (SF) configurations. Results are compared with positive and negative controls and normalized to Day 4 controls, error bars equal 1 SD, n=3.

The maximum metabolic activity measured over each experimental group occurred at 7 days for the TGF $\beta_1$ -D, and 14 days for both the D and DL preparations. For each measured time period, the positive control with the growth factor incorporated in the cell culture medium (termed TGF $\beta_1$ -M) resulted in the smallest metabolic activity levels. This could be an indication that the cells are not receiving as much of a stimulus as that which is provided by other loading modalities. At day 14, the cells grown on TGF $\beta_1$ -DL slides are more metabolically active than the controls, suggesting that some overproliferation was induced. Indeed, it is known that a very small amount of the growth factor was available for cellular action when simply added to the media. Conversely, in the DL loading preparation, it is conceivable that the highest amount of TGF $\beta_1$  was available to induce cellular response. The SF preparation most likely showed some high metabolic activity initially, however, there is no data presented here for Day 1, which would support this claim. It is possible that for cells cultured on substrates with TGF $\beta_1$  in the D configuration, a significant effect on mitochondrial activity would be seen later than 21 days, due to the position of the growth factor.

#### **5.3.2.3.3 DNA quantification**

The amount of double-stranded DNA was quantified to investigate the influence of TGF $\beta_1$  loading modality (M, D, DL, SF) on cellular function. For each sampling period (1, 4, 7, 14, 21 days), cell lysate was recovered and stored at -80°C until needed for analysis. For a detailed protocol, see Appendix F. Quant-iT™ PicoGreen® dsDNA reagent (Invitrogen) was used to quantify the amount of DNA present in the samples' cell lysate. The PicoGreen reagent was diluted 1:200 in 1X TE buffer and protected from light. In a black 96-well plate, 10  $\mu$ L of cell lysate was diluted in 90  $\mu$ L TE buffer. The

PicoGreen working solution was then added to each sample in a volume of 100  $\mu\text{L}$ . The plates were incubated for 5 minutes in the dark. An excitation wavelength of 485 nm was used, and fluorescence intensity was read at an emission wavelength of 538 nm (Tecan Genios Platerader). Results obtained from these measurements over the 21-day period are shown in Figure 5.15.

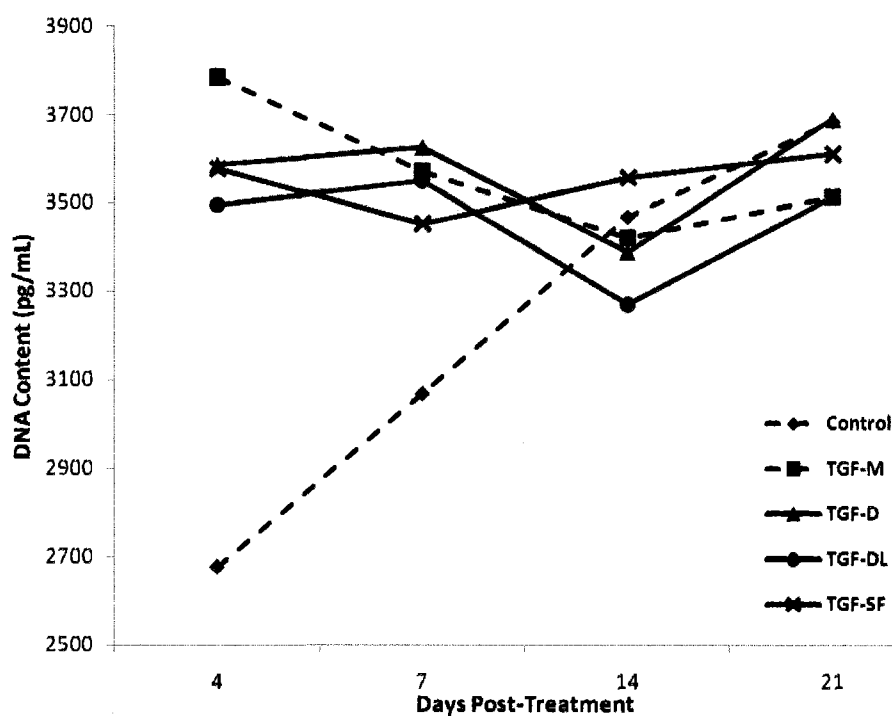


**Figure 5.15.** DNA quantification for cell culture on TGF $\beta_1$  nebulized substrates. Fluorescence intensity at 538 nm is background corrected to TE buffer, n=3.

The HDFs which received no TGF $\beta_1$  supplementation showed a steady increase in DNA content over the testing period. The positive control group, termed TGF $\beta_1$  had the highest DNA content at 4 days post-treatment. The DNA content for this group decreased until 14 days post-treatment, after which time it remained nearly stable. For cells cultured on TGF $\beta_1$ -loaded films, the DNA content fluctuated between 3200 and 3700 pg/mL throughout the experimental period.

#### **5.3.2.3.4 Cell morphology and localization of BrdU and collagen I**

To determine the degree to which mitotically active cells expressed proteins representative of a fibroblast phenotype, 5-Bromo-2'-Deoxyuridine (BrdU) and endogenous type-I collagen were co-localized in cells cultured on control and experimental substrates at 1, 4, 7, 14, and 21 days. BrdU is a mutagen that replaces thymine in DNA during cellular replication. A 5 mg/mL stock solution of BrdU (Sigma) was prepared in HBSS without phenol red and syringe-filtered. A working solution of BrdU in completed DMEM in a 1:100 dilution was prepared fresh for each use. On the sample day, existing media was decanted from substrates, and replaced with 1 mL of BrdU/DMEM. The samples were incubated for 24 hours at 37°C. Following the incubation period, substrates were rinsed in HBSS and cells were fixed in 95% ethanol at room temperature for 20 minutes. Cell substrates were preserved in PBS until further use. A double immunofluorescence labeling technique was used for visualization of collagen-I and BrdU immunoreactivity within the same sample (Appendix G).

Figure 5.16 shows the differences in HDF morphology for each experimental group, using differential interference microscopy. The images were acquired using a 40X objective.

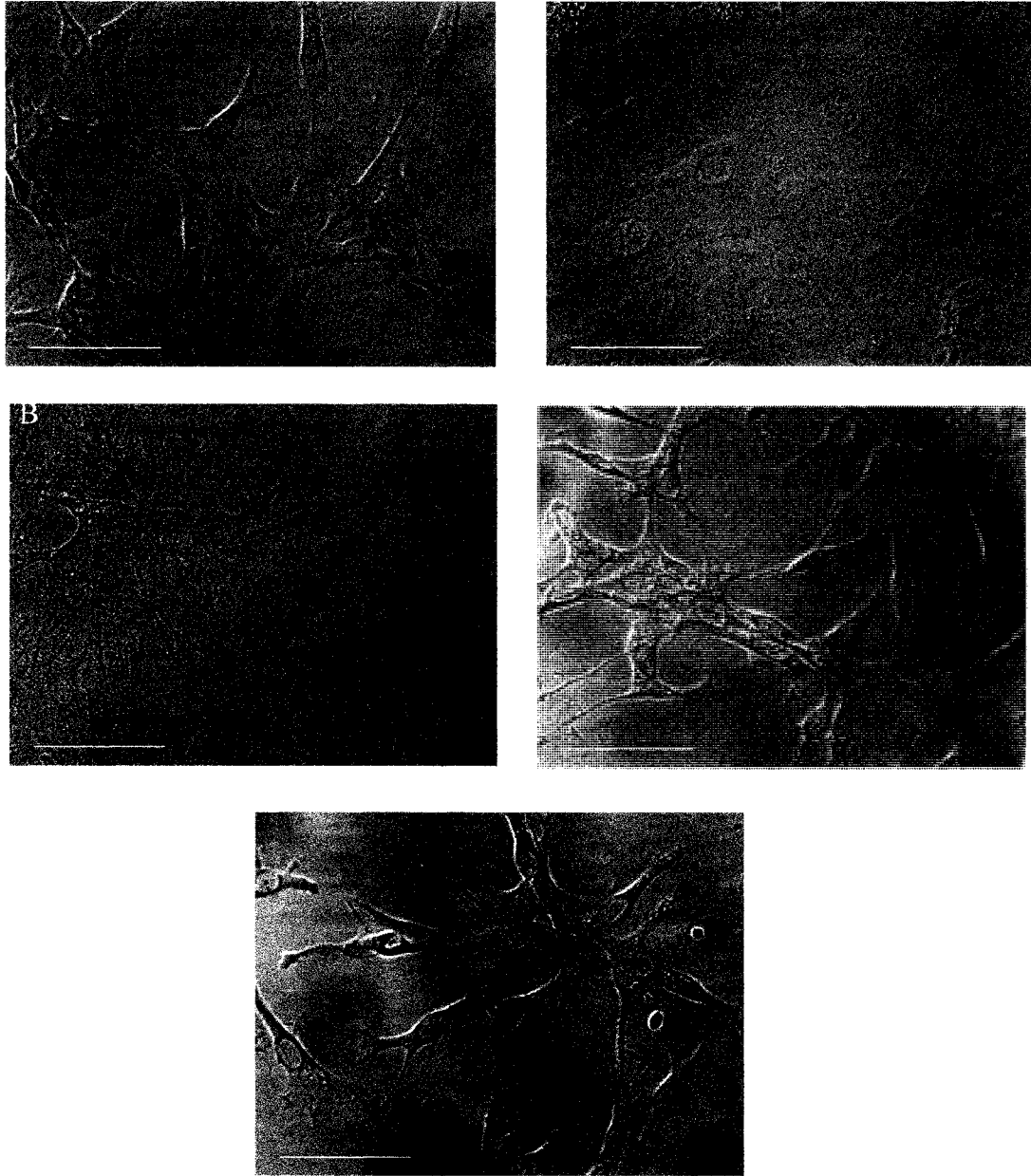


**Figure 5.16.** DIC images of fixed HDFs cultured on substrates with loading modalities (A) control and (B) culture with TGFβ<sub>1</sub> supplemented in the cell culture media. (C) TGFβ<sub>1</sub>-deep, (D) TGFβ<sub>1</sub>-double layer and (E) TGFβ<sub>1</sub>-superficial. The scale bar represents 25 μm.

From Figure 5.16, it can be observed that at 14 days, the cells cultured in the presence of TGFβ<sub>1</sub>-supplemented media have larger nuclei and cell bodies than any of the other experimental groups. In Figure 5.16 A, and to a larger extent in Figure 5.16 D

and F, the HDFs have very distinct cellular processes that appear to be anchoring them to the substrates. Interestingly, each of these substrate preparations consists of a terminal layer of TGF $\beta$ <sub>1</sub> with BSA as a carrier molecule.

BrdU analysis of HDFs cultured under each of the experimental conditions is shown in Figure 5.17. A positive reaction, indicated by the high intensity red staining, was obtained in all cases.

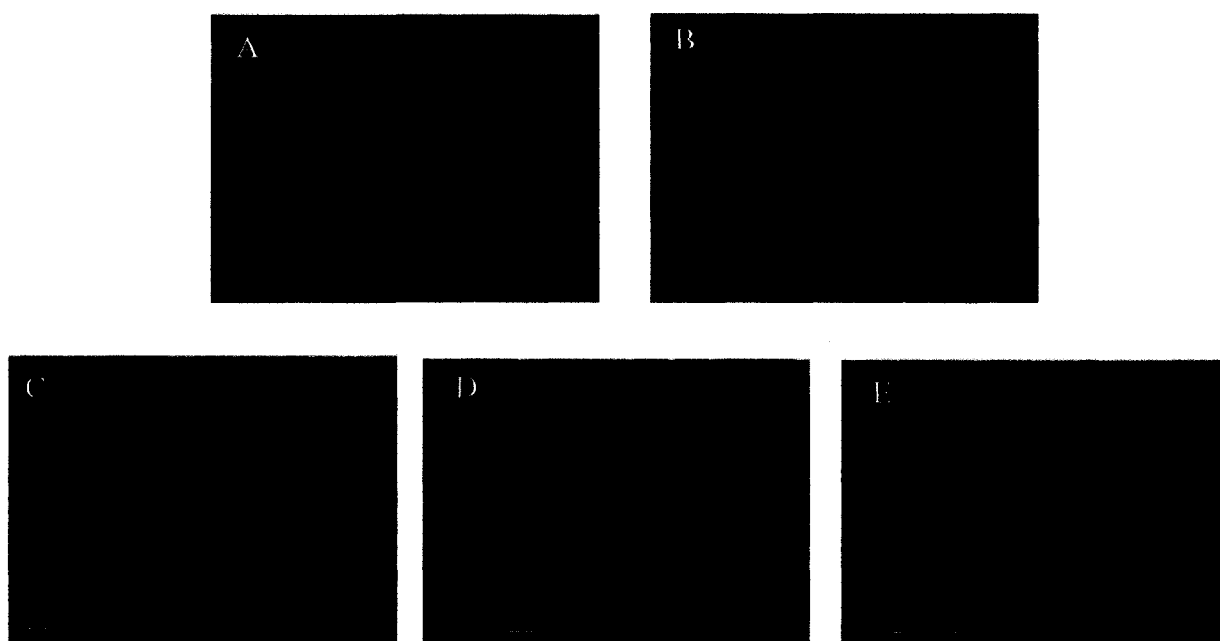


**Figure 5.17.** BrdU localization for HDFs cultured on substrates with loading modalities (A) control and (B) culture with TGF $\beta$ <sub>1</sub> supplemented in the cell culture media. (C) TGF $\beta$ <sub>1</sub>-deep, (D) TGF $\beta$ <sub>1</sub>-double layer and (E) TGF $\beta$ <sub>1</sub>-superficial. The scale bar represents 25  $\mu$ m.

Again, it can be noted that the cells cultured in TGF $\beta$ <sub>1</sub>-supplemented media are larger and have a different morphology when compared with those from any of the other preparations. These cells (Figure 5.18 B) are wider, larger, and not spindle-shaped as is the case for the other growth conditions. A representative image of collagen I immunocytochemical detection is presented in Figure 5.18.



**Figure 5.18.** Fluorescent image of collagen I immunoreactivity in HDFs cultured on TGF $\beta$ <sub>1</sub>-SF substrates at 21 days post-treatment. The scale bar represents 25  $\mu$ m.

There is very intense immunoreactivity for collagen I in this instance, as there is a great deal of contrast between the background and the regions of interest. However, other samples, such as those for cells cultured on TGF $\beta$ <sub>1</sub>-D substrates, appeared to show no immunoreactivity at first glance. It was later determined that a fluorescence signal was present; however, it could not be obtained under the default exposure-time setting. In attempts to connect a quantitative value with the collagen I signal, the minimum exposure required to obtain a fluorescence signal was recorded for the 21 days post-treatment samples. In this way, it is assumed that the background fluorescence across all preparations was the same. The minimum exposure times for signal acquisition at 40X magnification for each of the preparations is provided in Table 5.7.

**Table 5.7** Minimum Exposure Times for Collagen I Fluorescence Signal Acquisition

<b>EXPERIMENTAL GROUP</b> <i>Day 21</i>	<b>MINIMUM EXPOSURE TIME (ms)</b> <i>Collagen I signal</i>	<b>FLUORESCENCE INTENSITY</b>
Control (no additive)	9.1	6902.249
TGF $\beta_1$ -M	66.1	3110.734
TGF $\beta_1$ -D	14.6	5492.821
TGF $\beta_1$ -DL	3.6	7553.568
TGF $\beta_1$ -SF	11.7	6269.819

Comparison of the minimum exposure times and intensities for fluorescence in each experimental group allows for a relative comparison on collagen I immunoreactivity, where the largest fluorescence signal corresponds with the smallest exposure time. The group with the smallest minimum exposure time and largest fluorescence intensity, was the TGF $\beta_1$ -DL group, indicating that cells in this group were producing the largest immunoreactivity to collagen I. Likewise, the group with the highest minimum exposure time (66.1 ms) was the TGF $\beta_1$ -M group, having the weakest immunoreactivity to collagen I. The exposure times for acquisition of BrdU at 40X magnification ranged between 1000 and 2500 ms, indicating that these signals were much weaker and more difficult to detect than those of collagen I.

#### **5.4 Conclusions**

LbL film fabrication was successfully elaborated over planar glass substrates using an ultrasonic nebulizer. Aside from traditionally used PEs, colloidal TiO<sub>2</sub> nanoparticles, the drug DEX and the growth-factor TGF $\beta_1$  were easily incorporated within the film structure during this process. Much of the work presented here was an initial attempt to characterize the nebulized films, in terms of interfacial chemistry, as this has yet to be reported. Furthermore, preliminary *in vitro* testing of the growth factor-

loaded substrates was performed using human dermal fibroblasts (HDFs). Specifically, the effect of TGF $\beta_1$  nebulized coatings were evaluated in terms of adhesion, DNA content, mitochondrial activity, and collagen I production of HDFs over a three-week period. Cellular processes indicative of greater substrate adhesion were noted on TGF $\beta_1$  functionalized substrates which incorporated the protein in a superficial layer, when compared with both HDFs cultured on glass slides and HDFs cultured on glass slides in media supplemented with TGF $\beta_1$ . Assessment of mitochondrial activity indicated a maximum proliferation at 7 days for TGF $\beta_1$  in the D configuration, and at 14 days for the DL and SF loading schemes. Each loading scheme resulted in a higher DNA content compared with the control over 7 days. HDFs cultured on substrates with TGF $\beta_1$  in the D configuration demonstrated the highest DNA content over the 21-day period. Incorporation of TGF $\beta_1$  in the DL configuration led to the highest collagen I immunoreactivity after 21 days of treatment. These results were not correlated to a specific release of TGF $\beta_1$  over time, which surely has an effect on the cell response. In theory, the amount of TGF $\beta_1$  incorporated into the multilayer architectures is on the order of mg/cm<sup>2</sup>/day, when compared with only a few ng/cm<sup>2</sup>/day for the positive control. Release studies should be conducted to determine the dissolution of TGF $\beta_1$  from the multilayered assemblies to further support the data obtained from cell culture characterization.

HDFs culture on substrates containing TGF $\beta_1$  in a superficial position demonstrated heightened mitochondrial activity and the presence of distinct cellular processes at 14 days, which could be indicative of enhanced cell adhesion. Furthermore, differences in loading modalities of the growth factor may lead to

alterations in cellular differentiation processes, as evidenced by assessment of collagen I immunoreactivity. The ability to influence cell phenotype is certainly a promising outcome of this technology. A more detailed analysis of cell-substrate interactions is warranted, as there are still many unknowns, such as how the deposition times, distances, and film composition affect film composition, rigidity, and cellular responses with varied cell types. The results strongly indicate that the nebulization technique produces quality, organized film architectures while having an addition benefit of expediting film fabrication. Certainly, these two properties can be extremely advantageous in the coating of implants or other biomaterials, but the cost fabricating growth factor and drug embedded films must be considered in the context of scale-up. Nonetheless, it is envisioned that the inclusion of this and other growth factors or other bioactive agents could be used for enhancement of dental and orthopedic implants, or in the form of a bioactive bandage for support and enhancement of the initial stages of cutaneous wound healing.

## **CHAPTER 6**

### **CELLULAR ENCAPSULATION WITHIN NANOTHIN CAPSULES USING LAYER-BY-LAYER ASSEMBLY**

#### **6.1 Introduction**

Cellular encapsulation within polymer complexes has recently been an intense area of study, particularly as method for creation of an artificial pancreas in which Islet of Langerhans cells can be encapsulated in an alginate hydrogel [154, 155]. Within the encapsulation matrix, these cells are still capable of retaining their function, producing and exporting insulin. Awareness of the ability to retain islet function within permeable shells and matrices has prompted others to investigate the encapsulation of other cell types, including fibroblasts, chondrocytes, hepatocytes, and mesenchymal stem cells (MSCs) [52, 156-159].

Precise control of the microenvironment provides a means through which MSCs can give rise to a number of cell types, including chondrocytes, adipocytes, osteoblasts, neurons, and others [40]. It is their vast differentiation capability coupled with an innate self-renewal property that offers the possibility for treatment of numerous disease states and clinical issues. Whether the cells achieve and maintain a desired phenotype depends upon on a diverse set of extracellular environmental cues designed to direct and regulate cell behavior. The bone morphogenic proteins (BMPs) and members of the

transforming growth factor (TGF) superfamily are among the most studied signaling molecules, which have been identified as playing an important role in initiating pathways that lead to the differentiation and preservation of various cell types [123].

MSC differentiation *in situ*, however, poses a great challenge. Many substances used to enhance cellular function *in vitro* are not necessarily successful *in vivo*. For instance, monolayer culture of MSCs in the presence of osteogenic supplements such as dexamethasone, ascorbic acid-2 phosphate, and  $\beta$ -glycerol phosphate results in osteoblast lineage commitment and matrix mineralization, but has been shown to suppress *in vivo* bone growth in certain instances [159]. Therefore, in an *in vitro* setting, the simple addition of these molecules while providing instructional cues into the cellular environment, is unregulated, and has been shown to be insufficient in producing the desired extracellular matrix (ECM) architecture required in tissue-engineered implants due to their short half lives [160-162]. A means to regulate delivery of a suite of signaling molecules, ideally in a multi-stage framework of release, both spatially and temporally, is highly desired. Thus, it follows that bioencapsulation as first suggested by Chang in 1964, is a promising method to orchestrate the appropriate interaction between cells, instructional molecules, and the microenvironment leading to desired tissue-engineered constructs [163]. Furthermore, encapsulation of MSCs allows for creation of an *in vitro* 3-D microenvironment, and for the concerting of soluble signals both temporally and spatially, thereby better approximating MSC behavior to that witnessed in a native milieu.

The overarching goal of this project was to individually encapsulate cells within nanothin layers consisting of biocompatible polyelectrolytes and growth factors. To

accomplish this goal the layer-by-layer assembly (LbL) technique was chosen because of the mild assembly conditions, nanoscale precision, tuneability, and the potential for surface modification. Through this process, the negatively charged cell membrane can be encased within a cationic polymeric shell; oppositely charged polymers can be subsequently adsorbed to achieve a desired thickness and surface composition. The polyelectrolyte multilayers can be tuned to generate thicknesses from 5 to 50 nm, and alter capsule permeability based on composition and layer number [73, 152, 164]. It has been shown that poly(styrene sulfonate) (PSS)/ poly(allyamine) (PAH) layers on echinocytes were useful in generating nanotemplated cell capsules [78]. Moreover, a study by Diaspro et al. reported that prokaryotic cells encased within PSS/PAH polyelectrolyte shells were able to maintain their viability, functionality, and normal exchange of nutrients and waste [165]. LbL assembly has been used to modify platelet surfaces with antibodies as a means of investigating targeted delivery mechanisms within the walls of blood vessel substitutes [166] and for encapsulation of *E.coli* cells [167]. Alternatively, appropriate selection of polymers can also be exploited for the fabrication of stealth cellular vehicles. The masking of cells in this fashion could make them immunologically invisible, a desirable property in the case of allogenic transplants.

In this study we demonstrate the ability to individually encapsulate mouse mesenchymal stem cells (MSCs) and human dermal fibroblasts (HDFs) within multicomponent shells consisting of various materials suitable for LbL assembly, including polyelectrolytes, drugs, and proteins. The sections that follow include materials characterization and acute cell viability studies for MSCs and HDFs encapsulated within different capsular matrices.

## **6.2 Materials and Methods**

### **6.2.1 Preparation of Polyelectrolyte, Nanoparticle, Protein, and Drug Solutions**

Materials suitable for LbL assembly were used, including synthetic and natural PEs, charged colloidal nanoparticles, and water-soluble protein growth factors. The PEs hyaluronic acid (HA), poly(L-lysine), (PLL, MW 30,000), poly(styrene sulfonate) sodium salt, 30% (PSS), poly(dimethylallyl ammonium chloride), 20% (PDAA, MW 400,000), chondroitin-6 sulfate (CS, MW 60,000), poly(L-aspartic acid sodium salt, MW 15,000 – 50,000) (PLAA protamine sulfate (PS, MW 70,000) were obtained from Sigma Aldrich. All PEs were prepared between 1-3 mg/mL in DI H<sub>2</sub>O, HBSS, or 0.5 M NaCl when indicated. Titanium Dioxide (P25 Degussa AG, Germany) diameter ~21 nm, was prepared in DI H<sub>2</sub>O at a concentration of 6 mg/mL and adjusted to pH 4 with dilute HCl. Growth factors were prepared according to the supplier's recommendations. Briefly, rHBMP<sub>2</sub> (ProSpec, Israel) was reconstituted in 20 mM of sterile glacial acetic acid, and further diluted in Phosphate Buffered Saline (PBS) to give a stock concentration of 100 µg/mL. 1 µg of TGFβ<sub>1</sub> (ProSpec, Israel) was reconstituted in 4 mM HCl containing 1 mg/mL of Bovine Serum Albumin (Sigma) to yield a stock solution of 1 µg/mL. The growth factor stock solutions were then diluted with either cell culture medium or buffer, as appropriate for experimental use, to give a final concentration of 10ng/mL. Table 6.1 details the molecules used and their associated isoelectric points.

**Table 6.1** Isoelectric Points of Polyelectrolytes, Nanoparticles, and Biomolecules

<b>MOLECULE</b>	<b>ABBREVIATION</b>	<b>PI</b>
Bone Morphogenic Protein-2	BMP <sub>2</sub>	9
Chondroitin Sulfate	CS	3.2
Hyaluronic Acid	HA	2
Poly(L-aspartic acid)	PLAA	2.8
Poly(styrene sulfonate)	PSS	2
Poly(dimethylallyl ammonium chloride)	PDDA	12
Poly(L-lysine)	PLL	9
Protamine Sulfate	PS	10-12
Titanium Dioxide	TiO <sub>2</sub>	5
Transforming Growth Factor Beta-1	TGFβ <sub>1</sub>	8.9

### **6.2.2 Fabrication of Cellular Capsules**

Mouse MSCs (ATCC-CRL 12424) were cultured in completed Alpha-Modified Eagle's Medium (10% fetal bovine serum, 1% penicillin/streptomycin, 2mM L-glutamine). HDFs were cultured in Dulbecco's Modified Eagle's Medium (Cellgro), supplemented with 10% fetal calf serum (Hyclone), and 1% penicillin/streptomycin (Mediatech). Cells were incubated at 37 °C in a 5% CO<sub>2</sub>, 95% humidified air environment.

A cationic solution was added to the cell suspension for deposition of the first layer. After layer adsorption had been achieved, three intermediate washings with HBSS were made at 37 C using centrifugation at 1000 rpm for 5 minutes. Subsequently, the counterionic layer was adsorbed in the same manner. This process was repeated until the desired layering scheme was achieved. Figure 6.1 provides an illustration of thin film deposition onto a cellular template using the LbL technique.

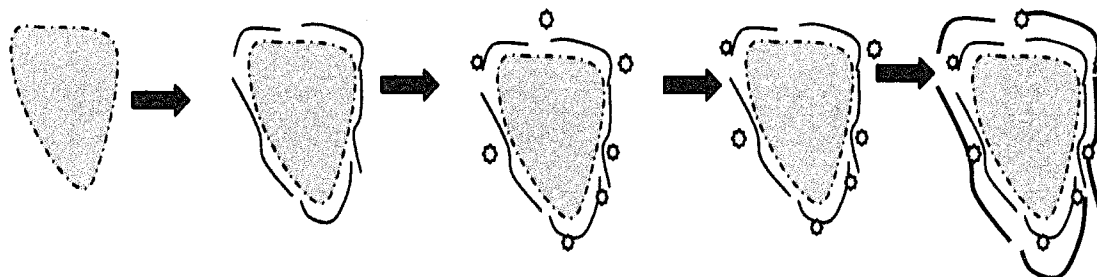


**Figure 6.1.** Illustration of cell encapsulation process, in which the negatively charged cell can be coated with polyelectrolytes (gray and red lines), as well as nanoparticles, or biologically relevant molecules (small circles)

## **6.3 Results and Discussion**

### **6.3.1 MSC Encapsulation in Biocompatible Shells**

Bilayers of PLL/HA or PLL/BMP<sub>2</sub> were deposited onto MSC templates as described in Section 6.2.2., so that a layering scheme of MSC/(cationic solution/anionic solution)<sub>n</sub> was attained, where n=1-3. PLL and HA were used at 1 mg/mL. A deposition time of ten minutes was typically used for PEs and BMP<sub>2</sub> was allowed to adsorb for 30 minutes. PLL and HA solutions (1 mg/mL) were prepared in each of the following solvents: DI H<sub>2</sub>O, Hank's Balanced Salt Solution (HBSS), and 0.5 M NaCl. Cationic PLL was first added to a 5x10<sup>6</sup> cells/mL suspension of mouse MSCs. After the washings in HBSS, the anionic HA or 10 ng/mL BMP<sub>2</sub> was adsorbed. In the instance where PLL/BMP<sub>2</sub> films were formed on the MSCs, PLL was added to a cell suspension of 2x10<sup>6</sup> cells/mL.

#### **6.3.1.1 Zeta-potential measurements**

Layer adsorption for each step was monitored by electrokinetic  $\zeta$ -potential measurements. For the purpose of these measurements, washings were carried out in DI H<sub>2</sub>O. Washing in this manner, as opposed to HBSS, was necessary to verify alterations

in surface charge with the addition of each polyelectrolyte layer. Figure 6.2 presents the net surface characteristics for MSCs encapsulated in two bilayers of PLL/BMP<sub>2</sub> and PLL/HA.

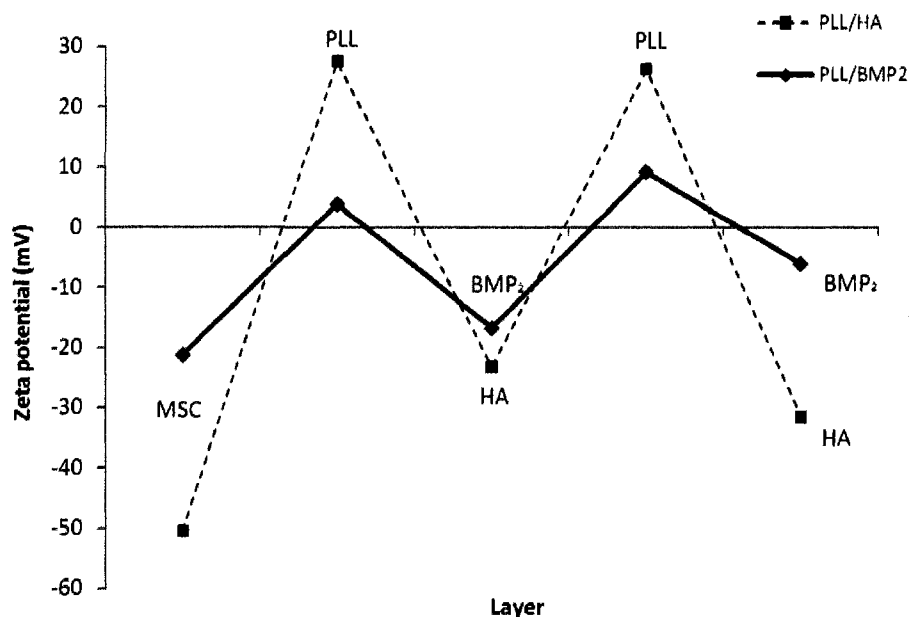


**Figure 6.2.** Surface charge inversions for encapsulated MSCs in PLL/HA and BMP<sub>2</sub>/HA bilayers

The addition of polymer and protein growth factors layers to the cell suspension results in alternation of surface charge with each deposition step. As shown in Figure 6.2, the  $\zeta$ -potential of bare MSCs is negative; however, the MSCs coated with PLL/BMP<sub>2</sub> carry a much smaller  $\zeta$ -potential ( $\sim -20$  mV) than those coated with PLL/HA layers ( $\sim -50$  mV). The PLL adsorption steps are also notably fewer for the BMP<sub>2</sub> preparation when compared with the HA preparation. In theory, one would expect similar surface charge measurements for deposition of PLL layers onto the cell templates. Two factors are in play here. One major influence is that there is a difference in electrostatic interactions between the layer ionizable groups. Secondly, the difference in the initial

concentration of cells used in the fabrication process may have affected these interactions based on ionizable groups or overall charge density which could determine the quality of subsequently deposited layers. Moreover, because proteins have the capacity to behave as dipoles, variations in the charge magnitudes could be attributed to various matrix proteins within the immediate environment, either synthesized by the stem cells and deposited in the pericellular matrix, or donated from the serum in the culture media [19, 95, 168].

When the terminating layer is PLL, the cell surface is positive. Similarly, with each HA or BMP<sub>2</sub> deposition step, the outermost layer of the cell is rendered negative. When PLL is a terminal layer, the cell surface is positive. Similarly, with each HA or BMP<sub>2</sub> deposition step, the outermost layer of the cell is rendered negative. One will notice that the PLL deposition steps which are alternated with HA have a smaller surface charge than the PLL alternated with BMP<sub>2</sub>. The differences in magnitude for the PLL-deposition steps when compared with the HA steps are a product of the chemical nature of each polyelectrolyte, and the pH at which the layers are assembled. HA has an isoelectric point of approximately 2.9 while both BMP<sub>2</sub> and PLL have isoelectric points of 9 [98]. For the case of the PLL/HA films, both polyions are almost completely dissociated at neutral pH, but PLL is more dissociated than HA, because the isoelectric point of PLL is further from the assembly pH than that of HA. According to Burke and Barrett, under these assembly conditions HA is more weakly charged and assumes a loopy conformation while PLL assumes a more rigid conformation [169]. In addition, HA is much larger than PLL, and thus carries a higher charge density.

For the case of the PLL/BMP<sub>2</sub> films the same behavior was expected. It is, however, noted that the behavior of polypeptides and proteins within LbL films is quite complex due to their non-uniform molecular conformation and surface charge densities [91]. Nonetheless, enough BMP<sub>2</sub> is deposited to allow for both the initial electrostatic interactions with the underlying layer, as well as surface charge reversal to allow for deposition of a subsequent layer. From additional  $\zeta$ -potential measurements over time, it was discovered that in theory, BMP<sub>2</sub> could be alternated with either a positive or negative PE, as the net charge characteristics of the protein are altered with time. The precise mechanism by which this charge ambiguity occurs is unknown, however, this observation is in agreement with the work of others, in which BMP<sub>2</sub> has been incorporated within LbL films as both cationic and anionic constituents [88, 89, 92].

#### **6.3.1.2 QCM measurements**

QCM analysis was completed at each growth step to monitor the layer deposition and determine the shell thicknesses produced. The results are shown in Figure 6.3. The PLL/HA bilayer thickness is approximately 1 nm, producing a two-bilayer shell of 2 nm thickness in the dry state. For a two-bilayer shell composed of PLL/BMP<sub>2</sub>, the thickness is around 4.5 nm. (Figure 6.3). In the hydrated state, the LbL multilayer thickness is approximately twice as large, with an estimated shell thickness of 6 and 9 nm, for layers with HA and BMP<sub>2</sub>, respectively [73, 108].

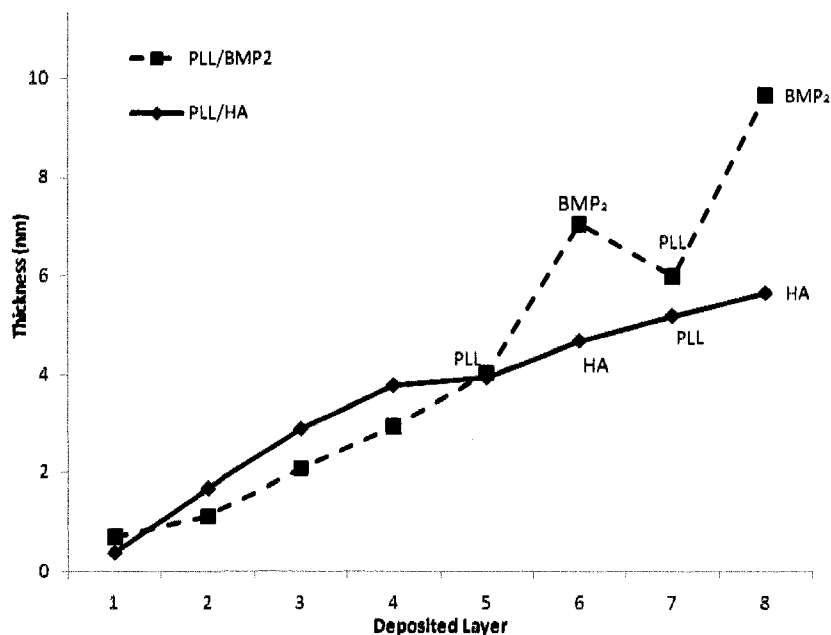


**Figure 6.3.** QCM for deposition two bilayers (PLL/HA) and (PLL/BMP<sub>2</sub>)

The peaks which appear in the figure correspond to the adsorption steps for BMP<sub>2</sub>. It is noted that adsorption of PLL onto the BMP<sub>2</sub> layer causes an increase in resonator frequency, which correlated to a decrease in thickness by roughly 1 nm. With the next BMP<sub>2</sub> deposition step, the thickness increases again by around 2.5 nm. Based on the observations here, it is hypothesized that upon immersion of the coated cells in culture media, portions of the BMP<sub>2</sub> layer are immediately solubilized, decreasing the total shell thickness.

### **6.3.1.3 Fluorescence microscopy**

To visually confirm the presence of polyelectrolyte layers on the MSC templates and to assess biocompatibility, the encapsulation process was repeated using fluorescein isothiocyanate (FITC) tagged PLL. The FITC molecule covalently binds to exposed amine residues, causing the PLL molecule to fluoresce at 530 nm when excited with 488 nm laser light. Figure 6.4 shows the results.

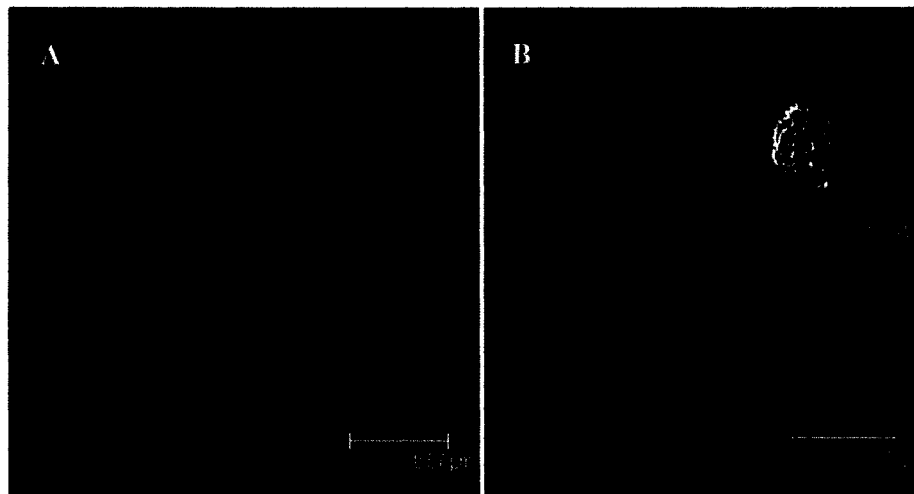


**Figure 6.4.** Confocal Micrograph for MSC/PLL/HA. Confocal micrographs of MSCs encapsulated within PLL-FITC/HA at (A) three days post-encapsulation and (B) seven days post-encapsulation. Insets show phase micrograph for reference. (Leica Laser Scanning Confocal Microscope, SP2).

The confocal image at three days post-encapsulation clearly shows the adsorption of PLL onto the cell membrane, forming an exact template (Figure 4A). The confocal micrograph at seven days post-encapsulation (Figure 4B), however, does not show the presence of a discrete red fluorescent layer and demonstrates a greater amount of fluorescence within the cell when compared with the three-day image. The presence of PLL-FITC within the immediate pericellular matrix is attributed to the ability of free PLL to diffuse in and out of the PLL/HA film, coupled with endocytosis of the polyelectrolyte [88, 89, 98, 170, 171].

*In vitro* cell viability studies were conducted using MSCs encapsulated within three bilayers of PLL/HA. Polyelectrolyte solutions were prepared in DI H<sub>2</sub>O, HBSS, or 0.5 M NaCl and adsorbed onto the cell as described earlier. For each preparation, cells were seeded at a density of 5000 cells/cm<sup>2</sup> and viability was assessed using the Live/Dead Assay (Biovision). Images were acquired with a Nikon microscope coupled to a Nikon E995 digital camera. In terms of viability, similar results were observed over the

seven-day period for all solvents (Figure 6.5). For cells to remain viable in culture, proper pH, osmotic and ionic balance are crucial. This notion brings about the conclusion that although the cell are exposed to PEs dissolved in unbalanced solvents for several minutes, they are either not greatly affected or have the ability to recover from a negative outcome. After each deposition step of shell buildup, the cells undergo three washings in HBSS. This medium contains various salts which support cellular function and nutrient transport. Undoubtedly, these washings play a role in the maintenance of membrane integrity and cellular viability.

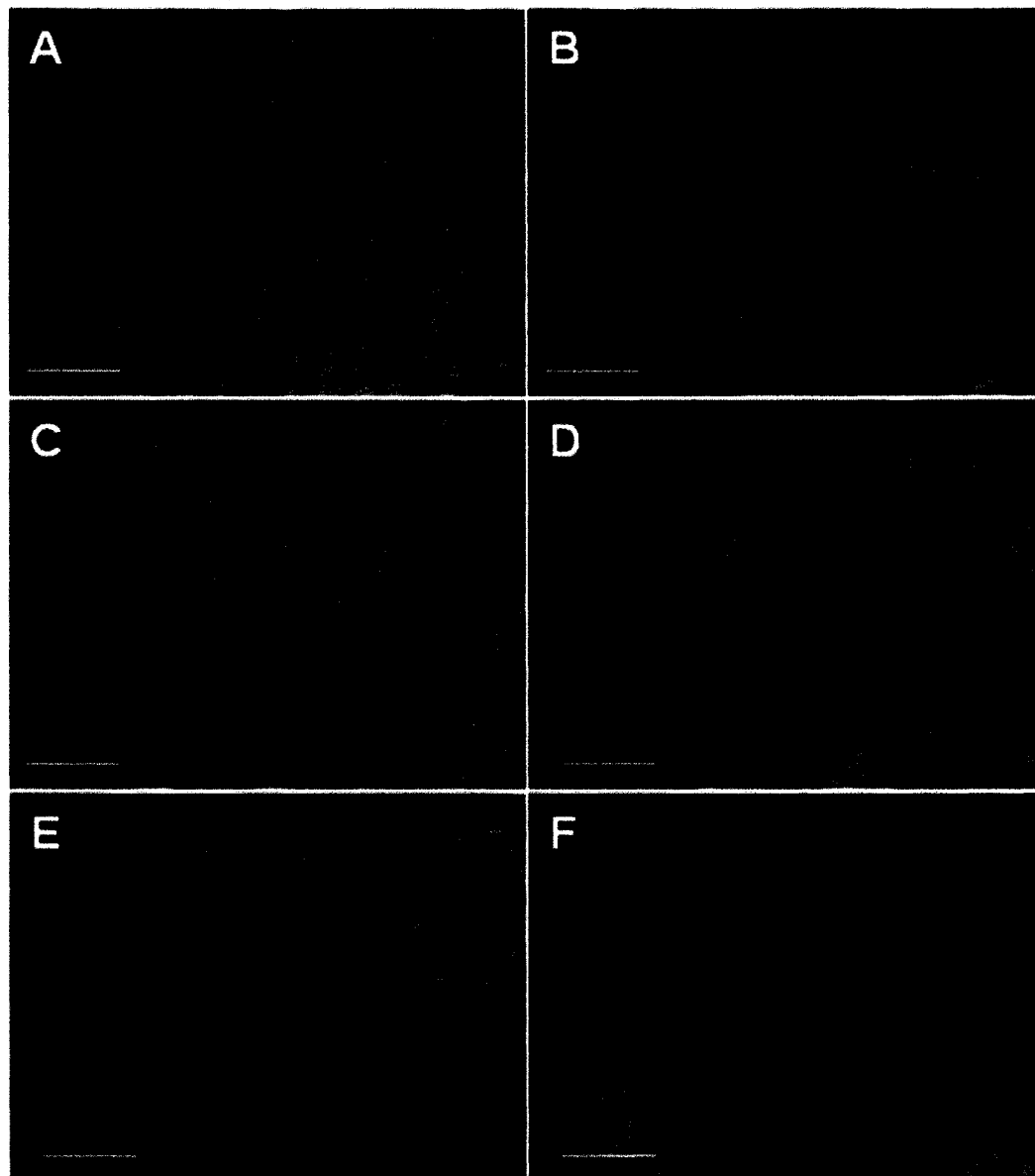


**Figure 6.5.** Live/Dead images of MSCs encapsulated within three bilayers of PLL/HA. Polyelectrolytes were suspended in deionized water (A-12 hrs post-encapsulation and B-7 days post-encapsulation), 0.5 M NaCl solution (C and D, 12 hrs and 7 days post-encapsulation), and HBSS (E and F, 12 hrs and 7 days post-encapsulation). The scale bars on each image represent 50  $\mu\text{m}$ .

Similar morphological results to those seen in Figure 6.5 were obtained when the encapsulated cells were observed with bright field microscopy. Cell clusters and aggregates form (Figure 6.6) after 6 days.

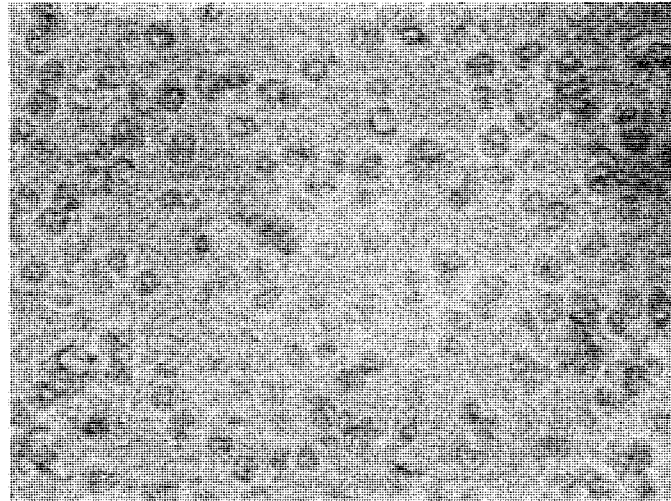


**Figure 6.6.** Bright field image of MSCs within PLL/HA shells at 6 days post-encapsulation. Polyelectrolytes were dissolved in HBSS. The image was acquired with Nikon system. Original magnification, 100X.

#### **6.3.1.4 Mitochondrial activity**

The MTT Assay (Invitrogen) was performed at one, three, and seven days post-encapsulation. MSCs coated with two bilayers of PLL/HA were seeded at a density of 10, 000 cells per well in a 96-well plate and incubated in a growth medium for the designated time period. The cells were incubated in MTT solution overnight. The formazan precipitate was dissolved with 100  $\mu$ L of MTT solvent (Sigma) and absorbance was immediately measured at 570 nm using a reference wavelength of 690 nm (Tecan spectrophotometer). The results of the MTT Assay for PEs dissolved in HBSS is provided in Figure 6.7.

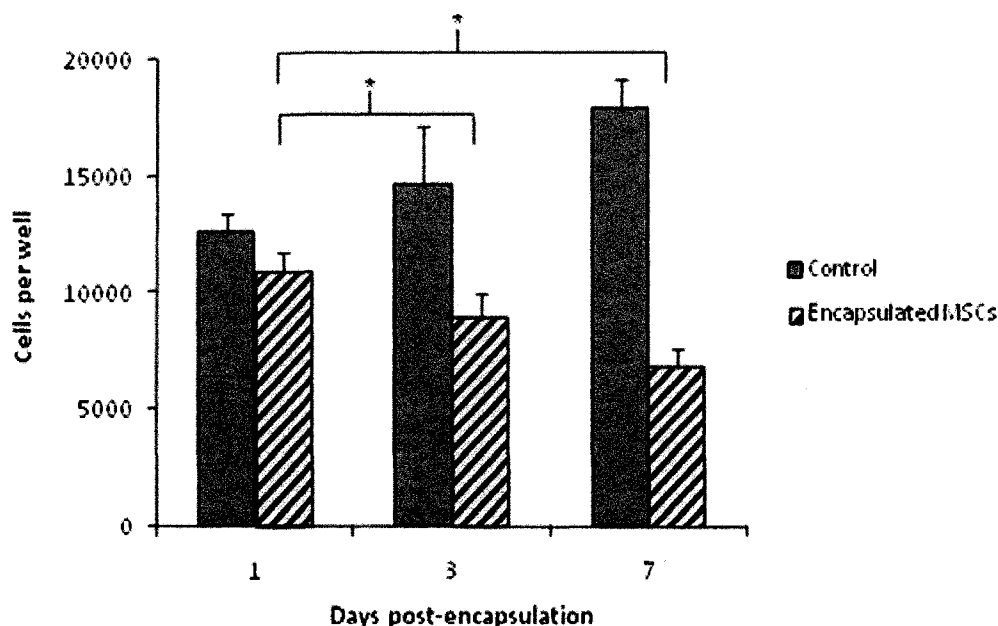


**Figure 6.7.** MTT Assay for MSCs encapsulated within two bilayers of PLL/HA. Control cells were grown without deposition of multilayer shells. Polyelectrolytes were suspended in HBSS and then adsorbed onto MSCs as described above. A student's t-test with  $p=0.05$  was used to determine statistical significance (denoted by the asterisks).

The uncoated cells showed a steady increase in metabolic activity between one and seven days of maintenance. Conversely, the metabolic activity of the encapsulated cells steadily declined over the seven-day culture period. As shown in Figure 6.7, a significant decrease in mitochondrial activity, and thus cell proliferation, was noted between one and three, and one and seven days post-encapsulation. There is no significant decrease between metabolic activity between the two groups at 1 day post-encapsulation, but as the encapsulation time is extended, the difference between the controls and encapsulated cell metabolic activity becomes increasingly great. The argument can be made that since the cells are not in their native environment, i.e. anchored to a substrate, the results seen here could simply indicate that they are not as mitochondrially active, but still viable.

Initially, cell viability could not be confirmed through Trypan Blue and MTT staining. It was assumed that the polyelectrolyte layers were permeable only to small-molecular-weight molecules. However, this hypothesis was nullified upon inspection of the molecular weights of the molecules used. Trypan Blue and MTT have molecular weights of 892 and 414, respectively. The Live/Dead Assay uses molecules which permeate the cell and form the fluorescent compounds calcein AM (MW 995) and ethidium homodimer-1 (MW 1293). It has been shown that polyelectrolyte multilayers are permeable to molecules with a Mw less than 3000 [73, 108]. Based on size comparisons, if the latter two can permeate the polyelectrolyte shell, one would expect that Trypan Blue and MTT would have the same potential. Further optimization of experimental conditions demonstrated the necessity to incubate cells in the MTT solution and Trypan Blue for a time period greater than what would conventionally be used. These results are likely due to the increased diffusion pathlength from addition of the polyelectrolyte layers. It is possible that we did not find any obstacles with the Live/Dead Assay simply because of its high sensitivity and fluorescent nature.

HA is a natural, linear polysaccharide comprised of D-glucuronic acid and N-acetyl-D-glucosamine. It is a chief component in connective tissue ECM, and plays a role in wound healing, among several other biological processes [98, 169, 170]. The natural cation, PLL, is a linear polypeptide containing an amino group and has been widely used in biomaterial applications to enhance cell adhesion [95, 169, 170]. Previously, characterization of PLL/HA multilayer films generated by LbL has been achieved using atomic force microscopy (AFM),  $\zeta$ -potential measurements, quartz crystal microbalance (QCM) monitoring, and contact-angle measurements [98, 169, 170]. Thus, the promise

of using these and other biologically friendly molecules with ionizable groups was further investigated in this work.

### **6.3.2 HDF Encapsulation in TGF $\beta$ <sub>1</sub> Functionalized Shells**

Using human dermal fibroblasts as anionic templates, the protein growth factor TGF $\beta$ <sub>1</sub> was incorporated into the layer coatings. For this purpose, three layering schemes were considered: deep (D), double-layered (DL), and superficial (SF). Table 6.2 elaborates the film architectures consisting of seven layers, which were built-up onto the HDFs.

**Table 6.2** PLL/TGF $\beta$ <sub>1</sub> Layer Architectures

<b>SCHEME</b>	<b>ARCHITECTURE</b>
D	(PLL/TGF $\beta$ <sub>1</sub> )/(PLL/HA) <sub>2</sub> -PLL
DL	(PLL/TGF $\beta$ <sub>1</sub> ) <sub>3</sub> -PLL
SF	(PLL/HA) <sub>2</sub> (PLL/TGF $\beta$ <sub>1</sub> )-PLL

#### **6.3.2.1 Zeta-potential measurements**

For the purpose of these measurements, intermediate washings were carried out in DI H<sub>2</sub>O. 1.5 mL of PE was added to a 3x10<sup>9</sup> cells, giving an initial concentration of 0.5 million cells/mL. A deposition time of 20 minutes was used for incorporation of TGF $\beta$ <sub>1</sub> within the cellular capsule. The results are provided in Figure 6.8. The HDF cell template carries a moderate negative charge of around -33 mV. Deposition of the PLL layer reverses the surface charge so that it carries a  $\zeta$ -potential of approximately +20 mV. With each additional deposition step, the surface charge reverses, demonstrating that the layers are being assembled electrostatically. It is noted that the  $\zeta$ -potential values obtained for TGF $\beta$ <sub>1</sub> layers are weaker than those of HA. However, in comparison to the

results for PLL/HA and PLL/BMP<sub>2</sub> layers on MSCs presented in Section 6.3.1.1, the  $\zeta$ -potential measurements for all deposition steps are moderately to strongly charged, meaning that the initial cell concentration in plays a critical role in establishing strongly charged layer interactions.

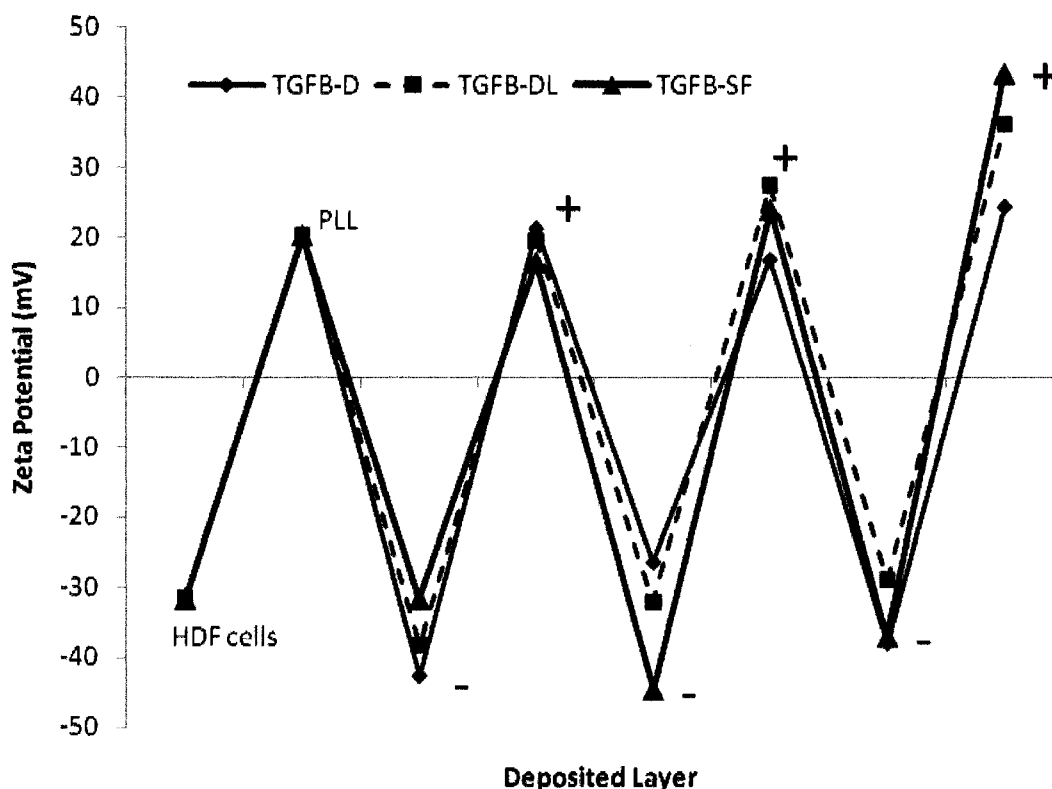


**Figure 6.8.** Adsorption kinetics as monitored by zeta-potential for growth factor incorporation in films (D, DL, SF). Initial amount of cells used was  $4.5 \times 10^6$ .

### 6.3.2.2 QCM Measurements

The QCM technique was employed to determine the thickness of TGF $\beta_1$ -embedded cellular coatings, and measurements were obtained as previously described in Section 5.3.2.1. As depicted in Figure 6.9, the growth step of a PLL/TGF $\beta_1$  bilayer corresponds to a thickness of approximately 3 nm. For a complete shell with TGF $\beta_1$  incorporated in one of the layering modalities, the total cell coating is only about 12 nm.

Again, it is expected that in aqueous solution, the LbL assembled layer thicknesses are doubled, thus a coating with embedded  $\text{TGF}\beta_1$  has a total shell thickness of around 24 nm.

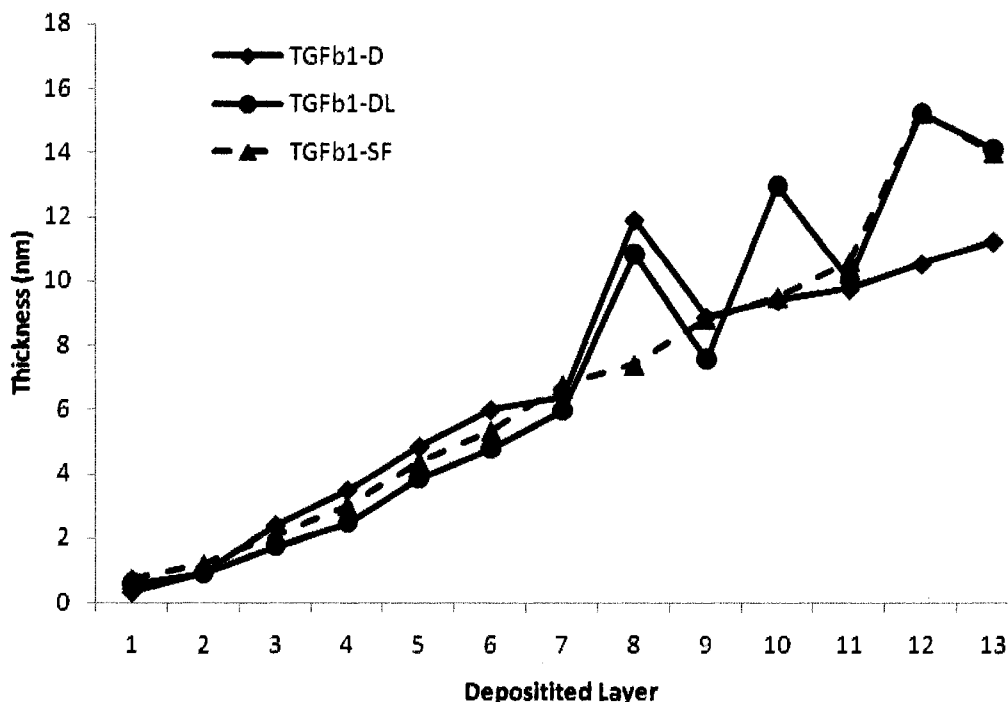


Figure 6.9. QCM for encapsulated HDFs comparing  $\text{TGF}\beta_1$  in the D, DL, SF modalities

The largest growth steps occur with deposition of  $\text{TGF}\beta_1$  layers, however, after deposition of  $\text{TGF}\beta_1$  the resonator frequency increases, suggesting that mass is being lost. The underlying principle regarding the observed QCM results is simply that the  $\text{TGF}\beta_1$  layers are being solubilized upon deposition of a PLL layer.

### 6.3.2.3 Viability of encapsulated HDFs

As a final extension of this work, several various bilayer combinations were deposited onto HDF templates. 25,000 cells were used in each instance for buildup of thin film capsules. Those PE pairs included (PDDA/PSS), (PLL/HA), ( $\text{TGF}\beta_1$ /HA), (PS/CS), (PS/PLAA), ( $\text{TGF}\beta_1$ /TiO<sub>2</sub>), (GelA/GelB), and (GelB/CS). The MTT Assay

was used as a means of comparing cellular response at 3 days post-encapsulation for each of the preparations. Table 6.3 provides initial  $\zeta$ -potential measurements.

**Table 6.3** Surface Charge Inversions for Encapsulated HDFs Comparing Different Layering Schemes, n=7.

<i>SCHEME</i>	<i>Cell Template</i>	<i>Layer 1</i>	<i>Layer 2</i>	<i>Layer 3</i>	<i>Layer 4</i>
1	-12.47	PDDA 17.86	PSS -21.18	PDDA 13.27	PSS -24.33
2	-15.18	PLL 11.63	HA -14.35	PLL 14.16	HA -17.12
3	-13.74	TGF $\beta_1$ -4.18	HA -17.36	TGF $\beta_1$ -8.42	HA -21.15
4	-17.12	PS 7.13	CS -21.49	PS 13.04	CS -16.27
5	-16.23	PS 9.44	PLAA -14.21	PS 13.41	PLAA -19.93
6	-15.21	TiO <sub>2</sub> 8.18	PLAA -6.14	TiO <sub>2</sub> 12.29	PLAA -7.13

In each case, the magnitude of charge at the cell template is around -15 mV. Proper surface charge alteration was seen in most instances, as the numbers change sign with each subsequent layer. In scheme 3, the net charge of TGF $\beta_1$  is -4.18 with its first deposition step, followed by a negative charge of -17.36 for the HA deposition step. The fact that the magnitude of charge is small but does not cross zero could be an indication that there are not a sufficient number of charged sites at which HA can adsorb, neutralize, and then reverse the sign. The three-day cellular response to encapsulation within shells of various constituents is presented here in Figure 6.10.

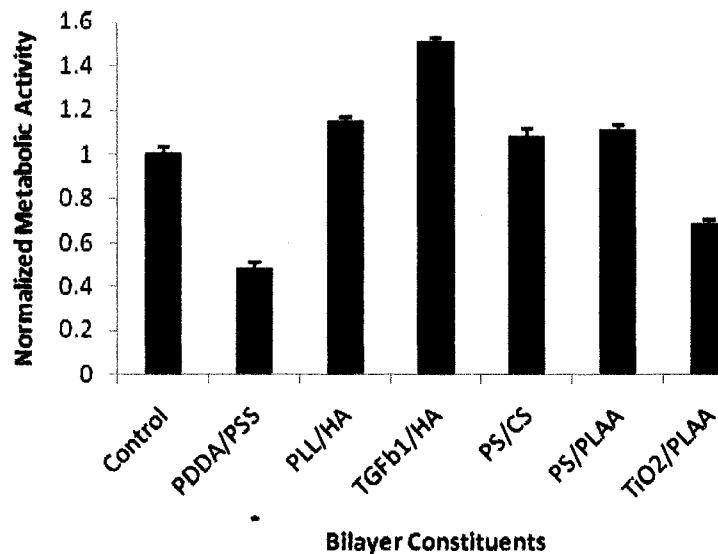


**Figure 6.10.** MTT results for various shell constituents. Control cells were grown without deposition of multilayer shells. Polyelectrolytes were suspended in HBSS and then adsorbed onto MSCs as described above. A student's t-test with  $p=0.05$  was used to determine statistical significance,  $n=3$ .

The control group received no supplementation or additional modifications. During this time-frame, the HDFs encapsulated within shells of TGFβ<sub>1</sub> and HA had the highest relative metabolic activity. HDFs encased in shells of the synthetic PEs PDDA and PSS showed the smallest metabolic activity after three days of encapsulation. Schemes 1 and 3 showed metabolic activity that was statistically significant from the controls, when a two-tailed student's t-test was employed.

#### 6.4 Conclusions

The largely preliminary work presented here describes the ability to buildup thin films on individual mammalian cells. Investigations into film growth, such as the case for the layer combination PLL/HA have established that the self-assembly process of natural PEs is comparable to that of synthetic polyelectrolyte multilayer films, whereby the surface charge is overcompensated after each polyion deposition step. Moreover,

bioactive molecules can be embedded within the film architecture via covalent or electrostatic interactions without loss of their functional integrity [170]. The inherent biocompatibility of PLL and HA make their combination highly desirable in tissue engineering, pharmaceuticals, and other biological applications [98, 169].

There are several key areas that must be investigated to further this technology for inclusion in bioactive implant systems. For example, MSC encapsulation in layers of PLL/HA, was met with a significant decrease in cell viability between one and three, and one and seven days post-encapsulation. One possibility is that the addition of polyelectrolyte layers causes some disruption in membrane integrity. Germain et al. demonstrated that after deposition of each bilayers, incubation of their cell suspensions for two hours at 37°C in buffer solution increased cell viability [172]. They further postulated that weak polyelectrolyte interactions may assist with shell flexibility and further prolong viability by reducing mechanical tension on the cell surface. This is supported by AFM studies wherein high ionic strength solutions had more flexible shells when compared with cells encapsulated in polyelectrolytes of low ionic strength [155].

Certainly, further cell viability tests over the long term coupled with AFM examinations for information concerning shell stiffness and durability, will provide additional insights into how this technology can be translated into the clinical realm. While our preliminary results are promising, examination of shell permeability is critical in assessing the longevity of encapsulated cells.

The ability to include growth factors, biomolecules, and therapeutics within the cell capsules will further contribute to the development of a comprehensive tissue-engineered product. Therefore, determination of the requisite positioning and

combination of factors needed to induce differentiation into specific cell types must be addressed. Fluorescent immunochemistry, SDS page, and ELISA may prove to be especially useful in accomplishing this task. Complementary studies in adsorption kinetics for the embedded proteins, growth factors, or drugs must also be performed, to determine optimal deposition times. Finally, the precise encapsulation efficiencies for various coating preparations was not determined, but would prove useful in conjunction with long term biocompatibility studies as far as scale-up and cost-efficiency are concerned.

## CHAPTER 7

### CONCLUSIONS AND FUTURE WORK

#### 7.1 Conclusions

There are trends towards production of multifunctional biomedical devices which can incorporate varying chemical, mechanical, and biological characteristics simultaneously and synergistically. The presented study described the fabrication, characterization and testing of novel LbL assemblies for incorporation into tissue engineering systems. The simplicity, versatility, and power of LbL to influence cellular behavior represents a major inroad in terms of using novel, nanoengineered approaches for construction of complex, yet functional assemblies which can be exploited for the improvement of clinical problems. First, the expedited or slowed release of dexamethasone (DEX) through with DEX aggregates (directly template drug crystals) or DLCAMs (drug physically immobilized in alginate microspheres) was achieved. The presence of DEX aggregates in culture medium directed bovine TMJ fibrochondrocytes toward the chondrocyte phenotype when compared with positive and negative controls. In another section, ultrasonic nebulization was used to expedite LbL coatings on planar substrates. The formation of multi-architecture films with embedded DEX, TiO<sub>2</sub> nanoparticles, and the protein growth factor TGFβ<sub>1</sub> collectively, shows an elegant method for enhancing for controlling, enhancing, and optimizing cellular response based on

variations in spray distance, deposition times, and layer composition. Finally, mouse mesenchymal stem cells (MSC) and human dermal fibroblasts (HDF) show the ability to remain viable while individually encapsulated within multilayer shells of varying compositions. Moreover, incorporation of complex molecular structures, such as TGF $\beta$ <sub>1</sub>, within the shell assembly resulted in heightened cellular mitochondrial activity in comparison with other shell architectures and unencapsulated cells.

## **7.2 Future Work**

### **7.2.1 Controlled-Release Technology**

From a clinical perspective, bioavailability of therapeutics in varying quantities over different time frames is ideal in a tissue-engineered setting. Based on the results of DEX release from DLCAMs, a sustained release of the drug is theoretically possible for a period of four months. This behavior is distinctively different from the expedited drug release from DEX aggregates, and from a practicality standpoint have a much greater potential for incorporation into a tissue-engineered structure. With that said, however, it is unknown whether the DEX release from DLCAMs remains pharmacologically and biologically active over a period of more than a few days. Further optimization studies of drug release from the calcium alginate matrices should be explored in terms of drug loading, cross-linking concentrations, sonication power, and mixing speed during the fabrication process. On a larger scale, the need for a significant amount of testing and characterization of *in vivo* cellular behavior correlated to microsphere degradation behavior, an thin film coatings, as well as analysis of the chemical composition of the drug over extended time periods is underscored.

Other possibilities for this technology include multi-stage timed release of various biologically relevant molecules, for example, multiple growth factors with precisely controlled-release behavior from a single system. An interesting approach to this prospect is successive encapsulations of varying growth factors using calcium alginate microspheres as spacers.

### **7.2.2 Nebulized Substrates with Bioactive Functionality**

Variations in the LbL process in concerning surface topography and adsorption kinetics were noted between the traditional substrate-dipping process and nebulization. When incorporated in different positions within nebulized film assemblies, HDF response to TGF $\beta_1$  was modulated over a three-week period, due likely to temporal and spatial concentration differences. Investigations into the specific release behavior of TGF $\beta_1$  should be pursued to elucidate this and other observations. Also, the noted difference in size between positive controls (cells grown on glass slides cultured in TGF $\beta_1$ -supplemented media) and the nebulized assemblies is still elusive. Thus, the interactions between cell behavior, protein adsorption characteristics, and topographical features should be further explored. In addition, the possibility of architectures consisting of multiple growth factors and varying concentration gradients could produce interesting cellular behaviors and varying phenotypes, towards the goal of generating tissues which closely approximate native cellular organization.

On a larger scale, this technology can be easily modified, for example, as a method to produce anti-microbial coatings on dental implants, in the fabrication of a bioactive bandage, which encourages enhanced hemostasis and wound-healing, or for optical, electronic and other properties towards the design of biosensor platforms and

arrays. The ability to functionalize the films with specific ligands or antibodies could also be used as a novel cell-recruitment system.

### **7.2.3 Cellular Encapsulation**

The ultimate purpose of the cell encapsulates is implantation or engraftment into a tissue defect to assume a particular therapeutic action. Despite the numerous strides in development of cell encapsulation technologies, implant failure remains a barrier to clinical implementation. Among the largely unresolved issues is attack by the host immune system. Within the shell layers, inclusion of anti-inflammatory agents such as DEX and Ketoprofen could assist in preventing acute inflammatory responses.

The ability to closely mimic natural encapsulation processes, such as that witnessed during embryonic development of the *Drosophila melanogaster* [173], could be a solution to increasing cell viability. Encapsulation also allows insect hosts to survive infection by parasitoids, and permits bacteria to maintain their virulence via secretion of a protective polysaccharide matrix [174, 175]. Further investigation into these natural methods of protective capsule formation may provide a basis for optimal material selection concerning fabrication of permeable, biocompatible, nanothin layers onto cells.

Other possibilities of this research branch out into a few directions. For example, cell populations could be primed within the 3-D capsules and then later dissolve leaving the cell intact and healthy and available for other uses. Also, there is the potential to produced organized tissue of varying cellular contents based on self-assembly of cells with oppositely charged coatings.

As a final thought, the flexibility and robustness of this technology expresses that there are endless possibilities for integration of these three technologies to produce novel composite materials to overcome obstacles in the field of tissue engineering and implant modification, to better control cellular function and tissue organization.

**APPENDIX A**

**PROTOCOL FOR FABRICATION OF CALCIUM**

**ALGINATE MICROSPHERES**

**Procedure**

Briefly, 0.75 g of low viscosity alginic acid sodium salt was slowly dissolved in 24 mL of deionized water while stirring with a propeller style stirrer at a setting of 1.5 for 10 minutes. The desired amount of dexamethasone was added to the mixture and stirred for an additional 5 minutes. A mixture of 54 mL of isooctane (EMD Chemicals) and 0.848 g Span-85 was ultrasonicated for 1 minute at 39 W. The alginate/drug mixture was then added to the isooctane/span mixture and sonicated at the same power for 5 minutes. Further sonication for an additional 2.5 minutes was performed after adding a mixture of 2.95 mL of isooctane and .45 mL of Tween-85. The mixture was then stirred for 20 minutes while slowly adding 10 mL of a 10% calcium chloride solution in deionized water. The emulsion was diluted with 500 mL of deionized water, added to a separatory funnel, and collected. Three washings by centrifugation for 3 minutes at 3000 rpm were performed before use for experiments.

## **APPENDIX B**

### **FITC-CONJUGATION PROTOCOL**

### **Materials and Equipment Needed**

- FITC
- PBS
- 0.5 M Carbonate buffer
- 10 mL test tubes
- Protein or Peptide
- DMSO
- Vortex
- PD-10 column

### **Procedure**

The following protocol can be used to couple FITC to amine residues, as was done in the case of complexing PLL to FITC.

1. Dissolve 2mg of protein/peptide in 1mL of PBS (pH 8.0) in clean 16x125mm polypropylene test tube. If needed, adjust pH to 8.0 using 0.5M carbonate buffer.
2. Prepare fresh, 1mg/mL of FITC in DMSO. Add 75uL of FITC/DMSO solution to protein/peptide while vortexing.
3. Incubate at room temperature for 45minutes.
4. Using a PD-10 column, wash PD-10 with 30mL of PBS.
5. Add the 1mL FITC-protein/peptide solution after the top of column is almost dry.
6. Close stopcock to stop flow after the protein/peptide has eluted into the column.
7. Add 5mL of PBS on top.
8. Open Stopcock. collect in 2mL fractions, discarding the first 2mL and keeping the 2nd 2mL fraction. The second 2mL fraction contains the conjugated protein/polypeptide\*.

**\*NOTE:** This step is appropriate only if 1mL of conjugated-protein/polyelectrolyte is added to the column. If 2mL of conjugated-Ig is added, discard first 1mL and keep the next 4mL. The antibody is always diluted by 2x after leaving the column.

## **APPENDIX C**

### **WST-1 ASSAY**

### **Materials and Equipment Needed**

- Flat bottomed 96-well plates
- Cell Culture medium
- WST-1 Cell Proliferation Reagent

### **Procedure**

1. Culture cells in flat bottomed 96-well plates in a final volume of 100  $\mu\text{L}$ /well culture medium in a humidified atmosphere (e.g. 37°C, 5% CO<sub>2</sub>). Reserve one well as a background control (culture medium without cells).

**Note:** The incubation period and cell density of the culture depend on the particular experimental conditions and on the cell line used. For most experimental setups, a cell density between 10<sup>3</sup> and 5 x 10<sup>4</sup> cells/well and an incubation time of 24 to 96 hr is appropriate.

2. Add 10  $\mu\text{L}$  of Premixed WST-1 Cell Proliferation Reagent to each well (1:10 final dilution).

**Note:** Premixed WST-1 Cell Proliferation Reagent should be used at a final dilution of 1:10. If cells are cultured in 200  $\mu\text{L}$  culture medium, add 20  $\mu\text{L}$  Premixed WST-1 Cell Proliferation Reagent per well.

3. Incubate the plate for 0.5 to 4 hr at 37°C in a humidified atmosphere maintained at 5% CO<sub>2</sub>.
4. Measure the absorbance at 420–480 nm (maximum absorption is at ~440 nm), using a spectrophotometric plate reader. The reference wavelength should be greater than 600 nm. Shake thoroughly for 1 minute before measurement.

**Note:** The absorbance level of the background control well (containing culture medium plus Premixed WST-1 Cell Proliferation Reagent, without cells) will depend on the culture medium, incubation time, and exposure to light. Typical background absorbance after 2 hr is between 0.1–0.2 absorbance units.

**APPENDIX D**

**IMMUNOCYTOCHEMICAL LOCALIZATION  
OF CELLULAR ANTIGENS**

### **Materials and Equipment Needed**

- Cell culture media
- HBSS without phenol red
- 95% ethanol
- Kim wipes
- Primary and secondary antibodies
- Petri dishes
- Coverslips or glass slides
- Transfer pipettes
- PBS
- PBS-Tween
- BrdU powder (if detecting BrdU)

Incorporate BrdU into cells by making a solution BrdU powder in HBSS without phenol red to make a concentration of 5 mg/mL

**NOTE:** If BrdU is to be detected, BrdU must be incorporated into the cells at least one day before immunocytochemistry. Additionally, nuclear permeabilization step must be done using a 1 N HCl solution.

#### **For Enzyme Substrate Detection:**

- Anti-mouse Kit (ABC detection)
- DAB, HistoMark Orange or other chromagen
- Hematoxylin or Contrast Green
- Plastic box

#### **For Fluorescent Detection:**

- 0.25-0.5% Triton X-100 in PBS

### **Procedure**

1. Trypsinize cells and seed onto glass slides at appropriate density. Place a few drops of cell suspension in the center of the coverslip
2. Incubate at 37 C for 10 minutes (cells have not yet attached, so carry them carefully so you don't disturb the cells)
3. Add complete media **around** the cell area. **DO NOT ADD ON TOP OF CELL SUSPENSION AS THIS WILL DISTURB CELLS.** You may then add enough media to cover bottom of dish and glass slides so that cells do not become dehydrated.
4. Incubate overnight so that cells are allowed to attach.
5. Verify attachment, if attachment has not occurred, add a few drops of media only to the area in which the cells were placed. Do not remove any media. Check back periodically.

6. After cells have attached, remove excess media from Petri dishes and slides using a non-sterile transfer pipette.
7. Fix cells with 95% ethanol, for 3-5 minutes (you should see a white residue)
8. Use KimWipes to gently remove moisture from around the cells. Then draw a ring around the cells with a hydrophobic Pap Pen (this holds the subsequent reactions within this area). Do not let ink from pen touch the cells. Label the coverslips "Experiment" and "Control".
9. Rinse 5 times for 2 min in PBS-T to permeabilize the cell membrane.
10. If a peroxidase marker is used, block endogenous peroxidase by incubating in 3% H<sub>2</sub>O<sub>2</sub> in PBS of 10-30 minutes. If other marker is used, such as avidin-biotin, or fluorescence, omit this step
11. Rinse 3 times for 5 min in PBS.
12. Block with 2-5% normal serum in PBS for 20 minutes (Normal serum should be the same species as the secondary antibody is raised). Place open Petri dish into plastic container with cover and incubate at room temperature.  
  
**Note:** If using avidin-biotin detection system, avidin/biotin block may be needed based on cell type. If you do, the avidin/biotin block should be done after normal serum block.  
  
If antibody is to be complexed to a fluorescent marker, this should be done a few minutes before this step and should be kept away from light.
13. Incubate experimental slides with primary antibody for 1 hour. Add same amount of PBS to control slides.
14. Decant the primary antibody solution, and immediately wash the dish 3x5 min with PBS. Do not let the cells dry at any step. Especially during washing, handle each dish individually since leaving a washed dish without medium for even a few seconds can allow drying in the center of the dish.
15. Add the secondary antibody and incubate for 30-60 minutes at room temperature.
16. Decant the secondary antibody and wash the cells 3x5 min in PBS.
17. If using the avidin/biotin detection method, apply one drop of **ABC reagent** and incubate at room temperature for 30 minutes

**NOTE:** If using DAB as a chromagen, follow steps 18-27

18. Make up DAB (unstable at room temp and light sensitive...must be made not more than 1hr before it is used):
  - Use tweezers to place one tablet into mixing bottle
  - Add 10 ml type I water and dissolve by shaking for 2-3 minutes
  - Add one drop of peroxide solution to mixing bottle and invert gently for about 30 seconds.
19. Wash cells immediately with PBS and then again for 5 minutes. Remove excess moisture with KimWipe
20. Apply DAB and incubate for 7-10 minutes in dark (place covered Petri dish in a box or cut off light in hood).
21. Terminate the reaction by washing with tap water (add and remove water a few times). If a reaction has occurred the experimental cells should appear brown in color.
22. Add 3-4 drops of hematoxylin to cells and incubate for 5 minutes.
23. Rinse in tap water by adding and removing until rinse water is colorless.
24. Rinse in acid rinse by adding a small amount every 2-3 seconds about 10 times, then pour back into glass container.
25. Immediately rinse in tap water by adding and removing about 10 times.
26. Add bluing solution to cells and incubate for 1 minute at room temperature.
27. Rinse in tap water about 10 times.
- 28.. Remove from Petri dishes. Allow slips to air dry for approximately 5 minutes on KimWipes.
29. Fix the cells again using 3.7% formaldehyde freshly made as performed in the initial fixation. The purpose of the second fixation is to crosslink the antibodies in place and to prevent subsequent diffusion of label. If not post-fixed in this way, the localization may not be stable for more than a few hours.
30. Mount the cells with mounting medium and coverslip. Anti-fading mounting medium is needed for fluorescent applications.

## **APPENDIX E**

### **MTT ASSAY**

**Procedure**

A stock solution of (3-(4,5-dimethylthiazol-2-yl)-2,5-diphenyltetrazolium bromide (MTT) was prepared at 5 mg/mL in PBS. The stock solution was further diluted in completed DMEM in a 1:10 ratio. The 10% working solution was freshly prepared before each use. For each sampling point (4, 7, 14, 21 days) cell culture media was decanted and the glass substrates for each treatment were rinsed thrice in HBSS without phenol red. A volume of 100  $\mu$ L of MTT working solution was added to the samples and the cells were incubated for a period of 24 hours at 37C. Subsequent to the incubation time, the purple formazan precipitate was dissolved with 100  $\mu$ L of 70% isopropyl alcohol. The solutions were then transferred to 96-well plates and absorbance was immediately measured at 570 nm using a reference wavelength of 690 nm (Tecan spectrophotometer).

**APPENDIX F**

**CELL LYSIS PROTOCOL**

### **Procedure**

Briefly, cells were lifted from substrates through trypsinization, transferred to 15 mL conical tubes, and collected by centrifugation at 1200 rpm for 5 minutes. Each pellet was resuspended in 1.5 mL of cold PBS and centrifuged at 1200 rpm for 5 minutes at 4°C. Cells were resuspended in 150 µL cell lysis solution (Sigma) and kept on ice for 15 minutes. Finally, the preparation was centrifuged at 3200 rpm for 20 minutes at 4°C. The supernatant was recovered and stored at -20°C until needed for further use.

Quant-iT™ PicoGreen® dsDNA reagent (Invitrogen) was used to quantify the amount of DNA present in the samples' cell lysate. The PicoGreen reagent was diluted 1:200 in 1X TE buffer and protected from light. In a black 96-well plate, 10 µL of cell lysate was diluted in 90 µL TE buffer. The PicoGreen working solution was then added to each sample in a volume of 100 µL. The plates were incubated for 5 minutes in the dark. An excitation wavelength of 485 nm was used, and fluorescence intensity was read at an emission wavelength of 538 nm (Tecan Genios Platereader).

## REFERENCES

1. Sharma, B. and J.H. Elisseeff, *Engineering structurally organized cartilage and bone tissues*. Ann Biomed Eng, 2004. **32**(1): p. 148-59.
2. Desai, T.A., *Micro- and nanoscale structures for tissue engineering constructs*. Med Eng Phys, 2000. **22**(9): p. 595-606.
3. Moiola, E.K., et al., *Matrices and scaffolds for drug delivery in dental, oral and craniofacial tissue engineering*. Adv Drug Deliv Rev, 2007. **59**(4-5): p. 308-24.
4. Puleo, D.A. and A. Nanci, *Understanding and controlling the bone-implant interface*. Biomaterials, 1999. **20**(23-24): p. 2311-21.
5. Le Guehennec, L., et al., *Surface treatments of titanium dental implants for rapid osseointegration*. Dent Mater, 2007. **23**(7): p. 844-54.
6. Meijer, G.J., et al., *Cell-based bone tissue engineering*. PLoS Med, 2007. **4**(2): p. e9.
7. Wan, Y., et al., *Adhesion and proliferation of OCT-1 osteoblast-like cells on micro- and nano-scale topography structured poly(L-lactide)*. Biomaterials, 2005. **26**(21): p. 4453-9.
8. Braddock, M., et al., *Born again bone: tissue engineering for bone repair*. News Physiol Sci, 2001. **16**: p. 208-13.
9. Rezwan, K., et al., *Biodegradable and bioactive porous polymer/inorganic composite scaffolds for bone tissue engineering*. Biomaterials, 2006. **27**(18): p. 3413-31.
10. P.B. Malafaya, G.A.S., E.T. Baran, R.L. Reisa, *Drug delivery therapies II. Strategies for delivering bone regenerating factors*. Current Opinion in Solid State and Materials Science, 2002. **6**: p. 297-312.
11. Kofron, M.D. and C.T. Laurencin, *Bone tissue engineering by gene delivery*. Adv Drug Deliv Rev, 2006. **58**(4): p. 555-76.

12. Lutolf, M.P. and J.A. Hubbell, *Synthetic biomaterials as instructive extracellular microenvironments for morphogenesis in tissue engineering*. Nat Biotechnol, 2005. **23**(1): p. 47-55.
13. Orsello, C.E., D.A. Lauffenburger, and D.A. Hammer, *Molecular properties in cell adhesion: a physical and engineering perspective*. Trends Biotechnol, 2001. **19**(8): p. 310-6.
14. Alberts, B., et al., *Molecular Biology of the Cell*. 3 ed. 1994: New York: Garland Publishing.
15. Anselme, K., *Osteoblast adhesion on biomaterials*. Biomaterials, 2000. **21**(7): p. 667-81.
16. Sommerfeldt, D.W. and C.T. Rubin, *Biology of bone and how it orchestrates the form and function of the skeleton*. Eur Spine J, 2001. **10 Suppl 2**: p. S86-95.
17. Nagaoka, T., Kaburagi, Y., Hamaguchi, Y., Hasegawa, M., Takehara, K., Steeber, D.A., Tedder, T.F., and S. Sato. , *American Journal of Pathology.*, 2000. **157**(1): p. 237-247.
18. Cavallaro, U. and G. Christofori, *Cell adhesion in tumor invasion and metastasis: loss of the glue is not enough*. Biochim Biophys Acta, 2001. **1552**(1): p. 39-45.
19. Folch, A. and M. Toner, *Microengineering of cellular interactions*. Annu Rev Biomed Eng, 2000. **2**: p. 227-56.
20. Garcia, A.J., *Get a grip: integrins in cell-biomaterial interactions*. Biomaterials, 2005. **26**(36): p. 7525-9.
21. Bronzino, J., *The Biomedical Engineering Handbook*. 1995, Boca Raton, Florida, : CRC Press LLC.
22. Baum, B.J. and D.J. Mooney, *The impact of tissue engineering on dentistry*. J Am Dent Assoc, 2000. **131**(3): p. 309-18.
23. Chen, B., et al., *Homogeneous osteogenesis and bone regeneration by demineralized bone matrix loading with collagen-targeting bone morphogenetic protein-2*. Biomaterials, 2007. **28**(6): p. 1027-35.
24. Akin, F.A., et al., *Preparation and analysis of macroporous TiO<sub>2</sub> films on Ti surfaces for bone-tissue implants*. J Biomed Mater Res, 2001. **57**(4): p. 588-96.
25. Qi, H., et al., *Identification of genes responsible for osteoblast differentiation from human mesodermal progenitor cells*. Proc Natl Acad Sci U S A, 2003. **100**(6): p. 3305-10.

26. Luppen, C.A., et al., *Brief bone morphogenetic protein 2 treatment of glucocorticoid-inhibited MC3T3-E1 osteoblasts rescues commitment-associated cell cycle and mineralization without alteration of Runx2*. J Biol Chem, 2003. **278**(45): p. 44995-5003.
27. Chaudhry, G.R., et al., *Osteogenic Cells Derived From Embryonic Stem Cells Produced Bone Nodules in Three-Dimensional Scaffolds*. J Biomed Biotechnol, 2004. **2004**(4): p. 203-210.
28. Vinals, F., et al., *Inhibition of PI3K/p70 S6K and p38 MAPK cascades increases osteoblastic differentiation induced by BMP-2*. FEBS Lett, 2002. **510**(1-2): p. 99-104.
29. Dennis, J.E. and P. Charbord, *Origin and differentiation of human and murine stroma*. Stem Cells, 2002. **20**(3): p. 205-14.
30. Schnabel, M., et al., *Differential expression of Notch genes in human osteoblastic cells*. Int J Mol Med, 2002. **9**(3): p. 229-32.
31. Grigoriadis, A.E., J.N. Heersche, and J.E. Aubin, *Differentiation of muscle, fat, cartilage, and bone from progenitor cells present in a bone-derived clonal cell population: effect of dexamethasone*. J Cell Biol, 1988. **106**(6): p. 2139-51.
32. Le Guehennec, L., et al., *Osteoblastic cell behaviour on different titanium implant surfaces*. Acta Biomater, 2008. **4**(3): p. 535-43.
33. Heath, C.A., *Cells for tissue engineering*. Trends Biotechnol, 2000. **18**(1): p. 17-9.
34. Gomillion, C.T. and K.J. Burg, *Stem cells and adipose tissue engineering*. Biomaterials, 2006. **27**(36): p. 6052-63.
35. Barry, F.P. and J.M. Murphy, *Mesenchymal stem cells: clinical applications and biological characterization*. Int J Biochem Cell Biol, 2004. **36**(4): p. 568-84.
36. Morrison, S.J., N.M. Shah, and D.J. Anderson, *Regulatory mechanisms in stem cell biology*. Cell, 1997. **88**(3): p. 287-98.
37. Conrad, C. and R. Huss, *Adult stem cell lines in regenerative medicine and reconstructive surgery*. J Surg Res, 2005. **124**(2): p. 201-8.
38. Tae, S.K., Lee, S.H., Park, J.S. and G.I. Im., *Mesenchymal stem cells for tissue engineering and regenerative medicine*. Biomed Mat., 2006. **1**: p. 63-71.

39. Alhadlaq, A., M. Tang, and J.J. Mao, *Engineered adipose tissue from human mesenchymal stem cells maintains predefined shape and dimension: implications in soft tissue augmentation and reconstruction*. *Tissue Eng*, 2005. **11**(3-4): p. 556-66.
40. Tuan, R.S., G. Boland, and R. Tuli, *Adult mesenchymal stem cells and cell-based tissue engineering*. *Arthritis Res Ther*, 2003. **5**(1): p. 32-45.
41. Pountos, I. and P.V. Giannoudis, *Biology of mesenchymal stem cells*. *Injury*, 2005. **36 Suppl 3**: p. S8-S12.
42. Liechty, K.W., et al., *Human mesenchymal stem cells engraft and demonstrate site-specific differentiation after in utero transplantation in sheep*. *Nat Med*, 2000. **6**(11): p. 1282-6.
43. Zavos, P.M., *Stem cells and cellular therapy: potential treatment for cardiovascular diseases*. *Int J Cardiol*, 2006. **107**(1): p. 1-6.
44. Zandstra, P.W. and A. Nagy, *Stem cell bioengineering*. *Annu Rev Biomed Eng*, 2001. **3**: p. 275-305.
45. Song, L., D. Baksh, and R.S. Tuan, *Mesenchymal stem cell-based cartilage tissue engineering: cells, scaffold and biology*. *Cytotherapy*, 2004. **6**(6): p. 596-601.
46. Prichard, H.L., W.M. Reichert, and B. Klitzman, *Adult adipose-derived stem cell attachment to biomaterials*. *Biomaterials*, 2007. **28**(6): p. 936-46.
47. McKee, M.D., *Management of Segmental Bony Defects: The Role of Osteoconductive Orthobiologics*. *Journal of the American Academy of Orthopaedic Surgeons*, 2006. **14**(10): p. S163-S167.
48. Stadlinger, B., et al., *Evaluation of osseointegration of dental implants coated with collagen, chondroitin sulphate and BMP-4: an animal study*. *Int J Oral Maxillofac Surg*, 2008. **37**(1): p. 54-9.
49. Cancedda, R., P. Giannoni, and M. Mastrogiacomo, *A tissue engineering approach to bone repair in large animal models and in clinical practice*. *Biomaterials*, 2007. **28**(29): p. 4240-50.
50. Hench, L.J., Polak, J.M., *Third-Generation Biomedical Materials*. *Science*, 2002. **295**: p. 1014-1017.
51. G Balasundaram, T.W., *A perspective on nanophase materials for orthopedic implant applications*. *Journal of Materials Chemistry*, 2006. **16**(38): p. 3737-3745

52. Yim, E.K. and K.W. Leong, *Significance of synthetic nanostructures in dictating cellular response*. *Nanomedicine*, 2005. **1**(1): p. 10-21.
53. Li, M.C., T.; Mills, D.K.; Lvov, Y.M.; McShane, M.J., *Comparison of Selective Attachment and Growth of Smooth Muscle Cells on Gelatin- and Fibronectin-Coated Micropatterns* *Journal of Nanoscience and Nanotechnology*, 2005. **5**(11): p. 1809-1815.
54. Allen, L.T., et al., *Surface-induced changes in protein adsorption and implications for cellular phenotypic responses to surface interaction*. *Biomaterials*, 2006. **27**(16): p. 3096-108.
55. Boyan, B.D., et al., *Role of material surfaces in regulating bone and cartilage cell response*. *Biomaterials*, 1996. **17**(2): p. 137-46.
56. Hoi-Yan Cheung, K.-T.L., Tung-Po Lu, David Hui, *A critical review on polymer-based bio-engineered materials for scaffold development*. *Composites: Part B*, 2007. **38**: p. 291-300.
57. Boyan, B.D., et al., *Osteoblasts generate an osteogenic microenvironment when grown on surfaces with rough microtopographies*. *Eur Cell Mater*, 2003. **6**: p. 22-7.
58. Lipski, A.M., Jaquiere, C, Choi, H ; Eberli, D. ; Stevens, M ; Martin, I. ; Cehn, I.-W. ; Prasad-Shastri, V., *Nanoscale engineering of biomaterial surfaces*. *Nanoscale engineering of biomaterial surfaces*, 2007. **19**: p. 553-557.
59. Eisenbarth, E., D. Velten, and J. Breme, *Biomimetic implant coatings*. *Biomol Eng*, 2007. **24**(1): p. 27-32.
60. Dirk Lehnert, B.W.-H., Christian David, Ulrich Weiland, Christoph Ballestrem, Beat A. Imhof, Martin Bastmeyer, *Cell behaviour on micropatterned substrata: limits of extracellular matrix geometry for spreading and adhesion* *Journal of Cell Science*, 2004. **117**: p. 41-52.
61. Huebsch, N.D. and D.J. Mooney, *Fluorescent resonance energy transfer: A tool for probing molecular cell-biomaterial interactions in three dimensions*. *Biomaterials*, 2007. **28**(15): p. 2424-37.
62. David Oupicky, A.L.P., Leonard W. Seymour, *Laterally Stabilized Complexes of DNA with Linear Reducible Polycations: Strategy for Triggered Intracellular Activation of DNA Delivery Vectors*. *Journal of the American Chemical Society*, 2002. **124**(1).

63. Francius, G., et al., *Effect of crosslinking on the elasticity of polyelectrolyte multilayer films measured by colloidal probe AFM*. Microsc Res Tech, 2006. **69**(2): p. 84-92.
64. Discher, D.E., P. Janmey, and Y.L. Wang, *Tissue cells feel and respond to the stiffness of their substrate*. Science, 2005. **310**(5751): p. 1139-43.
65. Liu, H., E.B. Slamovich, and T.J. Webster, *Increased osteoblast functions among nanophase titania/poly(lactide-co-glycolide) composites of the highest nanometer surface roughness*. J Biomed Mater Res A, 2006. **78**(4): p. 798-807.
66. Levenberg, S. and R. Langer, *Advances in tissue engineering*. Curr Top Dev Biol, 2004. **61**: p. 113-34.
67. R.C. Ghan, Y.L., R.S. Besser *Characterization of Self-Assembled SnO<sub>2</sub> Nanoparticles for Fabrication of a High Sensitivity and High Selectivity Micro-Gas Sensor*. MRS Proceedings, 2001.
68. Kommireddy, D.S., et al., *Layer-by-Layer assembly of TiO<sub>2</sub> nanoparticles for stable hydrophilic biocompatible coatings*. J Nanosci Nanotechnol, 2005. **5**(7): p. 1081-7.
69. Pargaonkar, N., et al., *Controlled release of dexamethasone from microcapsules produced by polyelectrolyte layer-by-layer nanoassembly*. Pharm Res, 2005. **22**(5): p. 826-35.
70. Zahr, A.S., M. de Villiers, and M.V. Pishko, *Encapsulation of drug nanoparticles in self-assembled macromolecular nanoshells*. Langmuir, 2005. **21**(1): p. 403-10.
71. Whitesides, G.M., J.P. Mathias, and C.T. Seto, *Molecular self-assembly and nanochemistry: a chemical strategy for the synthesis of nanostructures*. Science, 1991. **254**(5036): p. 1312-9.
72. G. Decher, J.S., *Fine-Tuning of the film thickness of ultrathin multilayer films composed of consecutively alternating layers of anionic and cationic polyelectrolytes* Progress in Colloid and Polymer Science, 1992. **89**: p. 160-164.
73. Yuri Lvov, A.A.A., Arif Mamedov, Helmuth Mohwald, and Gleb B. Sukhorukov, *Urease Encapsulation in Nanoorganized Microshells*. Nano Letters, 2001. **1**(3): p. 125-128.
74. Shutava, T.G., D.S. Kommireddy, and Y.M. Lvov, *Layer-by-layer enzyme/polyelectrolyte films as a functional protective barrier in oxidizing media*. J Am Chem Soc, 2006. **128**(30): p. 9926-34.

75. Malik, A., et al., *Structures of head-group and tail-group monolayers in a Langmuir-Blodgett film*. Phys Rev B Condens Matter, 1995. **52**(16): p. 11654-11657.
76. Yuri Lvov, G.D., Helmuth Mohwald, *Assembly, Structural Characterization, and Thermal Behavior of Layer-by-Layer Deposited Ultrathin Films of Poly(vinyl sulfate) and Poly(allylamine)*. Langmuir, 1993. **9**: p. 481-486.
77. Ai, H., et al., *Nano-encapsulation of furosemide microcrystals for controlled drug release*. J Control Release, 2003. **86**(1): p. 59-68.
78. Edwin Donath, S.M., Bjrn Neu, Gleb B. Sukhorukov, Radostina Georgieva, Andreas Voigt, Hans Baumler, Holger Kiesewetter, Helmuth M'hwald[b], *Hollow Polymer Shells from Biological Templates: Fabrication and Potential Applications*. Chemsitry -A European Journal, 2002. **8**(23): p. 5481-5485.
79. Dongsik Yoo, S.S.S., and Michael F. Rubner\*, *Controlling Bilayer Composition and Surface Wettability of Sequentially Adsorbed Multilayers of Weak Polyelectrolytes Macromolecules*, 1998. **31**(13): p. 4309 -4318.
80. Lvov, Y.M., Decher, G., *Assembly of multilayer ordered films by alternating adsorption of oppositely charged macromolecules*. Crystallography Reports, 1994. **39**(4): p. 628-647.
81. Thierry Cassagneau, J.H.F., Thomas E. Mallouk, *Optical and Electrical Characterizations of Ultrathin Films Self-Assembled from 11-Aminoundecanoic Acid Capped TiO<sub>2</sub> Nanoparticles and Polyallylamine Hydrochloride*. Langmuir, 2000. **16**: p. 241-246.
82. Vladimir V. Tsukruk, F.R., Valery N. Bliznyuk, *Self-Assembled Multilayer Films from Dendrimers*. Langmuir, 1997. **13**(8): p. 2171 -2176.
83. Izquierdo, A., et al., *Dipping versus Spraying: Exploring the Deposition Conditions for Speeding Up Layer-by-Layer Assembly*. Langmuir, 2005. **21**(16): p. 7558-7567.
84. Krogman, K.C., et al., *Automated Process for Improved Uniformity and Versatility of Layer-by-Layer Deposition*. Langmuir, 2007. **23**(6): p. 3137-3141.
85. Vineeth Kurnala, Skylar Stewart-Clark, Shilpa Edupganti, David K. Mills, Yuri Lvov. *Characterization of substrates prepared using nebulization versus traditional layer by layer assembly*. in Louisiana Emerging Materials Conference. 2006. Baton Rouge, LA.

86. Mingyuan Gao, J.S., Eric Dulkeith, Nicolai Gaponik, Uli Lemmer, Jochen Feldmann, *Lateral Patterning of CdTe Nanocrystal Films by the Electric Field Directed Layer-by-Layer Assembly Method*. Langmuir, 2002. **18**: p. 4098-4102.
87. Serizawa, T., et al., *Alternating bioactivity of polymeric layer-by-layer assemblies: anti- vs procoagulation of human blood on chitosan and dextran sulfate layers*. Biomacromolecules, 2000. **1**(3): p. 306-9.
88. Dierich, A., LeGuen, E., Messaddeq, N., Stoltz, J.F., Netter, P., Schaff, P., Voegel, J.C., Benkirane-Jessel, N., *Bone Formation Mediated by Synergy-Acting Growth Factors Embedded in a Polyelectrolyte Multilayer Film*. Advanced Materials, 2007. **19**: p. 693-697.
89. Leguen, E., et al., *Bioactive coatings based on polyelectrolyte multilayer architectures functionalized by embedded proteins, peptides or drugs*. Biomol Eng, 2007. **24**(1): p. 33-41.
90. Mao, Z., Ma, L., Zhou, J., Gao, C., Shen, J., *Bioactive Thin Film of Acidic Fibroblast Growth Factor Fabricated by Layer-by-Layer Assembly*. Bioconjugate Chemistry, 2005. **16**: p. 1316-1322.
91. Rudra, J.S., K. Dave, and D.T. Haynie, *Antimicrobial polypeptide multilayer nanocoatings*. J Biomater Sci Polym Ed, 2006. **17**(11): p. 1301-15.
92. J.J.J.P. van den Beucken, X.F.W., O.C. Boerman, M.R.J. Vos, N.A.J.M. Sommerdijk, T. Hayakawa, T. Fukushima, Y. Okahata, R.J.M. Nolte, J.A. Jansen, *Functionalization of multilayered DNA-coatings with bone morphogenetic protein 2*. Journal of Controlled Release, 2006. **113**: p. 63-72.
93. Wittmer, C.R., et al., *Fibronectin terminated multilayer films: protein adsorption and cell attachment studies*. Biomaterials, 2007. **28**(5): p. 851-60.
94. Fen-ni Fu, M.P.F., Bal Ram Singh, *Use of Fourier Transform Infrared/Attenuated Total Reflectance Spectroscopy for the Study of Surface Adsorption of Proteins*. Applied Spectroscopy, 1993. **1**: p. 98-102.
95. Richert, L., et al., *Cell interactions with polyelectrolyte multilayer films*. Biomacromolecules, 2002. **3**(6): p. 1170-8.
96. Tryoen-Toth, P., et al., *Viability, adhesion, and bone phenotype of osteoblast-like cells on polyelectrolyte multilayer films*. J Biomed Mater Res, 2002. **60**(4): p. 657-67.

97. R. Heuberger, G.S., J. Vörös, M. Textor, H. Möhwald *Biofunctional Polyelectrolyte Multilayers and Microcapsules: Control of Non-Specific and Bio-Specific Protein Adsorption*. *Advanced Functional Materials*, 2005. **15**(3): p. 357-366.
98. Hahn, S.K. and A.S. Hoffman, *Preparation and characterization of biocompatible polyelectrolyte complex multilayer of hyaluronic acid and poly-L-lysine*. *Int J Biol Macromol*, 2005. **37**(5): p. 227-31.
99. Cai, K. and Y. Wang, *Polysaccharide surface engineering of poly(D, L-lactic acid) via electrostatic self-assembly technique and its effects on osteoblast growth behaviours*. *J Mater Sci Mater Med*, 2006. **17**(10): p. 929-35.
100. Sinani, V.A., Koktysh Dmitry S. ; Yun Bo-Geon; Matts Robert L.; Pappas Todd C.; Motamedi Massoud; Thomas Stephanie N.; Kotov Nicholas A. , *Collagen coating promotes biocompatibility of semiconductor nanoparticles in stratified LBL films*. *Nano Letters*, 2003. **3**(9): p. 1177-1182
101. Kommireddy, D.S., et al., *Stem cell attachment to layer-by-layer assembled TiO<sub>2</sub> nanoparticle thin films*. *Biomaterials*, 2006. **27**(24): p. 4296-303.
102. Jan, E. and N.A. Kotov, *Successful differentiation of mouse neural stem cells on layer-by-layer assembled single-walled carbon nanotube composite*. *Nano Lett*, 2007. **7**(5): p. 1123-8.
103. Chapekar, M.S., *Tissue engineering: challenges and opportunities*. *J Biomed Mater Res*, 2000. **53**(6): p. 617-20.
104. Grant, G., Koktysh, D., Yun, B., Matts, R., Kotov, N., *Layer-By-Layer Assembly of Collagen Thin Films: Controlled Thickness and Biocompatibility*. *Biomedical Microdevices*, 2001. **3**(4): p. 301-306.
105. Ladam, G., et al., *Protein adsorption onto auto-assembled polyelectrolyte films*. *Biomol Eng*, 2002. **19**(2-6): p. 273-80.
106. Jessel, N., ATALAR Fatmah ; LAVALLE Philippe ; MUTTERER Jerome ; DECHER Gero ; SCHAAF Pierre ; VOEGEL Jean-Claude ; OGIER Joelle, *Bioactive coatings based on a polyelectrolyte multilayer architecture functionalized by embedded proteins*. *Advanced Materials*, 2003. **15**(9): p. 692-695.
107. Sauerbrey, G., *The use of quartz oscillators for weighing thin layers and for microweighing*. *Z. Phys*, 1959. **155**.

108. Caruso, F., Niikura, K., Furlong, D.N., Okahata, Y., *Ultrathin Multilayer Polyelectrolyte Films on Gold: Construction and Thickness Determination*. Langmuir, 1997. **13**(13): p. 3422-3426.
109. N. Mandzy, E.G., T. Druffel, *Breakage of TiO<sub>2</sub> agglomerates in electrostatically stabilized aqueous dispersions*. Powder Technology, 2005. **160**(2): p. 121-126.
110. Andrade, J.D., *Interfacial phenomena and biomaterials*. Med Instrum, 1973. **7**(2): p. 110-9.
111. Prasad, V., Semwogerere, D., Weeks, E.R., *Confocal microscopy of colloids*. Journal of Physics: Condensed Matter, 2007. **19**.
112. Yanjing Liu, Y., Rosidian, A., Lenahan, K., Wang, Y., Zeng, T., Claus, R.O., *Characterization of electrostatically self-assembled nanocomposite thin films*. Smart Material Structures, 1999. **8**: p. 100-105.
113. Hess, D.R., *Nebulizers: principles and performance*. Respiratory Care, 2000. **45**(6): p. 609-622.
114. Probes, M., *Product Information for Live/Dead Viability/Cytotoxicity Kit for Mammalian Cells*. 2005. p. 1-7.
115. Sciences, R.A., *Product Information Manual*. 2004.
116. Probes, I.-M., *PicoGreen*, in *Quant-iT™ PicoGreen® dsDNA Reagent and Kits*. 2005.
117. Heitz, P.U., *Immunocytochemistry--theory and application*. Acta Histochem Suppl, 1982. **25**: p. 17-35.
118. Buchter, A., et al., *Sustained release of doxycycline for the treatment of peri-implantitis: randomised controlled trial*. Br J Oral Maxillofac Surg, 2004. **42**(5): p. 439-44.
119. Mukherjee, D.P., Dorairaj, N.R., Mills, D.K., Graham, D., Krauser, J.K., *Fatigue properties of hydroxyapatite-coated dental implants after exposure to a periodontal pathogen*. Journal of Biomedical Materials Research-A, 2000. **53**(5): p. 467-474.
120. El-Hakim, I.E., I.S. Abdel-Hamid, and A. Bader, *Tempromandibular joint (TMJ) response to intra-articular dexamethasone injection following mechanical arthropathy: a histological study in rats*. Int J Oral Maxillofac Surg, 2005. **34**(3): p. 305-10.

121. T.Hickey, D.K., D.J.Burgess, F.Moussy, *In-vivo evaluation of a dexamethasone/PLGA microsphere system designed to suppress the inflammatory tissue response to implantable medical devices*. Journal of Biomedical Materials Research, 2002. **61**(180).
122. Maggiorini, M., et al., *Both tadalafil and dexamethasone may reduce the incidence of high-altitude pulmonary edema: a randomized trial*. Ann Intern Med, 2006. **145**(7): p. 497-506.
123. Tabata, Y., *Tissue regeneration based on growth factor release*. Tissue Eng, 2003. **9 Suppl 1**: p. S5-15.
124. R. van Dijkhuizen-Radersma 1, J.R.R., P. Kaim, S. Métairie, F.L.A.M.A. Péters, J. de Wijn, P.G. Zijlstra, K. de Groot, J.M. Bezemer, *Biodegradable poly(ether-ester) multiblock copolymers for controlled release applications*. Journal of Biomedical Materials Research, 2003. **67A**(4): p. 1294-1304.
125. Li, Z.Z., et al., *Controlled release of avermectin from porous hollow silica nanoparticles: influence of shell thickness on loading efficiency, UV-shielding property and release*. J Control Release, 2006. **111**(1-2): p. 81-8.
126. Park, J.H., M.G. Allen, and M.R. Prausnitz, *Polymer microneedles for controlled-release drug delivery*. Pharm Res, 2006. **23**(5): p. 1008-19.
127. Park, Y.J., et al., *Controlled release of platelet-derived growth factor from porous poly(L-lactide) membranes for guided tissue regeneration*. J Control Release, 1998. **51**(2-3): p. 201-11.
128. Ricci, M., et al., *Ketoprofen controlled release from composite microcapsules for cell encapsulation: effect on post-transplant acute inflammation*. J Control Release, 2005. **107**(3): p. 395-407.
129. Drury, J.L. and D.J. Mooney, *Hydrogels for tissue engineering: scaffold design variables and applications*. Biomaterials, 2003. **24**(24): p. 4337-51.
130. Biji Balakrishnan, A.J., *Self-cross-linking biopolymers as injectable in situ forming biodegradable scaffolds*. Biomaterials, 2005. **26**: p. 3941-3951.
131. Kristi S. Anseth, A.T.M., Stephanie J. Bryanta, Penny J. Martensa, Jennifer H. Elisseeff, Christopher N. Bowman, *In situ forming degradable networks and their application in tissue engineering and drug delivery*. Journal of Controlled Release, 2002. **78**: p. 199-209.

132. Jason A. Burdick, M.N.M., Adrian D. Hinman , Kevin Thorne , Kristi S. Anseth, Andrew T. Mettersa, Stephanie J. Bryanta, Penny J. Martensa, Jennifer H. Elisseff , Christopher N. Bowman, *Delivery of osteoinductive growth factors from degradable PEG hydrogels influences osteoblast differentiation and mineralization*. Journal of Controlled Release, 2002. **83**: p. 53-63.
133. Brown, J.Q., R. Srivastava, and M.J. McShane, *Encapsulation of glucose oxidase and an oxygen-quenched fluorophore in polyelectrolyte-coated calcium alginate microspheres as optical glucose sensor systems*. Biosens Bioelectron, 2005. **21**(1): p. 212-6.
134. R. D. Jayant, R.S., *Dexamethasone Release from Uniform Sized Nanoengineered Alginate Microspheres*. Journal of Biomedical Nanotechnology, 2007. **3**: p. 245-253.
135. J. E. Roldan, T.R.M., S. Kunder, M.M. de Villiers, H. Ai, M. J. McShane, Y. Lvov, D. K. Mills. *NANOSIGNALS: Engineering the Temporomandibular Joint Disc*. in *TMJ Association's Third Scientific Meeting: Advancing Diagnostic Approaches for TMJ Diseases and Disorders*. 2004.
136. Sweigart, M.A. and K.A. Athanasiou, *Toward tissue engineering of the knee meniscus*. Tissue Eng, 2001. **7**(2): p. 111-29.
137. Giannoni, P. and R. Cancedda, *Articular chondrocyte culturing for cell-based cartilage repair: needs and perspectives*. Cells Tissues Organs, 2006. **184**(1): p. 1-15.
138. Garcia, A.J., M.D. Vega, and D. Boettiger, *Modulation of cell proliferation and differentiation through substrate-dependent changes in fibronectin conformation*. Mol Biol Cell, 1999. **10**(3): p. 785-98.
139. Copur, M.S., P. Ledakis, and M. Norvell, *Prevention of delayed emesis caused by chemotherapy*. N Engl J Med, 2000. **343**(12): p. 888-9; author reply 889-90.
140. Milam, S.B., *Pathophysiology and epidemiology of TMJ*. J Musculoskelet Neuronal Interact, 2003. **3**(4): p. 382-90; discussion 406-7.
141. Leonardi, R., et al., *Immunolocalization of vimentin and alpha-smooth muscle actin in dysfunctional human temporomandibular joint disc samples*. J Oral Rehabil, 2002. **29**(3): p. 282-6.
142. Jackson, R.A., V. Nurcombe, and S.M. Cool, *Coordinated fibroblast growth factor and heparan sulfate regulation of osteogenesis*. Gene, 2006. **379**: p. 79-91.

143. Bosetti, M., et al., *Effect of different growth factors on human osteoblasts activities: a possible application in bone regeneration for tissue engineering*. *Biomol Eng*, 2007. **24**(6): p. 613-8.
144. Subramani, K., Birch, M.A., *Fabrication of poly(ethylene glycol) hydrogel micropatterns with osteoinductive growth factors and evaluation of the effects on osteoblast activity and function*. *Biomedical Materials*, 2006. **1**: p. 144-154.
145. Ripamonti, U., *Bone induction by recombinant human osteogenic protein-1 (hOP-1, BMP-7) in the primate Papio ursinus with expression of mRNA of gene products of the TGF-beta superfamily*. *J Cell Mol Med*, 2005. **9**(4): p. 911-28.
146. Matsusaki, M., et al., *Controlled release of vascular endothelial growth factor from alginate hydrogels nano-coated with polyelectrolyte multilayer films*. *J Biomater Sci Polym Ed*, 2007. **18**(6): p. 775-83.
147. Reddi, A.H., *Bone morphogenetic proteins: from basic science to clinical applications*. *J Bone Joint Surg Am*, 2001. **83-A Suppl 1**(Pt 1): p. S1-6.
148. Jeon, O., et al., *Enhancement of ectopic bone formation by bone morphogenetic protein-2 released from a heparin-conjugated poly(L-lactic-co-glycolic acid) scaffold*. *Biomaterials*, 2007. **28**(17): p. 2763-71.
149. Ramsden, J.L., Y., Decher, G., *Determination of optical constants of molecular films assembled via alternate polyion adsorption* *Thin Solid Films*, 1995. **254**(1-2): p. 246-251.
150. Joseph B. Schlenoff, S.T.D., Tarek Farhat *Sprayed Polyelectrolyte Multilayers* *Langmuir*, 2000. **16**(26): p. 9968 -9969.
151. Izquierdo, A., et al., *Dipping versus spraying: exploring the deposition conditions for speeding up layer-by-layer assembly*. *Langmuir*, 2005. **21**(16): p. 7558-67.
152. Caruso, F., *Nanoengineering of Particle Surfaces*. *Advanced Materials*, 2001. **13**(1): p. 11-22.
153. Haynie, D.T., *Physics of polypeptide multilayer films*. *J Biomed Mater Res B Appl Biomater*, 2006. **78**(2): p. 243-52.
154. Miura, S., Y. Teramura, and H. Iwata, *Encapsulation of islets with ultra-thin polyion complex membrane through poly(ethylene glycol)-phospholipids anchored to cell membrane*. *Biomaterials*, 2006. **27**(34): p. 5828-35.
155. Svaldo-Lanero, T., et al., *Morphology, mechanical properties and viability of encapsulated cells*. *Ultramicroscopy*, 2007. **107**(10-11): p. 913-21.

156. Chia, S.M., et al., *Multi-layered microcapsules for cell encapsulation*. Biomaterials, 2002. **23**(3): p. 849-56.
157. Konno, T. and K. Ishihara, *Temporal and spatially controllable cell encapsulation using a water-soluble phospholipid polymer with phenylboronic acid moiety*. Biomaterials, 2007. **28**(10): p. 1770-7.
158. Bae, K.H., J.J. Yoon, and T.G. Park, *Fabrication of hyaluronic acid hydrogel beads for cell encapsulation*. Biotechnol Prog, 2006. **22**(1): p. 297-302.
159. Batorsky A, L.J., Lund AW, Plopper GE, Stegemann JP, *Encapsulation of adult human mesenchymal stem cells within collagen-agarose microenvironments*. Biotechnology and Bioengineering, 2005. **92**(4): p. 492-500.
160. Chung, C.A., C.W. Yang, and C.W. Chen, *Analysis of cell growth and diffusion in a scaffold for cartilage tissue engineering*. Biotechnol Bioeng, 2006. **94**(6): p. 1138-46.
161. Babensee, J.E., L.V. McIntire, and A.G. Mikos, *Growth factor delivery for tissue engineering*. Pharm Res, 2000. **17**(5): p. 497-504.
162. Delgado, J.J., et al., *Validation of a method for non-invasive in vivo measurement of growth factor release from a local delivery system in bone*. J Control Release, 2006. **114**(2): p. 223-9.
163. Orive, G., et al., *Cell encapsulation: promise and progress*. Nat Med, 2003. **9**(1): p. 104-7.
164. Gleb B. Sukhorukov, E.D., Heinz Lichtenfeld, Eberhard Knippel, Monika Knippel, Axel Budde, Helmuth Möhwald, *Layer-by-layer self assembly of polyelectrolytes on colloidal particles* Colloids and Surfaces A: Physicochemical and Engineering Aspects, 1998. **137**(1-3): p. 253-266.
165. Diaspro A, S.D., Krol S, Cavalleri O, Gliozzi A, *Single living cell encapsulation in nano-organized polyelectrolyte shells*. Langmuir, 2002. **18**(13): p. 5047-5050.
166. H Ai, M.F., S Jones, Y Lvov *Electrostatic layer-by-layer nano-assembly on biological microtemplates: platelets*. Biomacromolecules, 2002. **3**(3): p. 560-564.
167. Hillberg, A.L. and M. Tabrizian, *Biorecognition through layer-by-layer polyelectrolyte assembly: in-situ hybridization on living cells*. Biomacromolecules, 2006. **7**(10): p. 2742-50.
168. M. -P. I. Van Damme, P.S., K. Derry, W. H. Murphy, B. N. Preston, *Temporal changes in charge content of cultured chondrocytes from bovine cartilaginous tissues*. Matrix Biology, 1997. **15**(7): p. 495-502.

169. Burke, S.E. and C.J. Barrett, *pH-responsive properties of multilayered poly(L-lysine)/hyaluronic acid surfaces*. *Biomacromolecules*, 2003. **4**(6): p. 1773-83.
170. Picart C, L.P., Hubert P, Cuisinier FJG, Decher G, Schaaf P, Voegel JC, *Buildup Mechanism for Poly(L-lysine)/Hyaluronic Acid Films onto a Solid Surface* *Langmuir*, 2001. **17**(23): p. 7414-7424.
171. Reibetanz, U., et al., *Defoliation and plasmid delivery with layer-by-layer coated colloids*. *Macromol Biosci*, 2006. **6**(2): p. 153-60.
172. Germain, M., et al., *Protection of mammalian cell used in biosensors by coating with a polyelectrolyte shell*. *Biosens Bioelectron*, 2006. **21**(8): p. 1566-73.
173. Deng WM, B.M., *Patterning and morphogenesis of the follicle cell epithelium during Drosophila oogenesis*. *International Journal of Developmental Biology*. **42**(4): p. 541-542.
174. Darcy A. Reed, K.A.L., Candice A. Stafford, Allison K. Hansen, Jocelyn G. Millar, Lawrence M. Hanks, Timothy D. Paine, *Host defensive response against an egg parasitoid involves cellular encapsulation and melanization* *Biological Control*, 2007. **41**(2): p. 214-222.
175. Snyder, D.S., et al., *Structure of a capsular polysaccharide isolated from Salmonella enteritidis*. *Carbohydr Res*, 2006. **341**(14): p. 2388-97.

## VITA

Skylar Stewart-Clark was born in Charleston, South Carolina on September 23, 1981, the daughter of Marvin and Georgette Stewart. After graduating from The Academic Magnet High School, North Charleston, South Carolina in 1999, she matriculated at Louisiana Tech University and earned a Bachelor of Science, cum laude, in Biomedical Engineering in May 2003. She entered the Masters of Biomedical Engineering program at Louisiana Tech in June 2003, and later was admitted to the PhD in Biomedical Engineering program in May 2005. She was awarded the NSF GK-12 fellowship for 4 years. She is married to Geoffrey Alan Clark of Bossier City, Louisiana and gave birth to their son, Adrian Prentiss Clark, on December 29, 2006.

### PUBLICATIONS, CONFERENCE PROCEEDINGS, AND PRESENTATIONS

- **S. Stewart-Clark**, Y. Lvov, D. Mills. "Release of Dexamethasone from thin-film modified drug aggregates and calcium alginate microspheres" (in preparation)
- **S. Stewart-Clark**, Y. Lvov, D. Mills. "TGF $\beta$ -1 and TiO<sub>2</sub>-embedded cellular substrates fabricated by nebulization" (in preparation)
- **S. Stewart-Clark**, M. Groan, K. Keeton, L. Ramsey, S. Jones, D. Mills. "Creating Connections: a model for incorporating scientific investigation and research into Louisiana's K-12 curriculum" AAAS Annual Meeting, Boston, MA, 2008.
- N. Veerabdran, P. Goli, **S. Stewart-Clark**, Y. Lvov, D. Mills. "Nanoencapsulation of Stem Cells within Polyelectrolyte Multilayer Shells." *Macromolecular Bioscience* 7(7), 887-882, 2007.
- **S. Stewart-Clark**. "Responsive Drug Delivery Systems", Biomedical Engineering 325, guest lecture, Louisiana Tech University, 2007
- V. Kurnala, S. Edupganti, **S. Stewart-Clark**, Y. Lvov, D. Mills. "Nebulization: A novel method for creating enhanced cell-supportive substrates", Houston BMES Conference, Houston, TX. (oral talk), 2007.

- V. Kurnala, **S. Stewart-Clark**, Y. Lvov, D. Mills. “Characterization of substrates prepared using nebulization versus traditional layer by layer assembly”, Louisiana Emerging Materials Conference, Baton Rouge, LA. (1<sup>st</sup> place), 2006.
- N. Veerabadran, P. Goli, **S. Stewart-Clark**, D. Mills, Y. Lvov. “Nanoencapsulation of stem cells within polyelectrolyte multilayer shells”, Nanofabrication Lecture Series: Functional Nanoassemblies, Louisiana Tech University. (oral talk), 2006.
- **S. Stewart-Clark**, J. Roldan, D. Mills, Y. Lvov. “A comparison of bioactive microstructures for mesenchymal tissue engineering “, BMES Annual Fall Meeting, Chicago, IL, 2006.
- **S. Stewart-Clark**, J. Roldan, D. Mills, Y. Lvov. “Layer-by-Layer Adsorption of Biocompatible Polyelectrolytes onto Dexamethasone Aggregates”, IEEE Engineering in Medicine and Biology Conference, New York, NY. (oral talk), 2006.
- **S. Stewart**, S. Bezucha, J. Roldan, Y. Lvov, D. Mills. “Osteoblast Expression in Response to Bioactive Microstructures”, Experimental Biology, San Francisco, CA, 2006.
- **S. Stewart**, J. Roldan, S. Bezucha, J. DuBois, D. Hough, L. Ramsey, D. Mills. “Implementation of Case-Based Modules in Rural Northeast Louisiana High Schools”, Experimental Biology, San Francisco, CA, 2006.
- J. E. Roldan, **S. S. Stewart**, J. N. DuBois, L. L. Ramsey, and D. K. Mills “Inquiry-Based Activities and Technology to Improve Student Performance on the Science Reasoning Portion of the ACT (American College Test)”. American Society for Engineering Education Conference and Exposition. Portland, OR. (oral talk), 2005.
- **S. S. Stewart**, W. Ying, W.B. Besio, D.K. Mills. “The Effects of Infrared Laser Therapy on Human Dermal Fibroblasts”, Applied and Natural Sciences Research Day. Louisiana Tech University, 2004.
- J Roldan, **S Stewart**, M Mikail, M Boquet, L Smith, M de Villers. “Thermally Enhanced Transdermal Drug Delivery Patch”, BMES Annual Fall Meeting. Nashville, TN, 2003